Development of Albumin-Hitchhiking siRNA Conjugates for Therapeutic Mcl-1 Silencing in Triple Negative Breast Cancer

By

Ella Nicole Hoogenboezem

Dissertation

Submitted to the Faculty of the

Graduate School of Vanderbilt University

in partial fulfillment of the requirements

for the degree of

DOCTOR OF PHILOSOPHY

in

Biomedical Engineering

May 31, 2022

Nashville, Tennessee

Approved:

Craig L. Duvall, Ph.D.

Rebecca S. Cook, Ph.D.

Dana M. Brantley-Sieders, Ph.D.

Ethan S. Lippmann, Ph.D.

Kasey C. Vickers, Ph.D.

John T. Wilson, Ph.D.

Dedication

This work is dedicated to my late grandfather, Ronald Aubrey Council, who always believed in me.

Acknowledgements

I am of the belief that it takes a village to generate a Ph.D., and my own doctoral work is no exception. Without the help of my wonderful mentors, colleagues, and collaborators, the work described here would not have been possible. I am grateful to all of my labmates and lab alumni, but particularly to Dr. Meredith Jackson, Dr. Rebecca Cook, Dr. Eric Dailing, Dr. Prarthana Patil, Shrusti Patel, Dr. Justin Lo, Carlisle DeJulius, Juan Colazo, Joshua McCune, Larry Stokes, Isom Kelly, Jordan Hill, William Tierney, Dr. Kameron Kilchrist, Dr. Bryan Dollinger, Dr. Nora Francini, Dr. Fang Yu, and Dr. Mukesh Gupta who actively took roles teaching me and spending time helping me produce the research I detail herein. Without my advisor, Dr. Craig Duvall, none of this would have been possible. I am incredibly grateful to him for recognizing something in me that led him to invite me to join his lab. He has given me encouragement along every step of the way and shared in the triumphs and heartaches with great investment. I will be eternally thankful for his advising and friendship.

Behind every successful piece of data, there were at least a handful of failures. And behind every failure, there was almost undoubtedly a phone call fielded by my amazing family and support system. Thank you to my parents, Virginia Marina and Willem Hoogenboezem, who have always believed in me and supported me. I appreciate every pep talk along the way more than you can know. Thank you to my big brother, Austin Hoogenboezem, for brightening my life with laughs and love. Thank you to my late grandparents, Ronald Council and Charlotte Council, who have always and will always be an important part of who I am. I am grateful to my Aunt Nicole, Uncle Craig, and Grandma Lorraine for always cheering me on and supporting me in a myriad of ways.

I could not possibly have made it through grad school without the friends who lifted me up and helped me build a beautiful life outside of lab. From the Kentucky Ave. boys, Linus Lee, Alvin Mukalel,

and Zack Zimmers, who made my first year here so fun, to the chemical engineering gang, Dr. Kyle Garland, Dr. Prarthana Patil, Dr. Mohsin Rahim, Dr. Jonah Rosch, Dr. Allison Bosworth, Dr. Kathryn Ozgun, Carlisle DeJulius, Jesse Beckner, and Dr. Richard D'Arcy, and finally members of the Taco Mama Club, Bonnie Walton, Dr. Blaise Kimmel, and Jessalyn Baljon, the friends I made in Nashville made my life here so happy. I am even more fortunate to have had friends that I met as far back as elementary school whose love and support have continued to enrich my life from afar. Thank you forever to Ashley Meade, Megan Miner, Dylan Wright, Brittney Munyer, Emily Thorp, and so many others for your friendships.

I would additionally like to thank the members of my thesis committee, Drs. John Wilson, Ethan Lippmann, Kasey Vickers, Dana Brantley-Sieders, and Rebecca Cook, each of which I have had the distinct honor and pleasure of getting to work with and build a personal relationship with. I would also like to acknowledge my funding sources: the National Institutes of Health (R01 CA224241, R01 EB019409, R01 CA260958, R21 AR078636, T32 CA217834) and the National Science Foundation (BMAT 1349604).

Table of Contents

Table of Figures

Chapter 1: Introduction

1.1 Background and Significance

RNA interference (RNAi) is a powerful, innate gene-silencing mechanism first uncovered in 1998[1]. RNAi modalities can be used to silence the expression of a target gene in a sequence-specific manner. One such modality, called short interfering RNA (siRNA), comprises a double stranded RNA of approximately 21-27 nucleotides[2] with one strand complementary to a section of target mRNA, called the antisense strand, and its complementary strand, termed the sense strand. Once intracellular, these siRNAs act as guides within a ribonucleic acid-protein complex, called the RNA-induced silencing complex (RISC), which cleaves the target mRNA that is aligned with the antisense strand[2]. The resulting degradation of the corresponding mRNA can therefore, in theory, be used to specifically target and prevent the synthesis of any disease-driving protein in the body. However, in their unmodified form, siRNAs are rapidly cleared or degraded by the body. Specifically, the body contains an abundance of enzymes that specifically degrade nucleic acids, called nucleases. Additionally, siRNAs are rapidly cleared from the body by the kidneys, resulting in a short circulation half-life and limited bioavailability.

Because of their large size (>10,000 Da), negative charge, and hydrophilic nature, siRNAs also lack the ability to effectively penetrate cell membranes. This is a critical obstacle because the site of action for siRNAs is in the cell cytoplasm. Moreover, they lack the ability to target a specific cell subtype. To overcome these barriers, attempts have been made to encapsulate these oligonucleotides into nanosized carriers. Indeed, the first clinical breakthrough in the field was achieved by packaging siRNA into a lipid nanoparticle called patisiran[3], which consists of a pH-sensitive, fusogenic amino lipid (MC3), phosphatidylcholine (DSPC), cholesterol, and dimyristoylglycerol PEG[4]. The MC3 fusogenic

lipid confers cell membrane penetration, “helper lipids” DSPC and cholesterol facilitate the stable encapsulation of siRNA, and PEG-lipid, dimyristoylglycerol PEG, regulates particle size without compromising activity[5]. This platform has been used to successfully target liver hepatocytes and knockdown transthyretin (TTR) for the treatment of polyneuropathy from hereditary TTR-mediated amyloidosis[6]. However, lipid nanoparticles have previously found limited clinical success due to inadequate efficacy and significant toxicity. Indeed, even patisiran requires intravenous administration inside of a clinical setting, and those given the drug must take steroids to suppress infusion-related reactions[7]. The challenges associated with these systems have given rise to a shift in the field toward carrier-free delivery of siRNAs. Since the establishment of patisiran, all subsequently FDA-approved siRNA drugs to date have utilized a trivalent N-acetylgalactosamine (GalNAc)-siRNA conjugate platform that targets the asiaglycoprotein receptor on liver hepatocytes. Currently, this construct serves as the basis for three FDA-approved treatments (givosiran, lumasiran, inclisiran) that target liver-derived diseases without the need for encapsulation.

Despite these exciting clinical advances, siRNA therapies for extrahepatic targets have remained elusive. In particular, siRNA holds immense unrealized potential for blocking expression of oncogenic drivers, many of which are not druggable using traditional small molecules. Traditional small molecules are prone to having off-target effects by affecting proteins of similar conformation. Moreover, the generation of small-molecule drugs requires substantial investment involving i) screening a library of compounds to identify lead structures ii) identifying regions of the small molecule at which substitutions lead to changes in sensitivity or specificity and iii) deriving additional derivatives to optimize the efficacy of the small molecule[8]. Comparatively, siRNAs are relatively straightforward to synthesize and screen. Moreover, though small molecules have revolutionized cancer treatment, their molecular

coverage is limited to only ~130 of the nearly 16,000+ protein families and 10,000+ protein folds encoded without the genome, leaving many oncogenic drivers currently undruggable[9].

The ability to silence these currently undruggable targets using RNAi in extrahepatic tumor targets holds immense promise. However, traditional cancer nanomedicines designed to deliver therapeutics like siRNA have shown a considerable disparity between preclinical and clinical success. These platforms were historically developed to leverage the phenomenon known as the enhanced permeability and retention (EPR) effect, through which macromolecules such as nanocarriers are thought to accumulate near leaky tumor vasculature[10, 11]. However, there is growing appreciation that clinical tumor specimens possess a much greater level of heterogeneity compared to commonly used mouse tumor models, which can lead to non-uniform delivery. Thus, reliance on the EPR effect alone for tumor delivery has come under scrutiny. A paradigm shift to include active processes for tumor delivery has instead come forward in the field. The first observations of preferential macromolecule accumulation in tumors were made based on the accumulation of a copolymer called SMANCS (polystyrene-co-maleic acid-half-butylate)[12, 13]. The effect was therefore thought to be applicable to a variety of macromolecules and lipidic particles. However, it is important to note that this polymer binds to the most abundant protein in the blood, called albumin. Additional studies in this seminal work examined labeled albumin itself to further support these conclusions. However, albumin itself possesses properties that make it unique among macromolecules in tumor accumulation[14]. As the most concentrated protein in the blood at 40 mg/mL, compared to its interstitial concentration of 14 mg/mL, diffusional transport of albumin is favorable[15]. When albumin extravasates into tissue, it is returned to the vascular space *via* the lymphatic system. Albumin's reliance on the lymphatic system to return to the circulation from the extracellular space therefore makes it prone to accumulation in tumors, which are often characterized by poor lymphatic drainage[16].

In addition to its desirable passive tumor accumulation, albumin is also preferentially internalized by tumor cells *via* active processes. In 2013, Commisso et al. observed a mechanism by which cancer cells can support their increased metabolic and growth needs by active uptake of extracellular proteins through macropinocytosis. They observed that cancer cells expressing oncogenic protein Ras, whose aberrant activation is associated with virtually all aspects of the malignant cancer phenotype, more highly utilize extracellular proteins (of which albumin is the most abundant) as a source of amino acids to drive cellular growth[17, 18].

Some cancer cells also preferentially use receptor-mediated albumin uptake pathways in addition to upregulated use of nonspecific macropinocytic mechanisms. This has become particularly evident based on the discovery that a correlation exists between expression of albumin-related receptors and relative efficacy of albumin-based therapies among different cancer types. Nab-paclitaxel (nab-P), also known as Abraxane, is an FDA-approved albumin-bound paclitaxel particle. Recently, Chatterjee et al. attempted to elucidate why certain pancreatic cancer patient populations responded better to treatment with nab-P than others[19]. It had previously been posited that SPARC (secreted protein acidic and rich in cysteine) was a critical albumin-binding protein that facilitates the efficacy of nab-P in metastatic pancreatic cancer. This idea was based on small scale retrospective studies (n=16) on nab-P treatment of head and neck cancer where the relationship was examined between SPARC tumor expression and patient outcomes[20]. However, further exploration in a phase III clinical trial on nab-P in metastatic pancreatic patients demonstrated no association between SPARC level and treatment efficacy[21]. Chatterjee et al. instead investigated the role the caveolae, omega-shaped invaginations of the plasma membrane, play in albumin uptake in cancer cells. Caveloae have previously been implicated in a wide variety of cellular processes including endocytosis, transcytosis, and signal transmission. The primary protein necessary for caveolae formation, Cav-1, is upregulated in a wide variety of cancer types

including pancreatic cancer, prostate cancer, and breast cancer, and Cav-1 upregulation is associated with cancer progression [19, 22-24]. It has been shown in Cav-1 deficient mice that caveolae are critical to albumin uptake and transport[25]. Interestingly, Chatterjee et al. demonstrated that RNAi-mediated attenuation of Cav-1 in cancer cells reduces albumin and nab-paclitaxel uptake and causes resistance to nab-paclitaxel-induced apoptosis. Thus, albumin has great potential for increasing the therapeutic efficacy of cancer therapeutics by conferring active uptake by tumor cells.

In addition to its passive and active tumor tropism, albumin's comparatively small size (hydrodynamic radius of ~4 nm[26, 27]) compared to traditional nanocarriers makes it an appealing drug delivery platform. With the growing appreciation for tumor heterogeneity in clinical specimens, therapeutics that can achieve more homogenous penetration in the tumor microenvironment have become prioritized. Indeed, observations in a wide variety of tumor models including syngeneic breast tumors, mouse mammary intraepithelial neoplasia outgrowths, and epithelial-mesenchymal transition tumors, permeability to albumin is ~4 gold greater than 100 nm liposomes [28]. Albumin accumulation has been observed in a variety of solid tumor animal models including sarcoma, ovarian carcinoma, and Novikof hepatoma[29].

Of note, albumin is a natural ferry within the body for fatty acids and other hydrophobic cargo. To this end, clinical success has been found by modifying therapeutics with ligands designed to bind albumin *in situ*. For instance, FDA-approved Semaglutide is a GLP-1 analog that achieved systematic protraction by maximizing reversible albumin binding through optimization of a linked fatty acid moiety[30, 31]. Notable preclinical examples include the use of a diacyl lipid linked by polyethylene glycol to deliver antigen/adjuvant cargo[32], palmitoyl modification to the 2' position of antisense oligonucleotides[33], DNA nanocages modified with branching 12-carbon chains[34], and fatty acid-bound platinum prodrugs[35]. However, optimization in the context of siRNA delivery to solid tumors has never

been explored. More notably, siRNA holds immense promise for addressing a critical unmet need to create molecularly targeted therapeutics in triple negative breast cancer (TNBC), specifically. TNBC is a highly aggressive clinical breast cancer subtype with few treatment options. TNBC patients are currently relegated to chemotherapies and do not typically benefit from molecularly targeted therapies. The first non-chemotherapy, PARP inhibitor olaparib, was approved in January 2018 for treatment of *BRCA*-1 mutant TNBCs, which account for only about 10% of all TNBCs.

Tumor cell apoptosis, regulated by members of the Bcl-2 family[36, 37], is often evaded by TNBCs[36, 38, 39]. Anti-apoptotic protein myeloid cell leukemia 1 (Mcl-1) is the most frequently altered Bcl-2 family protein in TNBC[37, 40-43]. Analysis of clinical specimens shows high Mcl-1 expression in TNBCs relative to normal breast tissue[44]. Further, Mcl-1 knockdown *via* RNAi has been shown to decrease growth in multiple TNBC lines[45]. Mcl-1 has proven clinical ties to tumor survival, drug resistance, and poor prognosis[41, 46-48,]. Analysis of 89 surgically resected TNBCs resistant to neoadjuvant chemotherapy showed that the second most common genetic alternation was MCL1 amplification (55%, second to MYC) [49]. Similarly, taxane-resistant breast, ovarian, colon, and lymphoma tumor cells exhibit Mcl-1 stabilization[48, 50]. Mcl-1 is therefore a particularly promising target for molecularly focused therapeutics.

Of the many small molecule Mcl-1 inhibitor discovery programs, few have reached Phase I clinical trials. Servier Pharmaceuticals has one of the most advanced programs with its drug S64315 and 3 ongoing trials, while Amgen recently put their clinical studies on hold due to cardiotoxicity[51]. Broadly, discovery efforts have been hindered by lack of compound Mcl-1 selectivity relative to other Bcl-2 family proteins (e.g., Bcl-2, Bcl-xL),[52] and poor solubility and *in vivo* PK[53]. A critical disadvantage of all small molecule Mcl-1 inhibitors is that they are limited to binding the Mcl-1 BH3-domain binding pocket (the Bim interaction pocket), leaving Mcl-1 intact to carry out functions unrelated to Bim

binding, such as cancer stem cell regulation[54, 55]. Further, Mcl-1 small molecules induce strong, compensatory Mcl-1 protein upregulation[56], self-limiting their therapeutic window and necessitating higher, potentially toxic dosing. The Mcl-1 inhibitor S63845 showed preclinical efficacy in hematological cancers[57], although was ineffective in TNBC as a single agent[58]. As Mcl-1 is important for hematopoietic stem cells[59] and cardiac function[60, 61], S63845 caused erythrocyte depletion, hemolysis, and weight loss at 60 mg/kg, but was safe at 25 mg/kg (though MTD is ~12.5 mg/kg in humanized Mcl-1 mice[62]). Improved Mcl-1 inhibitors would provide a wider therapeutic window to optimize tumor cell killing while limiting extra-tumoral Mcl-1 inhibition. An RNAi-based approach will inhibit all Mcl-1 functions, not just at the BH3 binding pocket and will prevent compensatory Mcl-1 protein upregulation.

In sum, albumin is an underexplored "Trojan horse" for delivery to tumor cells. Specifically, this dissertation explores utilizing albumin to deliver oncogene-targeting siRNA as a molecularly targeted therapeutic for TNBC. We hypothesize that by optimizing a lipid-modified siRNA construct for albumin binding, we can achieve therapeutic Mcl-1 silencing for reduction of tumor burden in TNBC.

1.2 Specific Aims

To address the unmet need for more broadly applicable, molecularly targeted TNBC therapy, our goal is to develop a rationally designed, albumin-binding Mcl-1 siRNA conjugate that avoids the drawbacks associated with small molecule treatments for therapeutic use in TNBC. To this end, we pursue the following specific aims:

Specific Aim 1: Create an optimized siRNA conjugate for albumin binding to improve pharmacokinetic properties and tumor gene silencing

In this aim, we will seek to systematically optimize the valency and linker of our siRNA conjugate for albumin binding. To screen our library of candidates, we will use the pharmacokinetic parameters

generated by real-time intravital microscopy of fluorophore-labeled conjugates, the relative amount of conjugate bound to albumin as determined by size exclusion chromatography, and carrier-free gene silencing and biodistribution in a tumor-bearing mouse model as the primary determinants of efficacy.

Specific Aim 2: Interrogate structure-function relationship and mechanism of action of lead siRNA conjugate

Using the lead siRNA conjugate candidate determined by Aim 1, we will then seek to interrogate the structure-function relationship of the conjugate to elucidate potential iterative designs and shed light on the conjugate mechanism of action. To this end, we will examine the effect of steric confinement of divalent conjugate lipid tails, phosphorothioate content of the albumin-binding moiety, reversible versus covalent binding of siRNA to albumin, and the implications of conjugate lipid chemistry. Examining these structural components will give insight into the competition between albumin binding and steric hindrance, the role that nuclease sensitivity and the nature of the phosphorothioate bond play in protein binding, the benefit of binding endogenous albumin without conformational modifications, and how tuning lipid hydrophobicity, functional groups, and saturation impact albumin binding and ultimate tumor gene silencing.

Specific Aim 3: Establish treatment efficacy and toxicology profiles of albumin-binding Mcl-1 siRNA conjugate relative to a clinically tested Mcl-1 small molecule inhibitor.

We will first seek to generate proof-of-concept using our first-generation siRNA conjugate to examine the potential of carrier-free silencing of Mcl-1 to achieve therapeutic efficacy in a mouse model of TNBC. Clinically relevant small molecule inhibitors of Mcl-1 have been limited by their toxicity and limited therapeutic windows *in vivo*. We will therefore seek to robustly characterize the toxicity profile of our lead Mcl-1 targeting siRNA conjugate as a comparison. Finally, we will look at therapeutic

efficacy of our lead conjugate versus a small molecule Mcl-1 inhibitor *in vivo*. To further examine the possibility for novel therapeutic combination therapies, we will co-administer an EGFR inhibitor that has been shown to have promising synergy with Mcl-1 inhibition in TNBC.

Chapter 2: Creation of an Optimized siRNA Conjugate for Albumin Binding to Improve Pharmacokinetic Properties and Tumor Gene Silencing

2.1 Introduction

We previously reported the utility of conjugating a diacyl lipid, DSPE-PEG_{2000}, to siRNA to facilitate albumin binding[63]. This hydrophobic modification was selected based on prior reports of its use for *in situ* albumin-targeting to promote delivery of peptide antigens to lymph nodes for vaccine applications[32]. However, polypeptides are far less polar than oligonucleotides and necessitate a large ethylene glycol block. Thus, this structure was not optimized for oligonucleotide delivery, leaving a significant gap for improvement. Additionally, our initial foray into this area utilized commercially available siRNAs that were not fully modified for *in vivo* stability. Modification of these siRNAs also required inefficient, two-step, solution-phase click chemistry.

We therefore sought to optimize our albumin-binding siRNA conjugate by first synthesizing robust, metabolically stable siRNA sequences. We then pursued systematic iteration of lipid valency and linker length to identify an optimal construct for albumin binding. By leveraging solid-phase synthesis to create a library of siRNA candidates, we were able to achieve high yields and fidelity for characterizing iterative differences between siRNA constructs in our library. We compare these conjugates to our “first generation” DSPE-PEG 2kDa-modified siRNA in addition to well characterized, cholesterol-TEG-siRNA. An optimal construct was identified by screening this library for its

pharmacokinetic properties, *in vivo* albumin binding properties, and efficacy in a tumor-bearing mouse model.

2.2 Results and Discussion

To first ensure that our subsequent constructs would not be limited by endo- and exo-nuclease degradation, we sought to synthesize siRNAs that were fully stabilized at the 2' position of the ribosugar. Modifying this position to replace the canonical hydroxyl with a synthetic fluoro (2'F) or methyl group (2'OMe) has been shown to confer protection from endonucleases[64]. Additionally, by replacing the phosphodiester (PO) linkages with phosphorothioate (PS) linkages on the termini of siRNA, resistance to exonuclease degradation can also be conferred[65]. Rather than employing a Dicer substrate siRNA, which gets cleaved intracellularly into 21-mers (19-mers with 2 nucleotide overhangs), we synthesized the synthetic 19-mer, blunt-ended downstream product (**Fig. 2.1A)**. The introduction of a synthetic siRNA of 19-21 nucleotides triggers gene silencing in cells and is expected to be more effective than longer fragments, especially in tumours that have low Dicer levels. In addition, longer RNA fragments may result in greater potential for toxic effects, especially in the liver[66].

This analog was able to achieve comparable potency to Dicer substrate siRNA when delivered by lipofection (**Fig. 2.1B),** but, importantly, demonstrated strikingly better stability when challenged at physiologic conditions with 60% serum (**Fig. 2.1C).** While traditional Dicer substrate siRNAs degrade within 4 h of serum challenge, the blunt ended siRNAs made with the alternating 2'F and 2'OMe "zipper" pattern of modifications and terminal PS bonds showed robust stability out to at least 48 h.

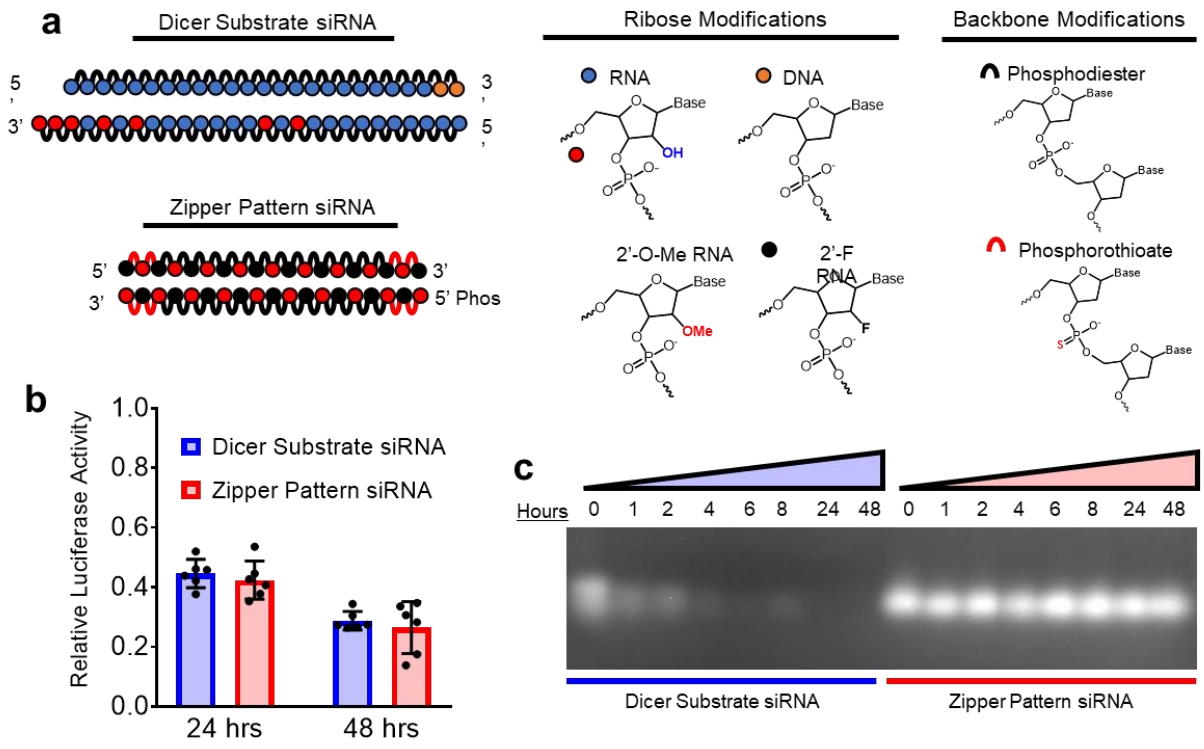

Figure 2.1 Utilizing siRNA modifications maintains knockdown potency while improving serum stability. (A) Graphical schematic of structural differences between synthetic Dicer Substrate siRNA and alternating 2'F-, 2'OMe-modified "zipper" siRNA used throughout this study. (B) Lipofection-mediated knockdown with 25 nM siRNA in Luciferase-expressing MDA-MB-231s. Luminescent signal was normalized to scrambled control siRNAs to account for any nonspecific toxicity effects. (C) Serum stability of siRNA challenged with 60% fetal bovine serum at 37°C visualized by agarose gel electrophoresis.

Valency of lipid-conjugated siRNA reportedly affects bioavailability and pharmacodynamics of siRNA conjugates *in vivo* [33, 34, 67]. Focusing on siRNAs conjugated to 18-carbon stearyl, an albumin-binding lipid with higher albumin affinity than those with shorter lipid tails[32, 68, 69]. we assessed the impact of stearyl valency on pharmacokinetics of our stabilized siRNA conjugates. Absolute circulation half-life ($t_{1/2}$) was measured using real-time fluorescence imaging of Cy5-labeled siRNA conjugates within mouse vasculature (**Fig. 2.2A**), revealing increased $t_{1/2}$ (46 ± 5.9 min) of siRNA conjugated to divalent (L_2) over monovalent (L_1) stearyl (28 ± 4.2 min) (**Fig. 2.2B,C**) Conversely, L_2-conjugated siRNA showed diminished kidney accumulation compared to siRNA-L_1 (**Fig. 2D**), suggesting that renal

clearance, the primary elimination mechanism of circulating siRNAs, is minimized with L_2-siRNA. The remainder of our studies, therefore, focused on a divalent lipid design.

Though the divalent lipid design displayed more favorable pharmacokinetics and biodistribution, the amount of conjugate that was albumin bound was comparable and relatively low for both conjugates (**Fig. 2.2E).** Previous work has suggested that optimization of linker length and hydrophilicity can be tuned to achieve higher albumin binding[30, 32, 68, 70]. However, this type of optimization has never been performed in the context of oligonucleotide delivery. To this end, we constructed a library of conjugates with progressively increasing number of hexaethylene glycol (EG) repeats between the branching moiety and the lipid tails (**Fig. 3**). We additionally synthesized two previously described serum protein-binding siRNA conjugates, cholesterol-TEG-siRNA[71-73] and si-PEG_{45}<L_2[74], as comparative references. Cholesterol-modified siRNAs have been well studied in the literature and are quickly incorporated into lipoprotein complexes such as low-density lipoprotein (LDL) and high density lipoprotein (HDL) after being introduced into the blood stream[75]. These lipoprotein complexes act as siRNA carriers to transport the cholesterol-siRNA conjugate to target tissues (predominantly the liver)[76]. The other control conjugate, si-PEG_{45}<L_2 was the first siRNA described in the literature that leveraged lipid-mediated albumin-binding to improve solid tumor delivery[63]. However, this work leveraged an siRNA that was vulnerable to nucleases and utilized a modifier that required two-step, solution-phase click-chemistry. This modifier was never optimized for use with a very hydrophilic, negatively charged molecule like siRNA[32], and contains bulky click chemistry groups and degradable esters. We therefore sought to further the field by filling the gaps in knowledge presented by these two comparative references.

Each candidate of the conjugate library was incubated with human serum albumin (HSA) to assess albumin-siRNA complex formation by an electrophoretic mobility shift assay. These studies

revealed that, while electrophoretic mobility of free siRNA was unaffected by albumin, the mobility si<$(EG_0L)_2$, si<$(EG_6L)_2$, si<$(EG_{18}L)_2$, and si<$(EG_{30}L)_2$ was lowered upon exposure to albumin (**Fig. 2.4A)** consistent with the high molecular weight of the complex formed by albumin and siRNA conjugates. Similarly, the two previously described lipid-siRNA conjugates, si-TEG-cholesterol, and si-PEG_{45}<L_2, also displayed albumin-dependent mobility shifts in this assay. However, mobility super-shifting of si-PEG_{45}<L_2 was seen in both the presence and absence of albumin, suggesting that si-PEG_{45}<L_2 may harbor some self-association properties which were not seen in si<$(EG_XL)_2$ conjugates. This agrees with previous literature findings that this modification pattern equilibrates between micellar and albumin-bound forms[32]. Similar results were observed using mouse serum albumin (**Supplemental Fig. 2.2**).

Albumin-binding kinetics of the si<$(EG_XL)_2$ variants were studied further using biolayer interferometry (**Fig. 2.4B**, **Supplementary Fig. 2.3**). As expected, free siRNA did not exhibit binding with HSA, while the previously described si-cholesterol exhibited moderate albumin binding. Although si<$(EG_0L)_2$ displayed a decreased HSA binding response compared to si-TEG-cholesterol, siRNA conjugates harboring a greater number of EG spacers within the linker element had progressively improved HSA binding kinetics, with both si<$(EG_{18}L)_2$ (Kd = 30 ± 0.3 nM) and si<$(EG_{30}L)_2$ (Kd = 9.49 ± 0.1 nM) exhibiting stronger albumin binding than si-TEG-cholesterol and si-PEG_{45}<L_2 (**Supplementary Fig. 2.3**).The substantial difference in albumin binding response between variants underscores the key role of the EG repeats within the linker region. Indeed, refinement of linker architecture was among the critical optimizations enabling high albumin-binding affinity for the peptide therapeutic Semaglutide, currently in clinical use[70].

Amphiphilic lipid-modified nucleic acids have a tendency to self-assemble into micellar structures[77-79], particularly when using long lipid chains. It is possible that self-aggregation of

amphiphilic siRNA-lipid conjugates is a competing interaction with albumin association, particularly if lipid tails can become sequestered in the core of a self-assembled structure, where they would be rendered unavailable for interaction with fatty acid binding pockets found in albumin (**Fig. 2.4C**). Thus, the critical micelle concentration (CMC) was determined for each si<$(EG_XL)_2$ to establish the impact of linker length on siRNA conjugate self-assembly (**Fig. 2.4D, Supplementary Fig. 2.4**). As expected, si-TEG-cholesterol exhibited a relatively high CMC (3430 ± 350 nM), suggesting a decreased tendency for cholesterol-conjugated siRNA to self-associate. This is consistent with the bulky structure of cholesterol, which is not amenable to close packing like lamellar long-chain lipids[80]. In contrast, the previously described albumin-binding conjugate si-PEG_{45}<L_2 exhibited a lower CMC (1860 ± 60 nM), indicating a higher tendency towards self-association. Interestingly, si<$(EG_0L)_2$, which lacks any EG spacer in the linker element, exhibited the lowest CMC (1040 ± 23 nM) and thus the highest propensity for self-association, while the increased number of EG repeats in si<$(EG_{18}L)_2$ and si<$(EG_{30}L)_2$ correlated with the highest CMCs (3260 ± 190 nM and 3330 ± 210 nM), and thus the lowest tendency towards self-association.

Modification of siRNAs with hydrophobic end groups can be used to engage and tune binding to serum proteins after intravenous administration, and the binding of different serum proteins has consequent impacts on pharmacokinetics and biodistribution [76, 81]. Serum protein albumin's exceptional half-life of 19 days, for instance, can be utilized to confer improved pharmacokinetics to therapeutics[14]. Intravenous delivery of each of the siRNA conjugates in mice was therefore used to understand how EG repeats within the linker affect pharmacokinetics of the siRNA conjugate. Intravital fluorescence microscopy of Cy5-labeled siRNA conjugates flowing through vessels of the mouse ear demonstrated the rapid and complete diminution of circulating free siRNA within the first 30 minutes post-treatment, while serum protein-binding si-TEG-cholesterol and si-PEG_{45}<L_2 retained some observable circulating

siRNA (**Figure 2.5A**). Interestingly, increased EG repeats correlated with increased retention of circulating siRNA in si<$(EG_XL)_2$ conjugates, but not indiscriminately, with the greatest fluorescence remaining in si<$(EG_{18}L)_2$ and si<$(EG_{30}L)_2$. This real-time collection of vascular fluorescence imaging data throughout the first hour post-treatment enabled calculation of absolute half-life ($t_{1/2\ abs}$), demonstrating the substantially prolonged $t_{1/2\ abs}$ of si<$(EG_{18}L)_2$, which was even greater than what was observed for si<$(EG_{30}L)_2$ **(Figure 2.5B)**, and nearly 5 times that of si<$(EG_0L)_2$ (**Supplementary Table 2.2**). Approximately 45 minutes after injection, there was significantly more renal accumulation, the primary clearance path for oligonucleotide-based therapeutics, of the parent siRNA and control conjugate, si-PEG_{45}<L_2 (**Fig. 2.5C, Supplementary Fig. 2.5**). We posit that the diminished renal clearance of the si<$(EG_XL)_2$ variants over si-PEG_{45}<L_2 is due to the hydrolytically degradable ester bonds located in the structure of DSPE-PEG_{2000}. Hydrolysis of this ester would be expected to release the siRNA from albumin, possibly prematurely in the circulation, resulting in renal clearance and shorter circulation time. Conjugates that remain albumin-bound, by comparison, can evade renal clearance through albumin's natural reabsorption in the renal proximal tubule where, after endocytosis by the megalin-cubilin complex, the neonatal Fc receptor redirects albumin and its associated cargo back to the interstitial space, facilitating its return to the circulation *via* the lymphatics [82-84].

Plasma was collected from mice treated intravenously with Cy5-labeled siRNA conjugate and analyzed by size exclusion chromatography to gauge which plasma proteins are most associated with the different conjugate structures in the blood (**Fig. 2.5D, Supplementary Figs. 2.6-7**). Cy5 fluorescence was detected in albumin-containing plasma fractions, as well as in fractions incompatible with albumin size exclusion. Notably, plasma isolated from mice treated with si<$(EG_{18}L)_2$, the most long-circulating of the investigated conjugates, exhibited the most robust peak within the albumin-containing fraction at

approximately 75% bound. This observation suggests a positive correlation between the amount of albumin-bound *in vivo* and circulation half-life.

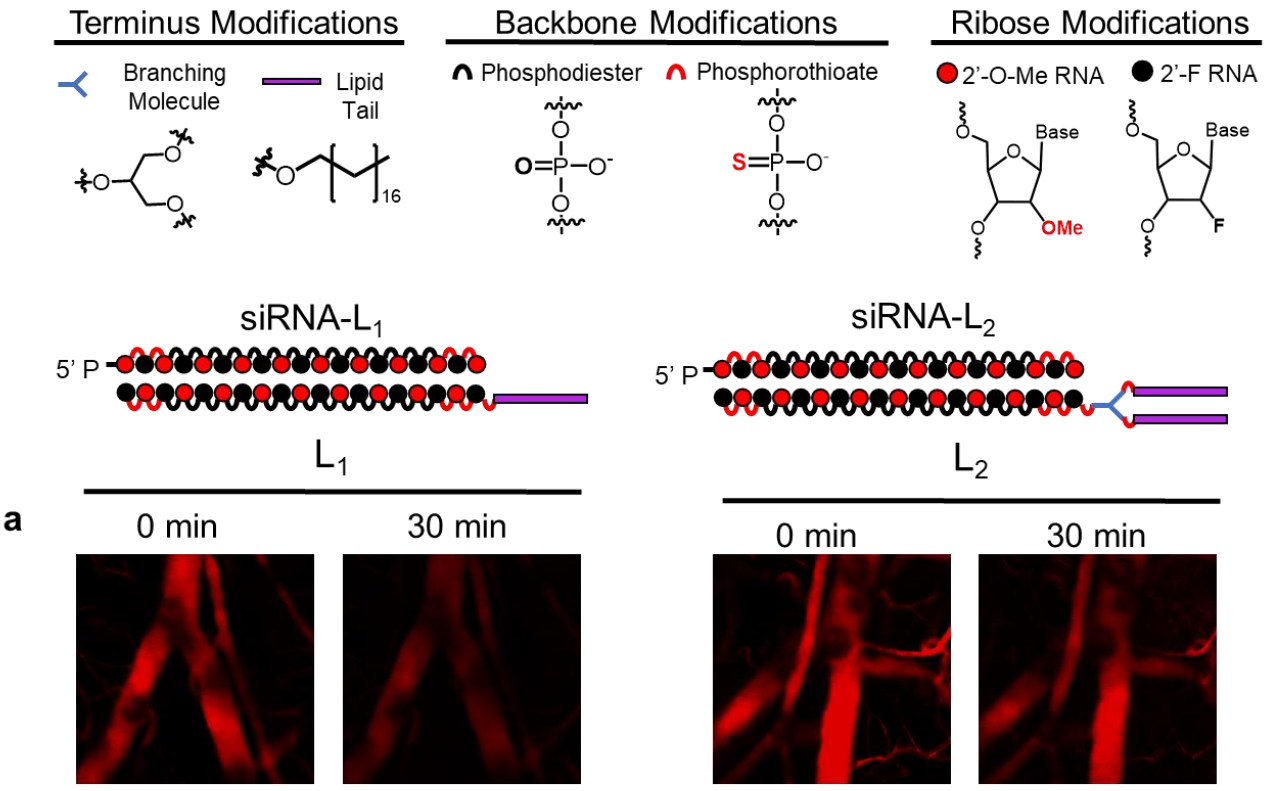

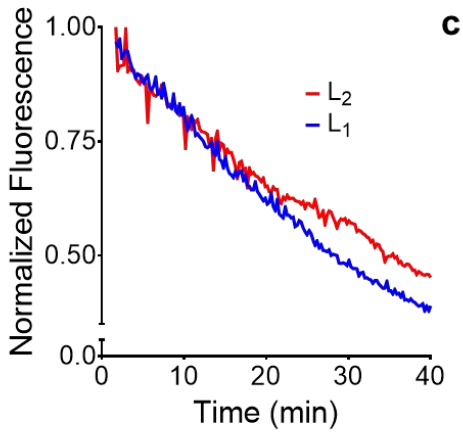

c

	$t_{1/2}$ (min)	$AUC_{0\text{-}40m}$ (μg•min)/(mL)	CL (mL)/(min)
siRNA-L_1	28 ± 4.2	430 ± 56	0.026 ± 0.0058
siRNA-L_2	46 ± 5.9**	440 ± 51	0.018 ± 0.0040

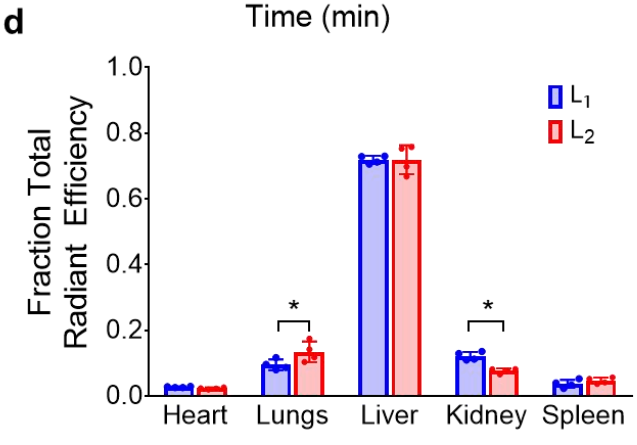

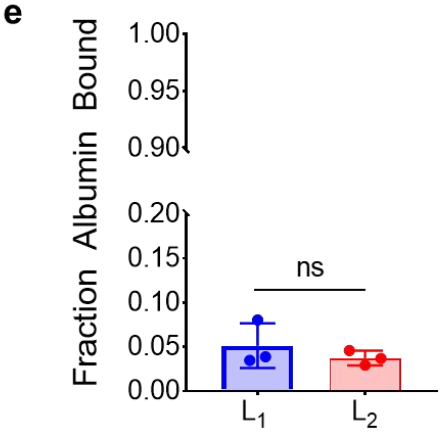

Figure 2.2*:* Divalent lipid-siRNA conjugate exhibits improved bioavailability compared to monovalent conjugateA) Representative intravital microscopy images of mouse ear vasculature monitored for fluorescence decay after i.v. injection of siRNA conjugate (1 mg/kg). B) Average of (n=4) intravital fluorescent signals from individual mice displayed. C) Pharmacokinetic parameters of siRNA conjugates determined by intravital microscopy (D) Biodistribution of fluorescent conjugates approximately 45 minutes after 1 mg/kg intravenous injection as measured by IVIS (n=4). Significance assessed by 2-way ANOVA with Sidak's multiple comparisons tests (E) Fraction of conjugate bound to albumin in mouse plasma after 1 mg/kg intravenous injection as calculated from known standards and sum of fractions' fluorescent intensities (n=3). Significance assessed using Welch's t-test.

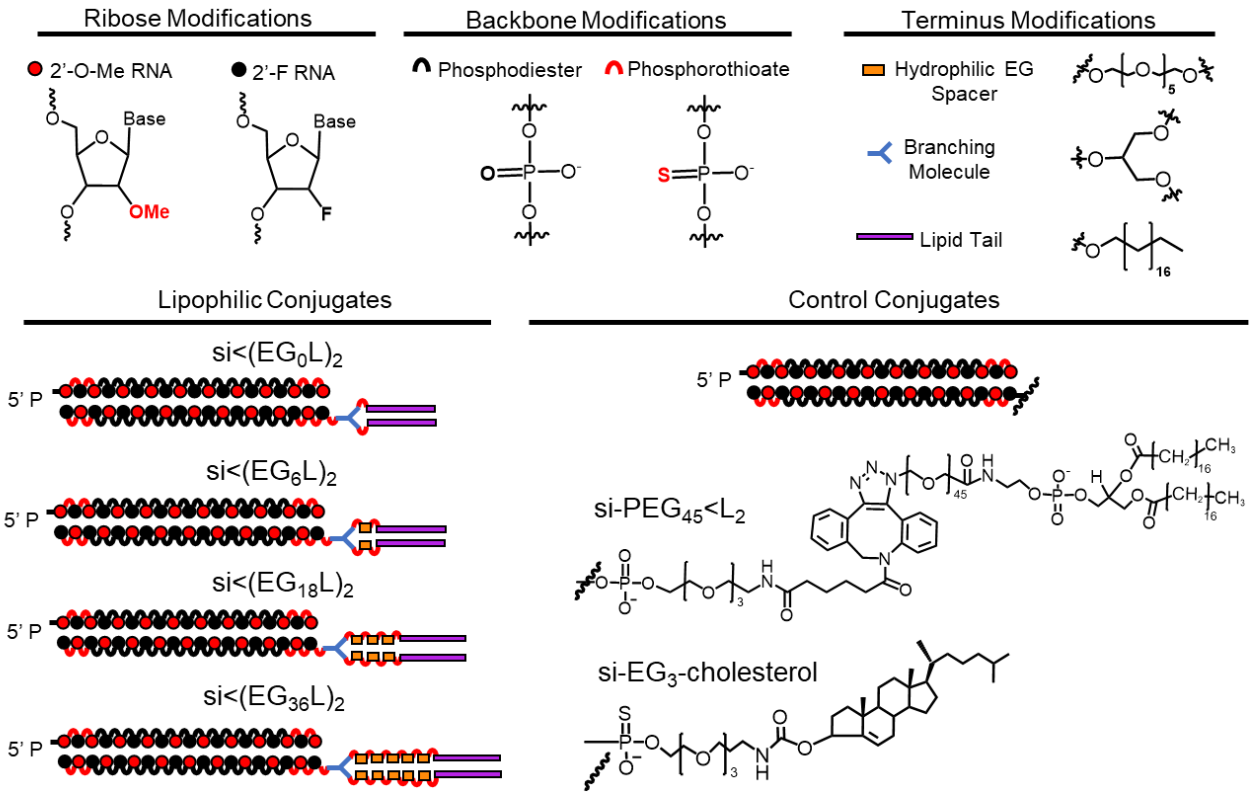

Figure 2.3 Library of chemically stabilized siRNA conjugates

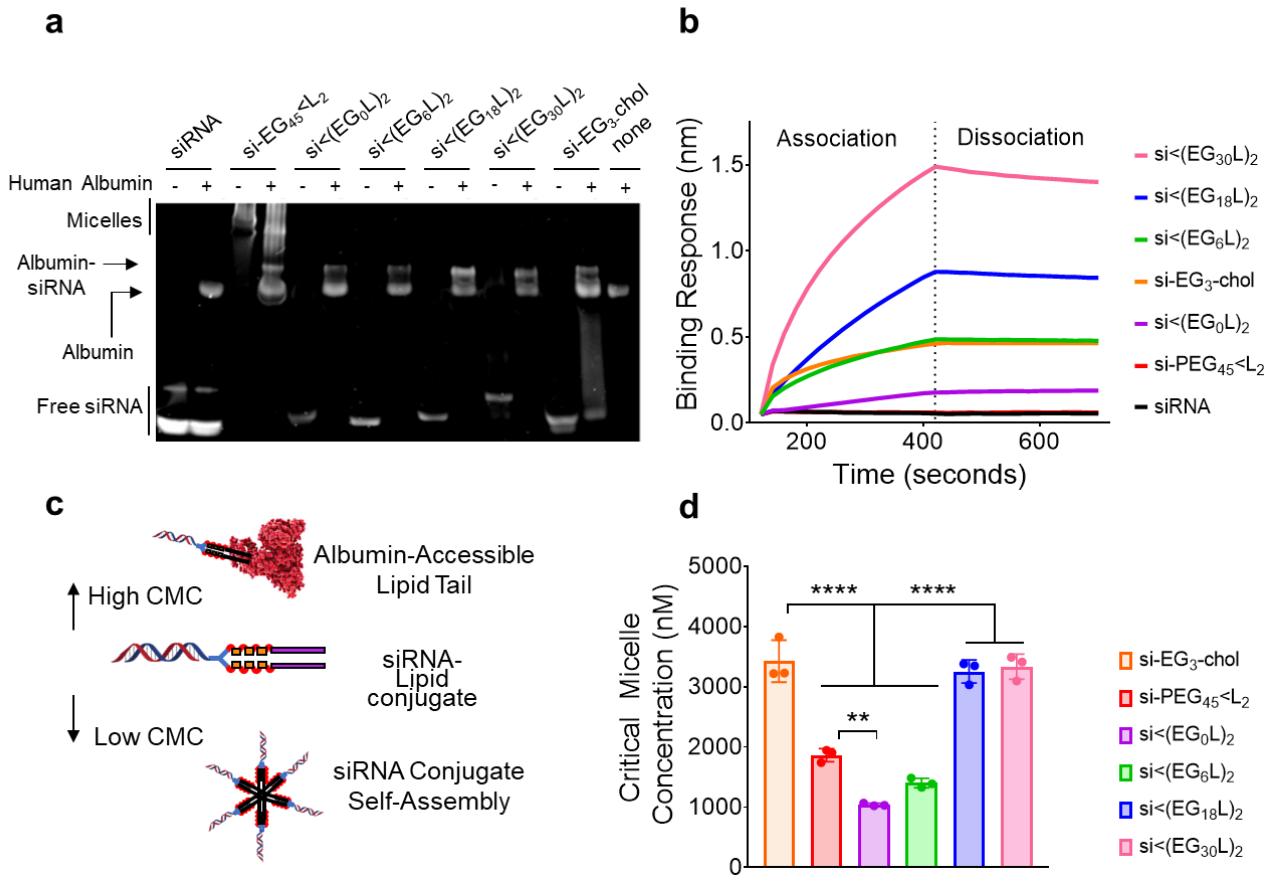

Figure 2.4: Hydrophilic linker length affects *in vitro* albumin-binding and micellar self-assembly of lipid- siRNA conjugates.(A) Native PAGE gel of siRNA conjugates run in the presence or absence of human serum albumin. Albumin association is indicated by an upwards shift of nucleic acid staining to coincide with the molecular weight increase from albumin binding. (B) Representative *in vitro* binding responses of siRNA conjugates to human serum albumin (400 nM) measured by biolayer interferometry. Dashed line represents transition from association to dissociation. (C) Proposed mechanism of competition between self-assembly and albumin binding of siRNA conjugates. (D) Critical micelle concentration of siRNA conjugates observed after 2 hours of incubation with Nile Red at 37°C (n=3). Significance assessed by one-way ANOVA with Tukey's multiple comparisons test.

It is interesting that *in vitro* albumin binding affinity analyses indicate that si<$(EG_{30}L)_2$ binds albumin more favorably than si<$(EG_{18}L)_2$ while albumin association *in vivo* is greater with si<$(EG_{18}L)_2$. This may be a result of the larger entropic penalty of binding incurred for this larger and more flexible

molecule that is mitigated by the ideal conditions of *in vitro* testing but becomes more apparent *in vivo*. This trend is also evident in testing against mouse serum albumin (**Supplementary Fig. 2.3**).

The observed positive correlation between hydrophilic linker length and albumin-bound siRNA *in vivo* enabled interrogation of potential correlations between conjugate albumin association and tumor accumulation. Luciferase (Luc)-expressing MDA-MB-231 TNBC cells were injected into the inguinal mammary fat pad to generate orthotopic tumors in female athymic mice. When tumors exceeded 50 mm^3, si<$(EG_XL)_2$ was delivered i.v. at 2.5 mg/kg on days 1, 3, and 5. On day 6, Cy5-labeled si<$(EG_XL)_2$ was delivered at 1 mg/kg, and Cy5 distribution to tumors and organs (kidney, liver, spleen, heart, lungs) was assessed on day 7, approximately 18 hours after final treatment (**Fig. 2.6**).

As expected, free Cy5-siRNA largely accumulated in the kidney, but not the tumor, resulting in a tumor to kidney fluorescence ratio of less than 0.05 (**Figure 2.6A**), which was modestly but not significantly increased in si-PEG_{45}<L_2 treated mice. However, progressively increased tumor fluorescence along with progressively decreased kidney fluorescence was seen in mice treated with si<$(EG_0L)_2$, si<$(EG_6L)_2$, and si<$(EG_{18}L)_2$, resulting in a tumor to kidney fluorescence ratio of 0.5, 0.9, and 1.0, respectively, suggesting that increased linker length potently affected siRNA tumor accumulation. These results are consistent with the increased albumin binding and increased circulation time seen with the si<$(EG_XL)_2$ constructs, as longer circulating siRNA conjugates are anticipated to enable higher tumor exposure and interaction with target cells [85, 86]. Interestingly, tumor to kidney fluorescence seen in mice treated with si<$(EG_{30}L)_2$ was lower than the other si<$(EG_XL)_2$ samples, again suggesting diminished albumin association *in* vivo results in lower tumor accumulation.

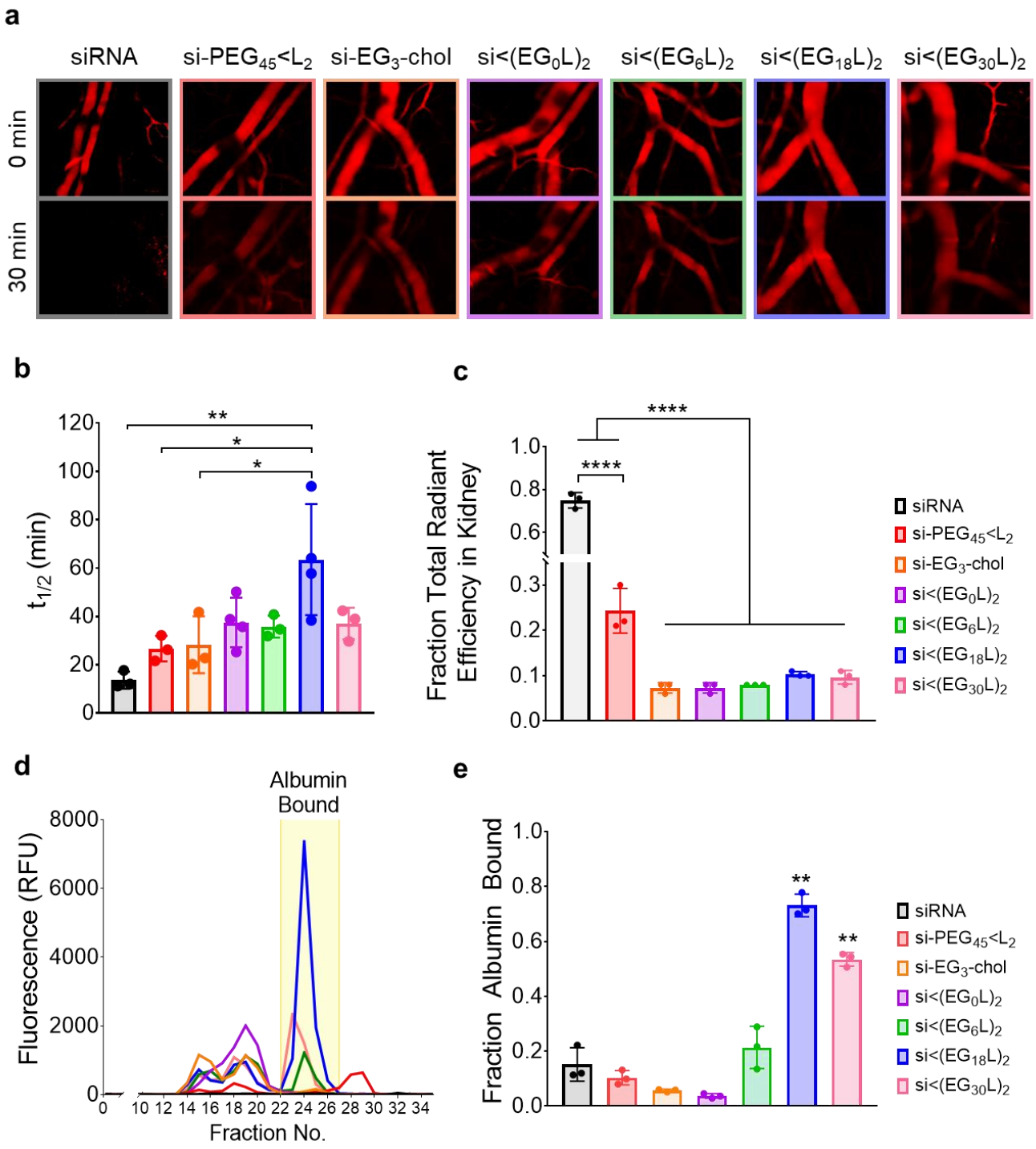

Figure 2.5: Hydrophilic linker length determines *in vivo* pharmacokinetics, biodistribution, and *in vivo* albumin-binding of lipid-siRNA conjugates.(A) Representative intravital microscopy images of mouse ear vasculature at T_{0min} and T_{30min}. (B) Conjugate absolute half-lives calculated from intravital microscopy fluorescent traces in vasculature (n=3-4). Significance assessed by 1-way ANOVA with Tukey's multiple comparisons test. (C) Kidney biodistribution of fluorescently labeled conjugates

approximately 45 minutes after 1 mg/kg intravenous injection (n=3). Significance assessed with 1-way ANOVA with Tukey's multiple comparison's test. (D) Representative fluorescent intensity traces of mouse plasma isolated approximately 45 minutes after 1 mg/kg intravenous injection separated into sequential fractions by size exclusion chromatography. (E) Fraction of conjugate bound to albumin in mouse plasma after 1 mg/kg intravenous injection as calculated from known standards and sum of fractions' fluorescent intensities (n=3). Significance assessed with 1-way ANOVA (Kruskal-Wallis) with Dunn's multiple comparisons test against control conjugate si-EG_{45}<L_2.

Importantly, at the end of the treatment regime, mice treated with si<$(EG_{18}L)_2$ targeting luciferase transgene showed nearly 80% reduction in tumor cell luciferase activity and protein amount compared to mice treated with a sham control (**Fig. 2.6B**). Indeed, si<$(EG_{18}L)_2$ also shows more than twice the silencing potency as previously reported albumin-binding construct si-PEG_{45}<L_2. Additionally, staining of tumor sections for the luciferase protein demonstrated robust spatial silencing throughout the field by the conjugate compared to parent siRNA and saline controls (**Fig 2.6C, Supplementary Fig. 2.8**).

Lead candidate si<$(EG_{18}L)_2$ was then synthesized to target endogenous oncogene Mcl-1. For added rigor, a single bolus was administered intravenously to mice bearing MDA-MB-231 tumors. Four days after treatment, relative Mcl-1 mRNA levels showed dose-dependent silencing, with 10 and 20 mg/kg injections achieving approximately 75% and 85% knockdown, respectively (**Fig. 2.6D**). This prompted us to examine if these higher doses could achieve sustained knockdown at a later time point as the tumor cells continued to proliferate. We administered these two higher doses and assessed relative Mcl-1 knockdown levels at 8d post-treatment, which, strikingly, showed that the knockdown was not significantly diminished (**Fig. 2.6E)**. These results suggest that the candidate holds promise as a therapeutic candidate that does not need to be administered more than once per week, as many current chemotherapies do. Our data indicates that the primary "off-target" organ for accumulation of our conjugate after i.v. injection is the liver. We therefore also sought to assess whether considerable off-target knockdown of liver Mcl-1 would be generated by these higher doses, but even at the highest dose

of 20 mg/kg siRNA, less than 20% silencing of liver Mcl-1 was observed compared to the 80% silencing achieved in the tumor (**Supplementary Fig. 2.9)**.

2.3 Conclusion

This work shows that systematic variation of lipophilic siRNA conjugate valency and linker length impacts albumin hitchhiking, pharmacokinetics, tumor biodistribution, and carrier-free gene silencing activity *in vivo*. The lipid valency, as previously reported [33, 34, 67], has a significant impact on pharmacokinetics. Based on these findings, we sought to optimize a divalent lipophilic siRNA conjugate for albumin binding. The addition of a hydrophilic linker improves albumin binding but not indiscriminately. Our data suggest that there is an optimal length of hydrophilic linker [si<$(EG_{18}L)_2$], and that studies identifying this conjugate also suggest there is a correlation between albumin bound *in vivo* and tumor gene silencing. Silencing was demonstrated of both transgene firefly luciferase and endogenous gene Mcl-1 in tumors. Importantly, silencing of endogenous gene Mcl-1 was sustained after a single bolus of siRNA at least eight days after intravenous injection, suggesting this platform could be administered less often than traditional chemotherapies.

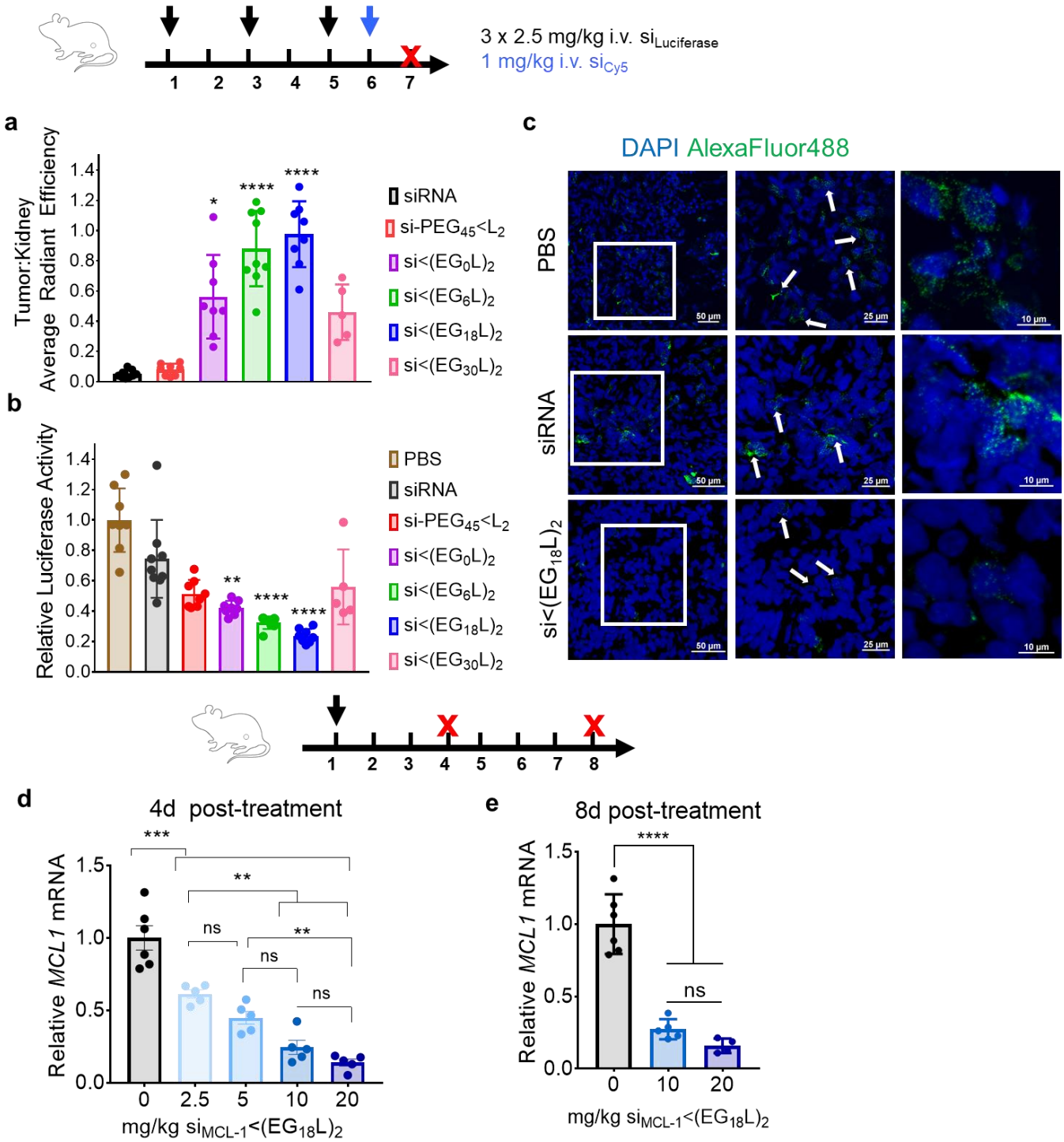

Figure 2.6: Albumin-binding increases tumor accumulation and carrier-free silencing of siRNA-lipid conjugates *in vivo* (A) Tumor:kidney ratio of fluorescently labeled conjugate injected via tail vein 18h before IVIS imaging (n=5-9). Significance assessed by 1-way ANOVA (Kruskal-Wallis) with Dunn's multiple comparisons test against siRNA control. (B) Luciferase activity of tumors normalized to saline treated controls measured *ex vivo* after 3 x 2.5 mg/kg injections via tail vein administration (n=5-9). Significance was assessed by 1-way ANOVA (Kruskal-Wallis) with Dunn's multiple

comparisons test against PBS control. (C) Representative images of tumor immunohistochemistry using AlexaFluor488-labeled Anti-Firefly Luciferase antibody after 3 x 2.5 mg/kg injections via tail vein administration. (D) Quantification of relative Mcl-1 mRNA levels after a single bolus injection of si_{Mcl-1}<$(EG_{18}L)_2$ both 4 days and (E) 8 days after treatment. Saline group replotted with 8d data but all significance tested together in a single 1-way ANOVA with Tukey's multiple comparison's test (n=4-6).

2.4 Materials and Methods

Reagents

2'-O-Me and 2'-F phosphoramidites and universal synthesis columns (MM1-2500-1) were purchased from Bioautomation. Symmetrical branching CED phosphoramidite was obtained from ChemGenes (CLP-5215). Cyanine 5 phosphoramidite (10-5915), stearyl phosphoramidite (10-1979), biotin TEG phosphoramidite (10-1955), hexaethyleneglycol phosphoramidite (10-1918), TEG cholesterol phosphoramidite (10-1976), and desalting columns (60-5010) were all purchased from Glen Research. All other reagents were purchased from Sigma-Aldrich unless otherwise specified.

Conjugate Synthesis, Purification, and Validation

Oligonucleotides were synthesized using modified (2'-F and 2'-O-Me) phosphoramidites with standard protecting groups on a MerMade 12 Oligonucleotide Synthesizer (Bioautomation). Sequences of siRNAs used can be found in **Supplementary Table 2.1**. Amidites were dissolved at 0.1M in anhydrous acetonitrile with the exception of 2'OMe U-CE phosphoramidite which utilized 20% anhydrous dimethylformamide by volume as a cosolvent and stearyl phosphoramidite which was dissolved in 3:1 dichloromethane:acetonitrile by volume. Coupling was performed under standard conditions, and strands were grown on controlled pore glass with a universal terminus (1 μmol scale, 1000Å pore size.)

Strands were cleaved and deprotected using 1:1 methylamine:40% ammonium hydroxide at room temperature for 2 hours. Lipophilic RNAs were purified by reversed-phase high performance liquid chromatography using a Clarity Oligo-RP column (Phenomenex) under a linear gradient from 85% mobile phase A (50 mM triethylammonium acetate in water) to 100% mobile phase B (methanol) or 95% mobile phase A to 100% mobile phase B (acetonitrile). Oligonucleotide containing fractions were dried using a Savant SpeedVac SPD 120 Vacuum Concentrator (ThermoFisher). Conjugates were then resuspended in nuclease free water and sterile filtered before lyophilization.

Conjugate molecular weight and purity was confirmed using Liquid Chromatography-Mass Spectrometry (LC-MS) analysis on a ThermoFisher LTQ Orbitrap XL Linear Ion Trap Mass Spectrometer. Chromatography was performed using a Waters XBridge Oligonucleotide BEH C18 Column under a linear gradient from 85% A (16.3 mM triethylamine – 400 mM hexafluoroisopropanol) to 100%B (methanol) at 45°C. First-generation conjugate, si-PEG_{45}<L_2, molecular weight was validated using MALDI-TOF mass spectrometry as previously reported [74] using 50 mg/mL 3-hydroxypicolinic acid in 50% water, 50% acetonitrile with 5 mg/mL ammonium citrate as a matrix. Mass and chromatographic characterization can be found in **Supplementary Figure 2.1**.

Purified oligonucleotide was resuspended in 0.9% sterile saline and annealed to its complementary strand by heating to 95°C and cooling stepwise by 15°C every 9 minutes until 25°C on a T100 Thermal Cycler (BioRad).

Biolayer Interferometry

Binding kinetics were measured by biolayer interferometry using an Octet RED 96 system (ForteBio). Duplexes labeled with TEG-Biotin on the 5’ terminus of the antisense strand were diluted to 500nM in Dulbecco’s phosphate buffered saline containing calcium and magnesium (DPBS $^{+/+}$) and

loaded on a Streptavidin Dip and Read Biosensor (ForteBio) for 600s. Baseline was then established over 120 seconds in DPBS $^{+/+}$. Association to either human or mouse serum albumin (1.6 µM, 0.8 µM, 0.4 µM, 0.2 µM, 0.1 µM, 0.05 µM, 0.025 µM, 0 µM) in DPBS $^{+/+}$ was then measured over 300 seconds. Subsequently the biosensor was immersed in DPBS $^{+/+}$ for 300 seconds to measure dissociation. All steps were conducted at 30°C and 1000 rpm. The binding values were measured using Octet Data Analysis HT Software. Reference biosensor values (biotinylated conjugate bound with no analyte) were subtracted to account for non-specific binding. Y axes were aligned to the average of the baseline step. Interstep correction was performed by aligning to the dissociation step, and noise filtering was performed. Global analysis was performed to derive constants simultaneously from all available analyte concentrations.

Cell Culture

Cells were cultured in Dulbecco's modified eagle's medium (DMEM, Gibco), containing 4.5 g/L glucose, 10% FBS (Gibco), and 50 µg/mL gentamicin. All cells for this manuscript were tested for *Mycoplasma* contamination using MycoAlert Myocplasma Detection Kit (Lonza).

In Vitro Knockdown Experiments

Luciferase-expressing MDA-MB-231s were seeded at 4,000 cells per well in 96 well plates in complete media. After 24 hours, cells were treated with siRNA (25nM) using Lipofectamine 2000 (ThermoFisher) in OptiMEM according to manufacturer protocol, replacing with complete media at 24 hours post-transfection, and measuring luciferase activity at 48 hours post-transfection in cells treated for 5 minutes with 150 µg/mL D-Luciferin, potassium salt (ThermoFisher) using an IVIS Lumina III imaging system (Caliper Life Sciences).

Critical Micelle Concentration

A serial dilution of duplexes was prepared in a 96-well plate from 20 µM to 10 nM in 50 uL of DPBS (Ca^{2+}/Mg^{2+} free). Nile Red (1 µL of a 0.5 mg/mL stock solution) was added to each well. Samples were then incubated in the dark with agitation at 37°C for 2 hours, and fluorescent intensity was measured on a plate reader (Tecan Infinite F500) at excitation 535 +/- 10 nm and emission 612 +/- 10 nm. The CMC was defined, as previously described [87], as the intersection point on the plot of the Nile red fluorescence versus the duplex concentration.

Serum Stability and Gel Migration Shift Experiments

siRNA (0.1 nmol) in 60% fetal bovine serum in PBS was incubated at 37° for 0-48 hours, then assessed on a 2% agarose gel in 1X TAE Buffer. Gels were stained with GelRed Nucleic Acid Stain (Biotium) according to the manufacturer's protocol. Binding of siRNA conjugates (0.1 nmol) to human or mouse serum albumin (in 5X molar excess) incubated for 30 min at 37°C was assessed by migration through 4%-20% polyacrylamide gels (Mini-Protean TGX). siRNA was visualized with GelRed Nucleic Acid Stain (Biotium) for ultraviolet imaging, and proteins visualized with Coomassie blue and visible light imaging.

Intravital Microscopy and Biodistribution

Microscopy was performed using a Nikon Czsi+ system with a Nikon Eclipse Ti-oE inverted microscopy base, Plan ApoVC 20× differential interference contrast N2 objective, 0.75 NA, Galvano scanner, and 543 dichroic mirror. All image analysis and acquisition were done using Nikon NIS-Elements AR version 4.30.01. A laser gain of 98 was used throughout. Isofluorane-anesthetized, 6-8

week old male CD-1 mice (Charles River) were immobilized on a heated confocal microscope stage for ear vein imaging. Mouse ears were depilated then immobilized on a glass coverslip using microscope immersion fluid. Ear veins were detected using light microscopy, and images were focused to the plane of greatest vessel width, where flowing red blood cells were clearly visible. Once in focus, confocal laser microscopy was used to acquire one image per second, at which point Cy5-labeled siRNA (1 mg/kg) in 100 µL was delivered via tail vein. Fluorescent intensity within a circular region of interest drawn in the focused vein was used to measure fluorescence decay. Values are normalized to maximum initial fluorescence and fit to a one-compartment model in PK Solver to determine pharmacokinetic parameters.

Approximately 45 minutes after delivery of Cy5-labeled siRNA, blood was collected by cardiac puncture using EDTA-coated plasticware and used for plasma collection. Cy5 fluorescence was quantified in heart, lung, liver, kidney, and spleen using IVIS Lumina Imaging system (Xenogen Corporation) at excitation and emission wavelengths of 620 and 670 nm, respectively, using Living Image software version 4.4.

Size Exclusion Chromatography (SEC) Assessment of Protein Binding in Plasma of i.v. Treated Mice

Murine plasma was filtered (0.22 um) then injected into an AKTA Pure Chromatography System (Cytiva) with three inline Superdex 200 Increase columns (10/300 GL) for fractionation at 0.3 mL/min using Tris running buffer (10mM Tris-HCl, 0.15M NaCl, 0.2% NaN_3) into 1.5 mL fractions with a F9-C 96-well plate fraction collector (Cytiva). Cy5 fluorescence was measured in fractions (100 uL) in black, clear-bottom, 96-well plates (Greiner-Bio-one REF 675096) on a SynergyMx (Biotek) at a gain of 120, excitation 642/9.0, emission 675/9.0. Fraction albumin-bound conjugate was determined by taking the sum of fluorescent intensity for fractions associated with albumin elution divided by the sum of

fluorescent intensity for all fractions collected. Albumin-associated fractions were determined by running known protein standards through the SEC system and examining A280 of eluent from each of the fractions (**Supplementary Fig. 3**).

Orthotopic Mammary Tumor Studies

Luciferase-expressing MDA-MB-231 cells (1 x 10^6) in 100 uL of 50% Matrigel were injected into the inguinal mammary fat pads of 4-6 week old female athymic Balb/C (*nu/nu*) mice (Envigo). Mice were randomized into treatment groups when tumors reached 50 mm^3. Mice were treated once every 2 days with 2.5 mg/kg (based on parent siRNA molecular weight) luciferase-targeting siRNA until day 7, for a total of 3 treatments. Mice were euthanized and organs collected at necropsy for measurements of biodistribution (as described above) and for molecular histological analysis. Tumors were minced and either flash frozen in liquid nitrogen for downstream assays or embedded in OCT and frozen for sectioning.

In Vivo Tumor Gene Silencing

Tumor fragments (200-300 mg) were lysed for one hour on ice with agitation in 1X Reporter Cell Lysis Buffer (Promega) and then centrifuged at 14,000 X g for 15 minutes at 4°C. Protein concentration was then quantitated using BCA Assay (Pierce). Lysates (20 mg per well) were assessed in 96-well plates using 90 ml reconstituted Luciferase Assay Substrate according to manufacturer's directions. Luminescence was measured using IVIS grid quantitation.

Mcl-1 mRNA was measured in MDA-MB-231 tumors using QuantiGene SinglePlex assay (Thermo Fisher). Tumors were harvested and stored in RNAlater (Thermo Fisher) at 4°C. Tumors were dissociated in RNAlater in GentleMACS C-tubes (Miltenyi Biotec), washed twice with water, then

digested for 6 h at 55°C in Quantigene Diluted Lysis Mixture (DLM) supplemented with proteinase K (0.25 mg/ml) using 2 mls DLM per gram of tumor. Tissue lysates were diluted 1:2 for Quantigene assessment with manufacturer-designed probe sets directed against human *MCL1* and human *PPIB*. Luminescence generated from each specific probe set was measured and quantified on a plate reader (Tecan). Each sample was assessed in 5 technical replicates. Values shown are the ratio of *MCL1* (corrected for the loading control, *PPIB*). All values shown are relative to the average *MCL1* level observed in tumors from saline-treated mice.

Cryosectioning, Immunofluorescence, and Confocal Microscopy of Tumor Sections

Samples were snap frozen in OCT embedding medium and stored at -80ºC until processing for cryosectioning. Samples were serially sectioned until an adequate depth was reached for optimal visualization. Cryosections at various depths along the tumor were then sectioned at 6 µm thickness, captured, and placed on a slide. Slides were then processed immediately using ProLong Gold Antifade Mountant with DAPI with a cover slip or fixed in 4% paraformaldehyde for 10 minutes before immunofluorescence staining was done using a rabbit anti-firefly luciferase (anti-Fluc antibody, Abcam, ab185924; 1:500) primary antibody overnight and a goat anti-rabbit Alexa Fluor® 488 (ab150077, Abcam; 1:500) secondary antibody for 1 hour in the dark; blocking was performed with donkey serum. Stained slides were counterstained with DAPI and imaged on a Nikon Eclipse Ti inverted confocal microscope. Imaging settings were kept constant across different treatment groups.

Statistical Analyses

Data were analyzed using GraphPad Prism 7 software (Graphpad Software, Inc.) Statistical tests used for data can be found in corresponding figure legends. For all figures, * $p \leq 0.05$ ** $p \leq 0.01$ *** $p \leq 0.001$ **** $p \leq 0.0001$. All plots show mean ± standard deviation.

Chapter 3: Interrogation of Structure-Function Relationship of Albumin-Binding siRNA Conjugates

3.1 Introduction

The studies discussed in Chapter 2 underscore that the optimization of individual structural features such as a hydrophilic linker have a significant impact on the performance of siRNA conjugates *in vivo*. These findings motivated the interrogation of further structural features within our lead conjugate to determine what components are critical to efficacy and determine if further optimization of these elements is warranted. Self-assembly was previously investigated in Chapter 2 as it relates to the hydrophilic linker element of our construct. However, a large distinction between previously reported si-PEG_{45}<L_2 and our new construct, si<$(EG_{18}L)_2$ is the branching architecture of these two conjugates. The diacyl lipid of si-PEG_{45}<L_2 closely links the two lipid chains together. This may in turn sterically hinder binding of the individual lipid chains to albumin or facilitate the self-assembly of these structures which we previously posited may compete with albumin binding. We therefore sought to investigate whether this specific feature was important to the performance of our newly optimized conjugate.

Additionally, each component of the lipid modifier that was added to the conjugate was linked by a phosphorothioate (PS), rather than a phosphodiester (PO), bond. As previously mentioned, inclusion of PS bonds at the termini of siRNA duplexes has been demonstrated to have a significant impact on the vulnerability of the duplexes to degradation by exonucleases. However, PS bonds themselves have been implicated in the binding of oligonucleotides to serum proteins[88] as well as their biodistribution and efficacy after systemic administration[89]. We therefore additionally iterated the PS

content of the albumin-binding moiety in our lead conjugate to uncover what effects, if any, it has on the efficacy of the construct.

Our siRNA optimization to this point has focused on the use of an 18-carbon stearyl, a lipid chain which has been shown to bind to albumin with higher affinity than shorter alkyl chains[32, 69]. However, there is a body of evidence which suggests that the carboxyl group of fatty acids that is typically consumed as a conjugation handle is critical to albumin binding[90]. The carboxyl group on native fatty acids drives a combination of electrostatic and hydrogen bonding interactions with albumin[91-93]. Albumin-binding GLP1 agonist peptide drug Semaglutide was dramatically improved by adopting this modification, resulting in half-life extension from 12.4h to 46.1h in mini-pigs[70]. We therefore sought to determine whether a siRNA conjugate that kept this group intact would demonstrate improved albumin affinity and better *in vivo* performance.

In Chapter 2, we posit that self-assembly of siRNA conjugates competes with albumin binding. Amphiphilic structures containing saturated, long chain lipids are well documented to pack into self-assembled structures[32, 77]. The cis-double bond(s) in unsaturated fatty acids such as oleic acid, however, introduce a "kink" in their shape which makes it more difficult to pack their molecules together[94, 95]. Additionally, studies show that oleoyl (C18 with double bond at ω-9) associates predominantly with albumin, not HDL, and has higher albumin binding affinity over stearate (its saturated C18 counterpart) and palmitate (C16), whereas the presence two double bonds lowers albumin affinity[96, 97]. We therefore hypothesized that replacing the stearyl in our lead conjugate with an oleoyl may improve albumin binding by reducing self-assembly.

To gain insight into the necessity of a reversible association between albumin and siRNA, we also sought to synthesize a covalently bound siRNA-albumin control. Currently, we do not yet understand if our siRNA conjugates are albumin-associated when they are taken up by tumor cells or if

they mostly rely on albumin as a means to reach the target tissue only. Additionally, as described in the introduction, there are reports that covalent modification of albumin can cause it to be preferentially trafficked to the degradative GP 18/GP30 pathway rather than the GP 60 pathway that promotes systemic recycling. We therefore also sought to glean insight into whether reversible association is required to prevent endogenous albumin from acquiring conformational modifications that would remove it from the circulation.

3.2 Results and Discussion

Structural interrogation of lead siRNA conjugate si<$(EG_{18}L)_2$ was first focused on whether the phosphorothioate (PS) content at the terminus with the albumin-binding moiety affects *in vitro* and *in vivo* properties. Variants of si<$(EG_{18}L)_2$ with PS bonds removed from the 5' sense terminus [si<$(EG_{18}L)_2$ No 5'Se PS] or from both the 5' sense terminus and each of the bonds in the albumin-binding moiety [si<$(EG_{18}L)_2$ No 5'Se or Binder PS] (**Figure 3.1A**) were synthesized and studied using biolayer interferometry to determine albumin binding kinetics (**Figure 3.1B, Supplementary Fig. 3.1**). Both variants exhibited comparable albumin affinity as the parent construct with KD values only varying +/- 2 nM. However, removing the PS bonds from the entire albumin-binding terminus significantly increased the critical micelle concentration compared to just removing it from the 5' sense terminus of the siRNA (2755 ± 526 to 3798 ± 225 nM), suggesting a lower tendency to self-assemble without the more hydrophobic PS bonds located on the binder (**Figure 3.1C)**.

Real time microscopy of fluorescently labeled conjugates in circulation was performed to determine the effect of PS content on circulation time. Removal of PS bonds from both the 5' sense terminus and the 5' sense terminus/binder resulted in significantly diminished pharmacokinetic profiles compared to parent construct si<$(EG_{18}L)_2$ (**Fig. 3.1D**) with circulation half-lives reduced to 37 ± 12

minutes and 15 ± 1.5 minutes respectively from 64 ± 23 minutes. Biodistribution of conjugates approximately 45 minutes after treatment demonstrated significant differences in PS-dependent accumulation in both the lungs and the liver (**Figure 3.1E**). Plasma was collected from mice treated intravenously with each siRNA conjugate to examine proteins bound *in vivo*. Removal of PS bonds in the albumin binding moiety resulted in 10-fold lower relative albumin binding by the siRNA conjugate relative to si<$(EG_{18}L)_2$ with and without PS bonds at the 5' sense terminus (**Fig. 3.2F**). These combined data suggest that PS-driven albumin-binding drives the observed differences in pharmacokinetics. This observation underscores the importance of PS incorporation into siRNA therapeutics.

The comparable level of albumin-binding *in vivo* between our lead construct and its variant without the phosphorothioate bonds at the siRNA terminus proximal to the albumin-binding moiety motivated us to further interrogate their functional differences in a tumor-bearing mouse model **(Fig. 3.2)**. Mice bearing Luciferase (Luc)-expressing MDA MB 231 tumors were treated every other day with 2 mg/kg of siRNA conjugate for a total of 3 treatments over the course of one week. Approximately 18h prior to sacrifice, mice were injected with a fluorophore-labeled version of each of the constructs (1 mg/kg) for determination of biodistribution and tumor cell uptake. The biodistribution of the two conjugates was comparable, with the only significant difference being a reduced level of liver accumulation with the elimination of the two PS bonds at the 5' sense terminus (**Fig. 3.2A)**. Flow cytometry of the tumor cells also showed similar uptake of the two constructs (**Fig. 3.2B).** However, si<$(EG_{18}L)_2$ with no 5' sense PS bonds exhibited significantly diminished tumor gene silencing. Whereas our lead construct demonstrated nearly 70% knockdown of the target gene, the elimination of the 5' sense PS bonds resulted in only about 20% knockdown (**Fig. 3.2C)**. The comparable biodistribution and uptake of both compounds but large disparity in knockdown suggests that these bonds are not degraded during circulation and extravasation. Rather, we hypothesize that, upon uptake,

these bonds are degraded and no longer link the siRNA to its divalent lipid tail. This in turn may impede interactions with cell membranes.

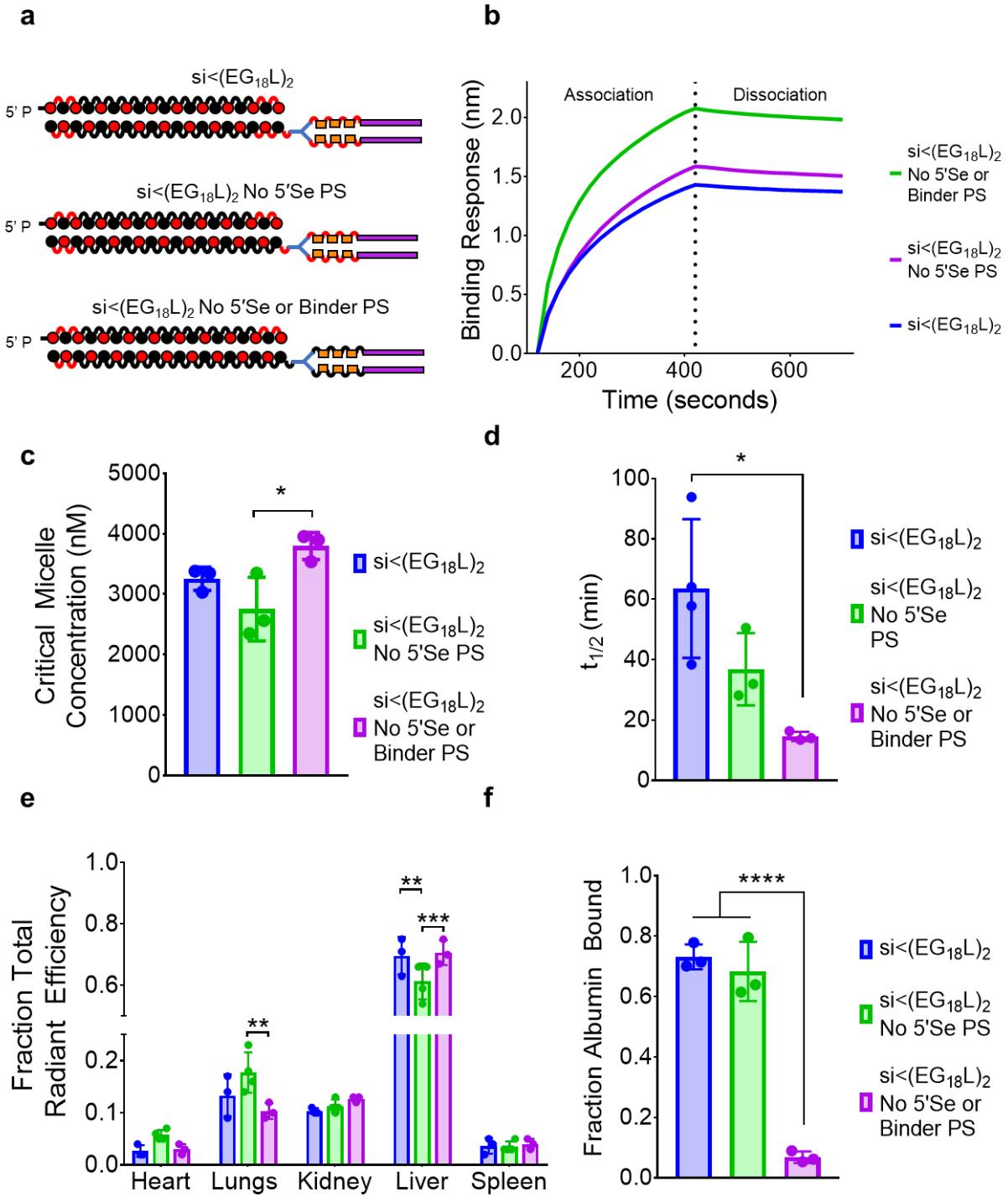

Figure 3.1: Inclusion of 5′ sense strand and linker phosphorothioate (PS) bonds maximizes performance of lipid-modified siRNA conjugate *in vitro* and *in vivo*.(A) Structural PS variants of lead si<$(EG_{18}L)_2$ conjugate investigated. (B) Representative *in vitro* binding responses of PS variants to human serum albumin (400 nM) measured by biolayer interferometry. Dashed line represents transition from association to dissociation. (C) Critical micelle concentration observed after 2-hour incubation

with Nile Red at 37°C (n=3). Significance assessed by 1-way ANOVA with Tukey's multiple comparisons test. (D) Absolute circulation half-life measured by intravital microscopy (n=3-4). Significance assessed by 1-way ANOVA with Tukey's multiple comparisons test. (E) Organ biodistribution of conjugates measured by IVIS approximately 45 minutes after 1 mg/kg tail vein injection. Significance assessed by 2-way ANOVA with Tukey's multiple comparisons test. (F) Fraction of albumin-bound conjugate in plasma isolated from mice approximately 45 minutes after i.v. injection (n=3). Significance assessed by 1-way ANOVA with Tukey's multiple comparisons test.

To further interrogate this hypothesis, we synthesized several additional variants of our lead construct. There have been reports suggesting that including two repeats of thymidine (dT_2), a DNA nucleotide, linked by phosphodiester bonds before a lipidic moiety can cause targeted cleavage from siRNA after internalization[89]. We therefore created an analogous iteration of our construct using this linker, si-(dT_2)<$(EG_{18}L)_2$, to assist in elucidating the effects of cleavage of the albumin binding moiety from the siRNA after internalization. Similarly, disulfide linkers have been used in the context of macromolecule delivery to achieve intracellular release of therapeutics. The cytosolic and endolysosomal compartments are thought to cause environmentally responsive disulfide reduction[98]. This paradigm motivated us to additionally synthesize our construct with a disulfide linker between the siRNA and the albumin binding moiety [si-(S-S)<$(EG_{18}L)_2$]. Finally, to more precisely define the role of the lipid within our structure, we included a variant of our lead candidate with the two C_{18} lipid tails removed from the structure [si<$(EG_{18}L)_2$].

Conjugate variants were tested for their accumulation and tumor-gene silencing in Luc-expressing MDA-MB-231 tumor bearing mice. Conjugates targeting Luciferase were administered intravenously every other day at a dose of 2 mg/kg for a total of three injections. Mice were additionally treated with 1 mg/kg of a non-targeting, fluorescently labeled version of each conjugate 18h prior to sacrifice.

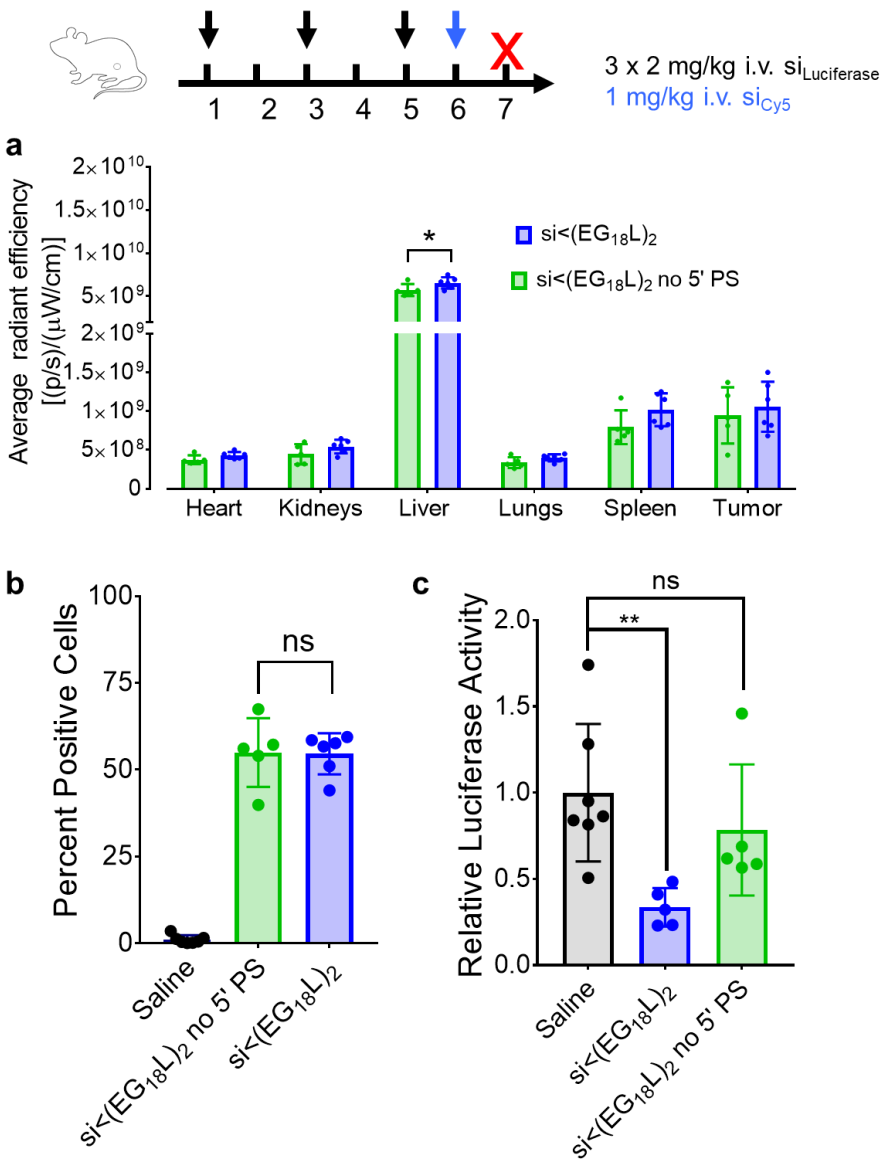

Figure 3.2: Phosphorothioate bonds at the siRNA terminus proximal to the albumin-binding moiety are critical to carrier-free tumor gene silencing

(A) Biodistribution of Cy5-labeled siRNA conjugates measured by epifluorescence 18 h after 1 mg/kg intravenous injection. Significance assessed by 2-way ANOVA with Tukey's multiple comparisons (n=4-6). (B) Percent Cy5 positive tumor cells determined by flow cytometry (C) Relative luciferase activity of tumor lysates after 3 x 2 mg/kg intravenous injections of siRNA conjugates targeting firefly luciferase over the course of one week. Significance assessed by 1-way ANOVA with Tukey's multiple comparisons (n=4-7).

Fluorescent imaging of the organs showed comparable gross accumulation of the two "cleavable" conjugate iterations compared to the parent construct (**Fig. 3.3A)**. As expected, si<$(EG_{18})_2$ demonstrated significantly greater kidney accumulation, which can be attributed to the loss of lipid-mediated serum component binding and subsequent inability to evade renal clearance. Flow cytometry of tumor cells showed significantly more conjugate-positive cells in mice treated with the lead construct compared to the variants with a (dT_2) linker or lacking lipid tails (**Fig. 3.3B**). However, all three iterations demonstrated diminished tumor-gene silencing compared to parent construct si<$(EG_{18}L)_2$ (**Fig. 3.3C**). This observation further supports our hypothesis that intact lipid tails are critical to achieving tumor gene silencing, rather than impeding the process.

We then sought to determine whether the position of the branching point in the divalent si<$(EG_{18}L)_2$ conjugate influences *in vitro* and *in vivo* outcomes. This study was motivated by the desire to further explore the hypothesis that albumin association is driven by a reduced tendency to self-assemble rather than simply the relative level of conjugate hydrophilic linker content or linker length. We posit that placement of this branching point proximal to the lipids promotes self-assembly and apparent hydrophobicity by sterically confining the lipids together. Since the greatest siRNA circulation time and tumor accumulation was seen with the si<$(EG_{18}L)_2$ conjugate, which correlated with increased albumin binding *in vivo*, two additional iterations of si<$(EG_{18}L)_2$ were generated, one matched for overall ethylene glycol content (si-EG_{36}<L_2) and one matched for the distance between the siRNA and its lipid tail (si-EG_{18}<L_2) (**Fig. 3.4A)**. As before, biolayer interferometry was performed to measure albumin binding *in vitro*. Interestingly, both variants showed diminished albumin binding responses *in vitro* relative to the parent construct si<$(EG_{18}L)_2$ (**Fig. 3.4B**). The critical micelle concentration was measured by Nile Red encapsulation, and both si-EG_{18}<L_2 and si-EG_{36}<L_2 exhibited significantly lower

critical micelle concentrations (1838 ± 117 and 2293 ± 132 nM) compared to si<$(EG_{18}L)_2$ (3255 ± 192 nM) (**Fig. 3.4C)**, suggesting that branching architecture directly impacts the tendency of amphiphilic siRNA conjugates to self-assemble.

Intravital microscopy of circulating fluorescent conjugates was performed to examine pharmacokinetics. Interestingly, there was not a significant difference in absolute circulation half-life among the branching architecture variants (**Figure 3.4D**). However, biodistribution of the fluorescently labeled conjugates approximately 45 minutes after administration revealed significantly higher liver accumulation of si-EG_{18}<L_2 and si-EG_{36}<L_2 compared to si<$(EG_{18}L)_2$ (**Figure 3.4E**). This observation may be explained by a tendency to bind a greater fraction of lipoproteins over albumin *in vivo* which can preferentially traffic the conjugates to the liver [81]. Indeed, plasma isolated from mice treated with the conjugates and analyzed by size exclusion chromatography for associated proteins demonstrated significantly decreased albumin binding among branching architecture variants si-EG_{18}<L_2 and si-EG_{36}<L_2 compared to si<$(EG_{18}L)_2$ from about 75% to less than 5% (**Fig. 3.4F**). This is further supported by the observation that the half-lives of si-EG_{18}<L_2 and si-EG_{36}<L_2 were not significantly different than si<$(EG_{18}L)_2$, suggesting that their half-life extension is due to association with alternative serum components other than albumin such as lipoproteins.

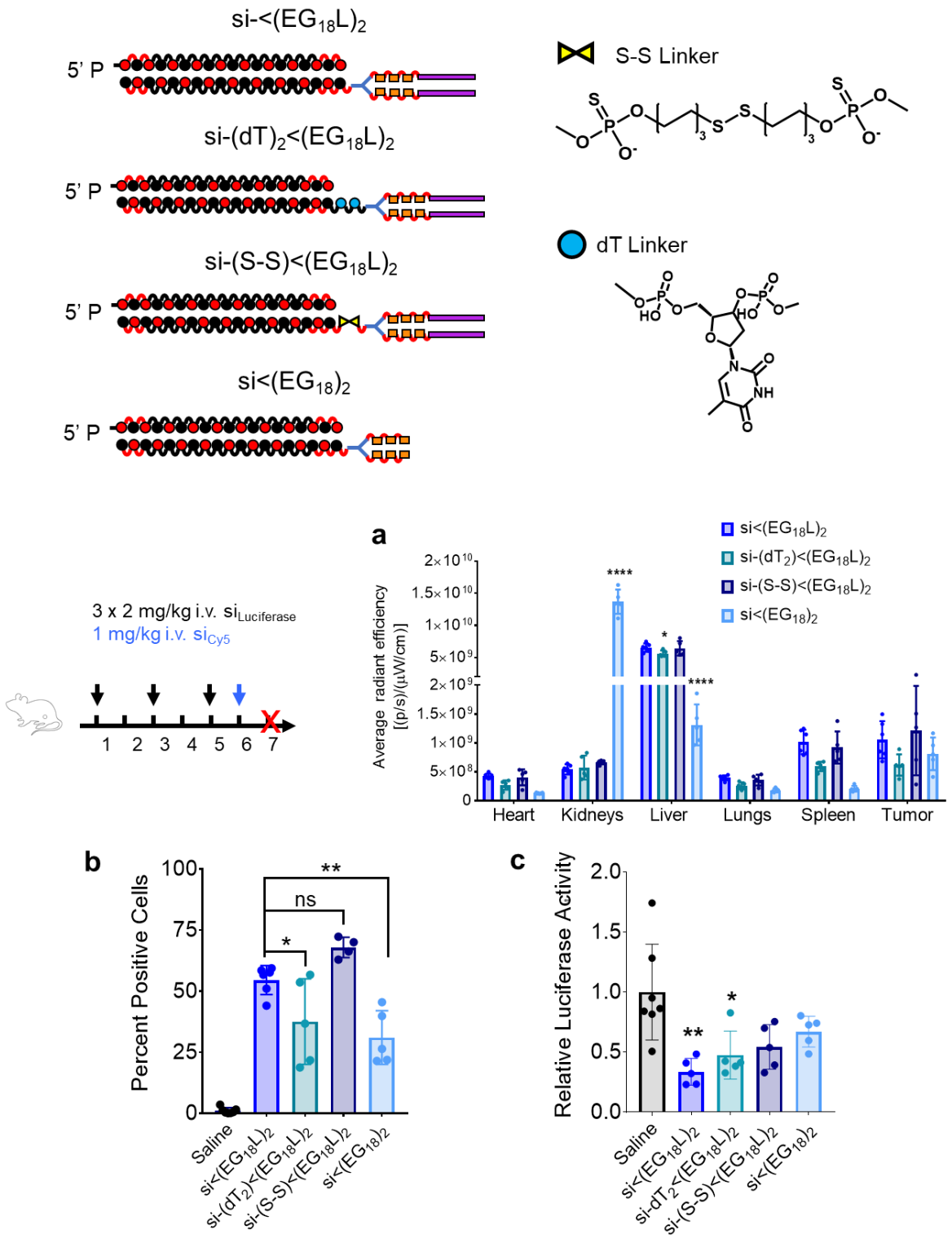

Figure 3.3: Intact lipid tails are critical to conjugate *in vivo* efficacy

(A) Biodistribution of Cy5-labeled siRNA conjugates measured by epifluorescence 18 h after 1 mg/kg intravenous injection. Significance assessed by 2-way ANOVA with Tukey's multiple comparisons

(n=4-6). Significance compared to si<$(EG_{18}L)_2$ displayed. (B) Percent Cy5 positive tumor cells determined by flow cytometry (C) Relative luciferase activity of tumor lysates after 3 x 2 mg/kg intravenous injections of siRNA conjugates targeting firefly luciferase over the course of one week. Significance assessed by 1-way ANOVA with Tukey's multiple comparisons (n=4-7). Significance compared to si<$(EG_{18}L)_2$ displayed.

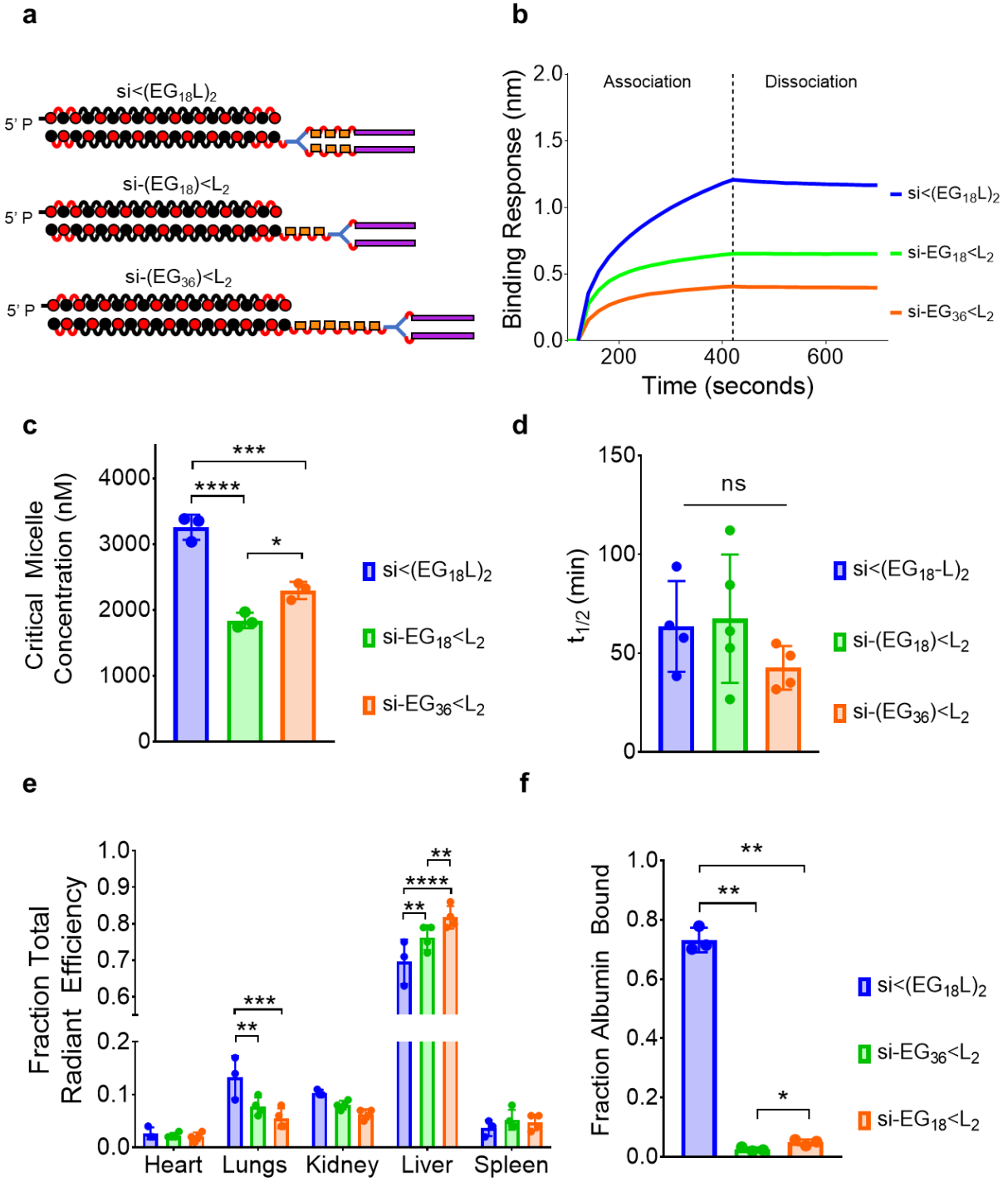

Figure 3.4: Proximal positioning of divalent lipid-siRNA conjugate branching point improves *in vitro* and *in vivo* outcomes. (A) Structures of branching position variants of lead conjugate investigated. (B) Representative *in vitro* binding responses of brancher variants to human serum albumin (400 nM) measured by biolayer interferometry. Dashed line represents transition from association to dissociation. (C) Critical micelle concentration observed after 2-hour incubation with Nile Red at 37°C (n=3). Significance assessed by 1-way ANOVA with Tukey's multiple comparisons test. (D) Absolute circulation half-life measured by intravital microscopy (n=3-4). Significance assessed by 1-way ANOVA with Tukey's multiple comparisons test. (E) Organ biodistribution of conjugate measured by IVIS approximately 45 minutes after 1 mg/kg tail vein injection. Significance assessed by 2-way ANOVA with Tukey's multiple comparisons test. (F) Fraction of albumin-bound conjugate in plasma isolated from mice approximately 45 minutes after i.v. injection (n=3). Significance assessed by 1-way ANOVA with Tukey's multiple comparisons test.

We next sought to investigate whether the nature of the C_{18} lipid itself has important implications in conjugate performance. To this end, we synthesized two variants of our lead structure- one with the carboxyl terminal still intact [si<$(EG_{18}L_{diacid})_2$] and one with a double bond [si<$(EG_{18}L_{unsaturated})_2$] by creating si<$(EG_{18}$-Amine$)_2$ and conjugating amine-reactive PFP-modified lipid variants on to the terminus of the conjugates (**Supplementary Fig. 3.2**). Both the diacid and unsaturated variants of the conjugate exhibited comparable kidney accumulation and absolute circulation half-life (**Fig. 3.5A, B**). However, si<$(EG_{18}L_{unsaturated})_2$ demonstrated significantly diminished albumin binding *in vivo* compared to its saturated and diacid counterparts (~40% bound versus ~75-80% bound) (**Fig 3.5C**). Based on the correlations of albumin-bound *in vivo* and ultimate tumor gene silencing observed previously, we therefore only proceeded with characterizing the diacid variant. Strikingly, si<$(EG_{18}L_{diacid})_2$ showed a substantially stronger binding response to albumin (**Fig. 3.5D**), with affinity for human serum albumin approximately two orders of magnitude superior to its non-acid counterpart [si<$(EG_{18}L_{diacid})_2$ KD = 0.15 ± 0.002 nM and si<$(EG_{18}L)_2$ KD = 30 ± 0.3 nM] (**Supplementary Fig. 3.4**). To determine whether the impact of this increased affinity for albumin would be captured by circulation half-life at longer time points, we additionally sampled blood from mice injected intravenously with 5 mg/kg of either

fluorescently labeled si<$(EG_{18}L)_2$ or its diacid counterpart but found no significant difference in their PK profiles (**Supplementary Fig. 3.5**).

Based on the comparable characteristics of the two variants to this point, we next compared the two in a tumor-bearing mouse model. We further decreased the dose compared to our previous screenings in an attempt to emphasize any differences between the variants (**Fig. 3.5E)**. Conjugate targeting luciferase was administered intravenously every other day for a total of three injections of 1.5 mg/kg, with a non-functional, fluorescently labeled conjugate delivered at a dose of 1 mg/kg 18h prior to sacrifice. Tumor accumulation measured by epifluorescence and flow cytometry of cells demonstrated comparable accumulation of both versions of the conjugate (**Fig. 3.5F, G)**. However, the diacid conjugate demonstrated significantly higher renal accumulation and lower liver accumulation. Despite the significant increase in albumin affinity of this conjugate, it did not produce significantly better reduction of luciferase activity. Indeed, si<$(EG_{18}L)_2$, trends toward having significantly more knockdown than its diacid counterpart **(Fig. 3.5H)**. Based on these data, we posit that hydrophobicity of the conjugate outcompetes affinity for effective *in vivo* silencing.

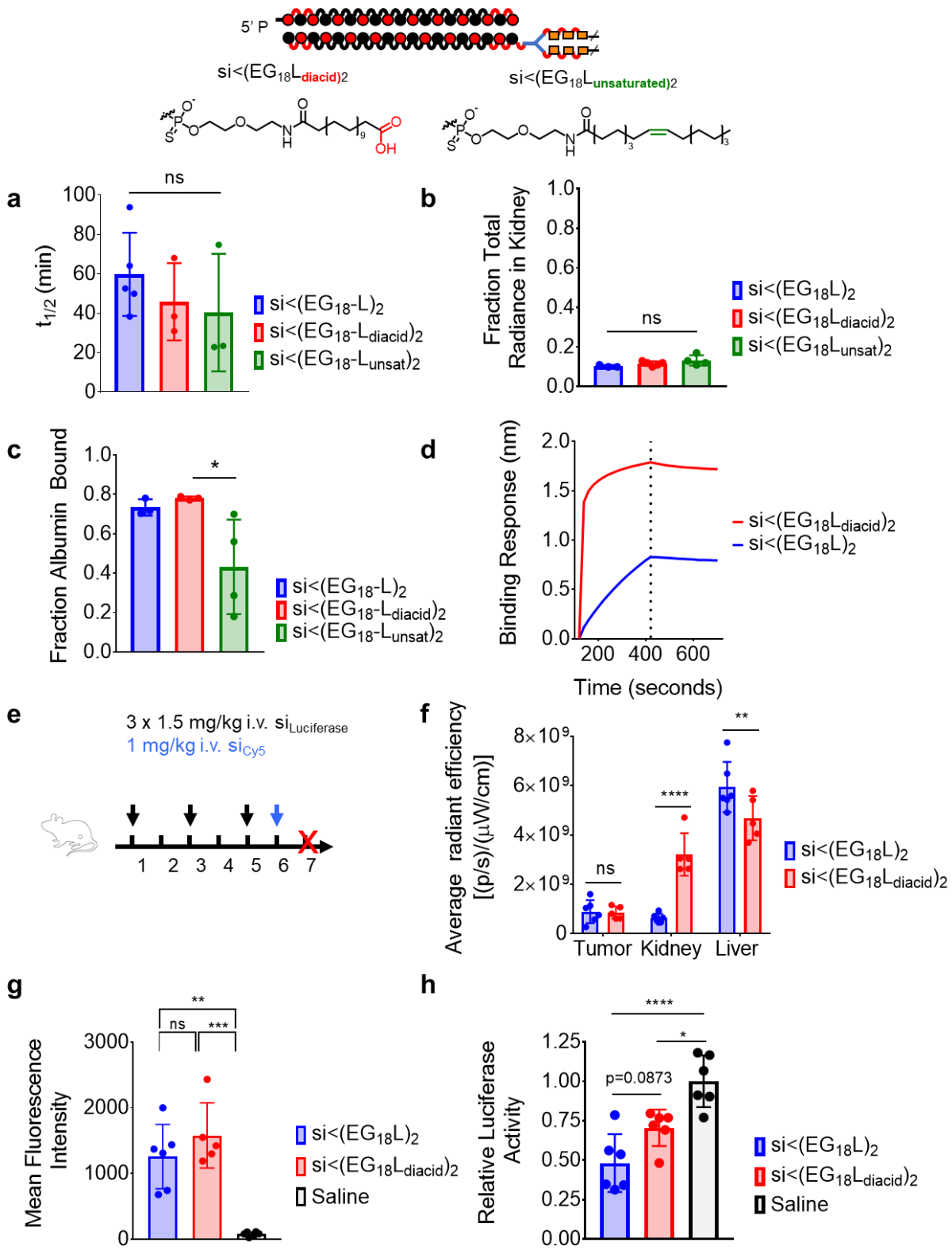

Figure 3.5: Lipid hydrophobicity is more important than carboxyl-driven albumin-binding or unsaturation for tumor gene silencing of siRNA conjugates.(A) Absolute circulation half-life measured by intravital microscopy (n=3-5). Significance assessed by 1-way ANOVA with Tukey's

multiple comparisons test. (B) Kidney biodistribution of fluorescently labeled conjugates approximately 45 minutes after 1 mg/kg intravenous injection (n=3-4). Significance assessed with 1-way ANOVA with Tukey's multiple comparison's test. (C) Fraction of albumin-bound conjugate in plasma isolated from mice approximately 45 minutes after i.v. injection (n=3-4). Significance assessed by 1-way ANOVA with Tukey's multiple comparisons test. (D) Representative *in vitro* binding responses of variants to human serum albumin (400 nM) measured by biolayer interferometry. Dashed line represents transition from association to dissociation. (E) siRNA dosing regime in mice bearing orthotopic, luciferase-expressing MDA-MB-231 tumors (F) Epifluorescence of organs measured by IVIS approximately 18h after injection with fluorescently labeled siRNA constructs. Significance assessed by 2-way ANOVA (n=5-6). (G) Average fluorescent intensity of tumor cells from each mouse measured by flow cytometry (n=5-6). Significance assessed by 1-way ANOVA with Tukey's multiple comparisons test. (H) Luciferase activity of tumors normalized to saline treated controls measured *ex vivo* after 3 x 1.5 mg/kg injections via tail vein administration (n=6). Significance was assessed by 1-way ANOVA with Tukey's multiple comparison's test.

To further interrogate the appeal of an albumin-binding, lipophilic conjugate, we synthesized an siRNA duplex directly, covalently bound to mouse serum albumin. We sought to determine whether lipid-mediated, reversible binding was preferable to maximized albumin-bound delivery (**Fig. 3.6A**). We synthesized these complexes by leveraging the two free thiol groups present on mouse serum albumin as a handle for modifying with an azido-PEG_3-maleimide linker followed by reacting with DBCO-modified siRNA duplex. Gel electrophoresis demonstrated an upward shift of resulting product relative to the DBCO-duplex precursor, suggesting successful conjugation and removal of unreacted ligands (**Fig. 3.6B**). Fluorophore-labeled duplex was additionally used to validate that A260 readouts of product agreed with fluorescent readouts for quantification of siRNA in the resulting complex. Plasma isolated from mice injected with the siRNA-MSA complex demonstrated that approximately 80% of the siRNA was associated with fractions associated with albumin (**Fig. 3.6C**). Strikingly, however, the observed half-life of the siRNA covalently bound to albumin was greatly diminished compared to our lipophilic siRNA conjugate (**Fig. 3.6D**). Previous reports have shown that cell surface glycoproteins gp18 and gp30 can bind to covalently modified albumin and act as scavenger receptors that traffic the modified

albumin for lysosomal degradation[99-101].This is further supported by the organ biodistribution of the siRNA taken from the same cohort of mice, which shows no significant difference in kidney levels between the groups (**Fig. 3.6E**). This suggests that liberation from the albumin resulting in renal clearance is not responsible for the reduction in circulation half-life. We sought to compare the *in vivo* efficacy of the two using a rigorous, low dose treatment regime to emphasize differences in performance between the two candidates (**Fig. 3.6F**). Mice bearing luciferase-expressing MDA-MB-231 tumors were treated intravenously every other day with 1.5 mg/kg siRNA for a total of three injections. A fluorescently labeled, inactive version of each compound was administered at a dose of 1 mg/kg 18h before sacrifice. Interestingly, epifluorescence of whole organs and flow cytometry of tumor cells demonstrates comparable tumor accumulation of the two compounds (**Fig. 3.6G, H**). However, the conjugate demonstrates significantly better reduction of luciferase activity than its covalently bound counterpart (**Fig. 3.6I**). These findings suggest that non-covalent binding to albumin is preferable and, further, that the lipids on the conjugate may be critical to escaping endosomal entrapment after uptake

by tumor cells.

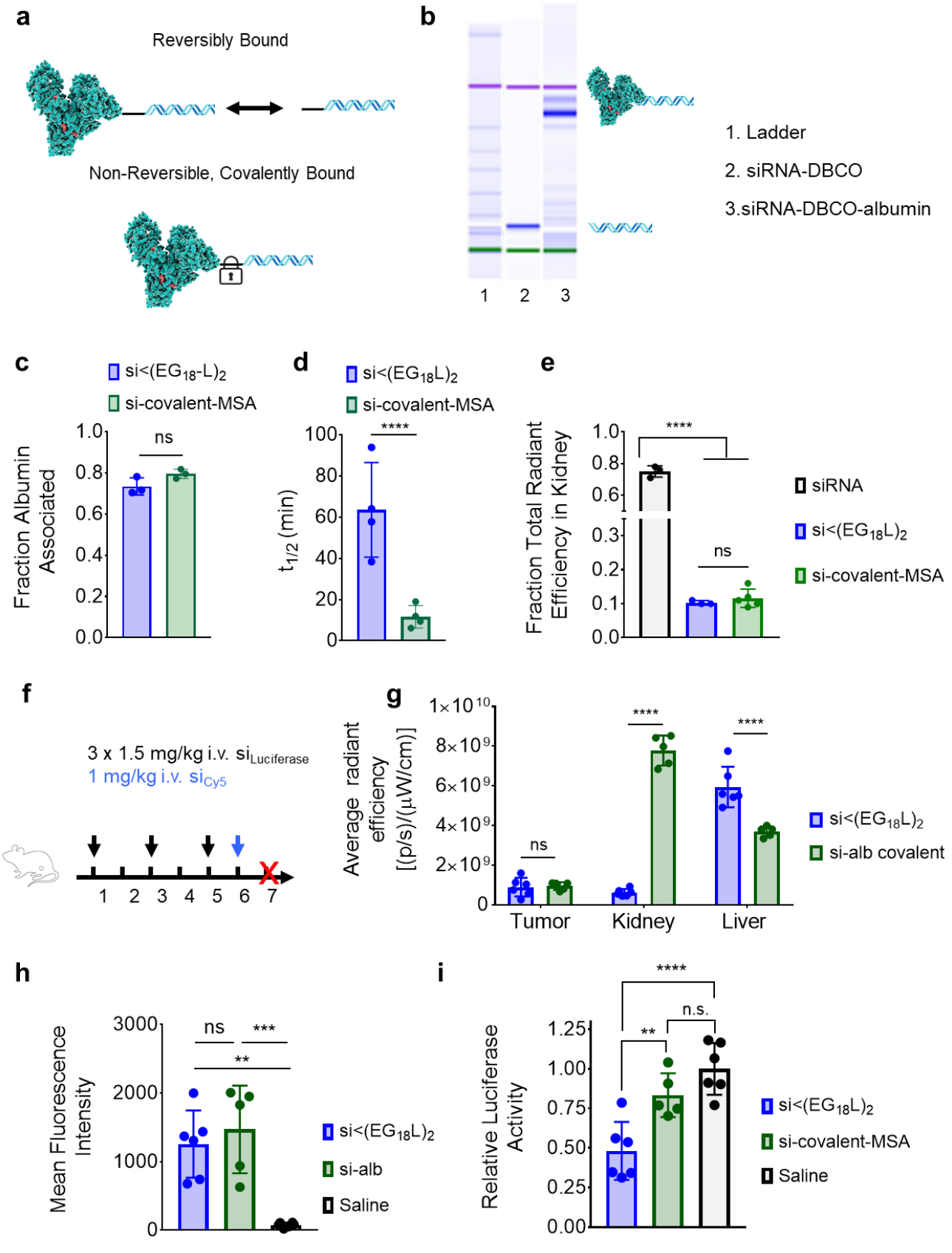
a
Reversibly Bound
Non-Reversible, Covalently Bound
b
1. Ladder
2. siRNA-DBCO
3.siRNA-DBCO-albumin
1 2 3
c
si<(EG18-L)2
si-covalent-MSA
Fraction Albumin Associated
ns
d
si<(EG18L)2
si-covalent-MSA
t1/2 (min)
****
e
Fraction Total Radiant Efficiency in Kidney
****
ns
siRNA
si<(EG18L)2
si-covalent-MSA
f
3 x 1.5 mg/kg i.v. siLuciferase
1 mg/kg i.v. siCy5
1 2 3 4 5 6 7
g
Average radiant efficiency [(p/s)/(μW/cm)]
ns
****
****
Tumor
Kidney
Liver
si<(EG18L)2
si-alb covalent
h
Mean Fluorescence Intensity
ns
***
**
si<(EG18L)2
si-alb
Saline
i
Relative Luciferase Activity
****
n.s.
**
si<(EG18L)2
si-covalent-MSA
Saline

Figure 3.6: Reversibly bound siRNA conjugate outperforms siRNA duplex covalently bound to albumin.(A) Schematic depicting the design rationale of covalently bound siRNA duplex for comparison to reversibly bound siRNA conjugate (B) Electrophoretic gel depicting the upward shift of the siRNA duplex band after conjugation to albumin (C) Fraction of albumin-bound conjugate in plasma isolated from mice approximately 45 minutes after i.v. injection (n=3-4). Significance assessed by 1-way ANOVA with Tukey's multiple comparisons test. (D) Absolute circulation half-life measured by intravital microscopy (n=3-5). Significance assessed by 1-way ANOVA with Tukey's multiple comparisons test. (E) Kidney biodistribution of fluorescently labeled conjugates approximately 45 minutes after 1 mg/kg intravenous injection (n=3-4). Significance assessed with 1-way ANOVA with Tukey's multiple comparison's test. (F) siRNA dosing regime in mice bearing orthotopic, luciferase-expressing MDA-MB-231 tumors (G) Epifluorescence of organs measured by IVIS approximately 18h after injection with fluorescently labeled siRNA constructs. Significance assessed by 2-way ANOVA (n=5-6). (H) Average fluorescent intensity of tumor cells from each mouse measured by flow cytometry (n=5-6). Significance assessed by 1-way ANOVA with Tukey's multiple comparisons test. (I) Luciferase activity of tumors normalized to saline treated controls measured ex vivo after 3 x 1.5 mg/kg injections via tail vein administration (n=6). Significance was assessed by 1-way ANOVA with Tukey's multiple comparison's test.

3.3 Conclusion

In sum, the interrogation of structure-function relationships within our lead albumin-binding siRNA conjugates led to the identification of key design features. The first observation made from these studies was that inclusion of phosphorothioate bonds, rather than phosphodiester bonds, is critical at the albumin-binding siRNA terminus and in the albumin binding moiety itself. Moreover, our studies on cleavable variants and variants lacking a lipid tail demonstrate their necessity for achieving tumor gene silencing. Next, we demonstrate, that when our lead conjugate is matched for overall ethylene glycol content, or the linker length between the siRNA and lipids, lipid constraint results in significantly diminished albumin binding. We additionally examined the implications of substituting the C_{18} lipids in our structure with their carboxyl-intact and unsaturated counterparts. We observed that, despite the striking increase in affinity conferred by the "diacid" lipids, the more hydrophobic C_{18} lipid shows superior *in vivo* performance. We speculate that this may be due to hydrophobe-driven cell insertion into membranes that drives efficacy. Finally, we show that our non-covalently albumin-binding siRNA

conjugate outperforms siRNA covalently bound to MSA. We posit this may be due to the removal of conformationally modified albumin from circulation, or once more, the need for hydrophobe driven cell membrane interactions. Taken together, these studies help elucidate the mechanism of action of our siRNA conjugate and confirm that our lead candidate would not improve from further iterative design on the aforementioned structural features.

3.4 Materials and Methods

Reagent sourcing, conjugate synthesis, purification, and mass spectrometry methods are described in Chapter 2.4. Characterization of critical micelle concentration, pharmacokinetics by intravital microscopy, proteins bound *in vivo* by size exclusion chromatography, biodistribution, *in vivo* tumor generation, *in vivo* tumor gene silencing, and affinity for albumin as measured by biolayer interferometry were all performed using the same methodology reported in Chapter 2.4.

Synthesis of Amine-Reactive Lipids

Oleic acid was dissolved at 1mM in anhydrous dichloromethane and placed on ice. A 10x molar excess of triethylamine was then added followed by a 3x molar excess of pentafluorophenyl trifluoroacetate. Octadecanoic acid was dissolved at 0.5 mM in anhydrous dichloromethane and placed on ice. A 2x molar excess of triethylamine was then added followed by a 0.5x molar excess of pentafluorophenyl trifluoroacetate added dropwise.

For both lipids, the reaction vessel was removed from ice after 15 minutes and allowed to equilibrate to room temperature. The reaction mixture was then stirred for 4h followed by storage at -20°C. The crude product was purified by silica gel column chromatography and eluted with solvents

with a gradient from 100% hexane to 100% ethyl acetate. The compounds were then rotovapped to dryness and characterized by H and F NMR.

Synthesis of Lipid-Variant siRNA Conjugates

Amine-terminated oligonucleotides were speed vacuumed to dryness and desalted to remove MMT groups. Oligonucleotides were then lyophilized followed by reconstitution in 0.1 sodium tetraborate (pH 8.5) to a concentration of 500 uM. PFP-modified lipid was dissolved into a mixture of acetonitrile, DMSO, and triethylamine (70:29:1 by volume) at a concentration of 7 uM. Aqueous oligonucleotide was added dropwise to the organic solution for a 1:40 molar ratio of oligonucleotide-amine:amine-reactive lipid (approximately 25% 0.1M sodium tetraborate, 75% organic mixture). Solution was stirred overnight and desalted prior to purification and characterization detailed in the main methods section.

Synthesis of siRNA Conjugate Variant Covalently Bound to Albumin

Conjugate covalently bound to albumin was synthesized by first reacting azido-PEG_3-maleimide (Click Chemistry Tools) with the free thiols on human (1 free SH) or mouse (2 free SH) albumin. Albumin was dissolved in PBS with 0.5M EDTA to a final concentration of 10 mM. Anhydrous DMF was used to solubilize and activate azido-PEG_3-maleimide. DBCO-modified siRNA duplex in PBS was reacted at a 1:1 ratio of DBCO groups:free SH groups and allowed to incubate at room temperature for 4 hours. To remove any siRNA that did not react with albumin, or reacted only with the azido linker, the resulting solution underwent 10 rounds of centrifugation in a 30 kDa cutoff Amicon filter at 14,000 xg

for 10 minutes for each round. Conjugation was confirmed by gel electrophoresis of precusor DBCO-siRNA alongside resulting siRNA-DBCO-albumin.

In Vivo Tumor Cell Uptake

Minced tumor was washed with HBSS containing Ca^{2+} and Mg^{2+} and then agitated for 1h in an enzyme mix containing collagenase (0.5 mg/mL, Roche Life Sciences) and DNase (0.19 mg/mL, BioRAD) in DMEM. Tumors were centrifuged and resuspended in HBSS without Ca^{2+} and Mg^{2+} and then incubated with 5 mM EDTA for 20 min. Tumors were then centrifuged, and the pellets were resuspended in HBSS with Ca^{2+} and Mg^{2+} and filtered using a 70 μm Nylon cell strainer. Filtrate was then washed once more with HBSS containing Ca^{2+} and Mg^{2+} and then incubated in ACK lysis buffer (Thermo Fisher Scientific) for 2 min before being diluted in 20 mL of $PBS^{-/-}$. Cells were then pelleted and resuspended in 1–2 mL $PBS^{-/-}$ prior to running on a flow cytometer (Guava easyCyte). Uptake analysis was performed in FlowJo. Cell populations were isolated using forward and side scatter, then GFP positive tumor cells were gated, and Cy5 fluorescence intensity was measured for the GFP positive tumor cell population.

Chapter 4: Therapeutic Mcl-1 Targeting Using Albumin-Binding siRNA Conjugates in Triple Negative Breast Cancer

4.1 Introduction

Triple negative breast cancer is a molecular subtype of breast cancer that is characterized by a lack of expression of estrogen receptor, progesterone receptor, and human epidermal growth factor receptor type 2 (HER2)[102]. As a result, these patients cannot be treated with endocrine therapy or

therapies targeted to HER2. Chemotherapy is currently the standard of care, but TNBC patients as a group have a worse outcome after chemotherapy than patients with other breast cancer subtypes[103, 104]. Neoadjuvant chemotherapy, in which chemotherapy is administered prior to surgical removal of the tumor, can be effective in the minority of women who have a complete pathological response. However, the outcome for the majority of patients who have residual disease is relatively poor[103].

Analysis of 89 surgically resected TNBCs resistant to neoadjuvant chemotherapy showed that the second most common genetic alteration was *MCL1* amplification (55%, second to *MYC*)[49]. Mcl-1 is an antiapoptotic protein that is part of the Bcl-2 family of proteins. Upregulation of these anti-apoptotic Bcl-2 family proteins has been shown to increase tumor cell survival and chemotherapy resistance[39,105]. Mcl-1 is the most frequently altered Bcl-2 family protein in TNBC[37, 40-43]. Moreover, Mcl-1 has proven clinical ties to tumor survival, drug resistance, and poor prognosis[41, 46-48]. Thus, Mcl-1 targeting is a promising approach for creating a molecularly targeted therapeutic for TNBC.

Direct Mcl-1 inhibition with small molecules is being explored in preclinical cancer models and in some clinical studies of hematological malignancies. One of those most promising compounds, S63845 (now optimized to molecule MIK665), achieved single agent in xenograft hematological cancer models. This compound and others described in the patent literature inhibit human Mcl-1 at picomolar binding affinities to trigger apoptosis, but utility of these compounds is limited in part by poor aqueous solubility, high clearance, low tumor exposure, and short half-life. In studies with humanized Mcl-1 mice, S63845 demonstrated a narrow therapeutic window, with a maximum tolerated dose of 12.5 mg/kg[62]. Small molecules are known to passively penetrate many organs, contributing to dose limiting thrombocytopenia and neurotoxicity (seen with several Bcl-2 family inhibitors)[106, 107], or hemolysis seen with S63845[56]. Moreover, small molecule inhibitors like S63845 leave Mcl-1 protein expression intact, with two critical consequences: (1) compensatory Mcl-1 protein upregulation[56, 108], which can

overwhelm the narrow therapeutic window of current Mcl-1 inhibitors; (2) Small molecule docking to the BH3-domain binding pocket leaves other Mcl-1 activities intact, including metabolic mitochondrial activities in cancer stem cells[54, 55].

An RNAi-based approach will inhibit all Mcl-1 functions, not just at the BH3 binding pocket and will prevent compensatory Mcl-1 protein upregulation. Additionally, the less promiscuous nature of siRNA can be anticipated to result in fewer toxicities than those resulting from treatment with small molecules. We therefore seek to compare our siRNA conjugate platform targeted against Mcl-1 with these clinically relevant Mcl-1 targeting small molecules for its ability to achieve therapeutic efficacy without associated morbidities.

Recent breakthroughs in the field have uncovered that pharmacological inhibition of Mcl-1 synergizes with epidermal growth factor (EGFR) inhibition in a panel of genetically diverse TNBC cells[109]. Previously, despite the observed relationship between EGFR activity and TNBC growth, drugs that inhibited EGFR signaling were consistently inefficacious in this setting[110]. Erlotinib is an orally administered EGFR inhibitor that is often used to treat non-small cell lung cancer. We therefore additionally sought to determine if we could use our platform to "unlock" the potential of EGFR inhibitors to be used treatments for TNBC.

4.2 Results and Discussion

We first sought to achieve proof-of-concept that siRNA targeting of Mcl-1 could result in reduction of tumor burden in TNBC. To this end, we used our "first generation" siRNA conjugate targeting human Mcl-1 in HCC1187 tumor bearing mice. Mice were treated intravenously 3 times per week with 2.5 mg/kg siRNA. After the first week of treatment, mice treated with Mcl-1 targeting

conjugate demonstrated a significant reduction in tumor burden compared to mice treated with a control conjugate (**Fig. 4.1A**). Additionally, mice that received the conjugate targeting Mcl-1 demonstrated significantly less tumor MCL-1 protein than saline and control conjugate-treated animals (**Fig. 4.2B-C**). MCL-1 is a member of the BCL-2 family of antiapoptotic proteins. Thus, successful silencing of Mcl-1 should induce apoptosis in the tumors, which can be measured by detecting caspase-3/7, proteases which are activated universally during apoptosis[111]. Indeed, we observed significantly more staining for caspase-3/7 in tumors harvested from mice treated with siRNA conjugate targeting Mcl-1 compared to control conjugate (**Fig. 4.1D-E)**. P-histone H3 is a protein phosphorylated during mitosis and meiosis that can be used as a proxy for cellular proliferation[112]. Successful treatment of tumors should therefore result in decreased P-histone H3 staining. We observed that $si_{Mcl\text{-}1}$ conjugate-treated tumors demonstrated significant reduction in P-Histone 3 staining compared to saline-treated controls (**Fig. 4.1F)**, indicating that MCL-1 reduction *via* RNAi can successfully impede tumor cell proliferation.

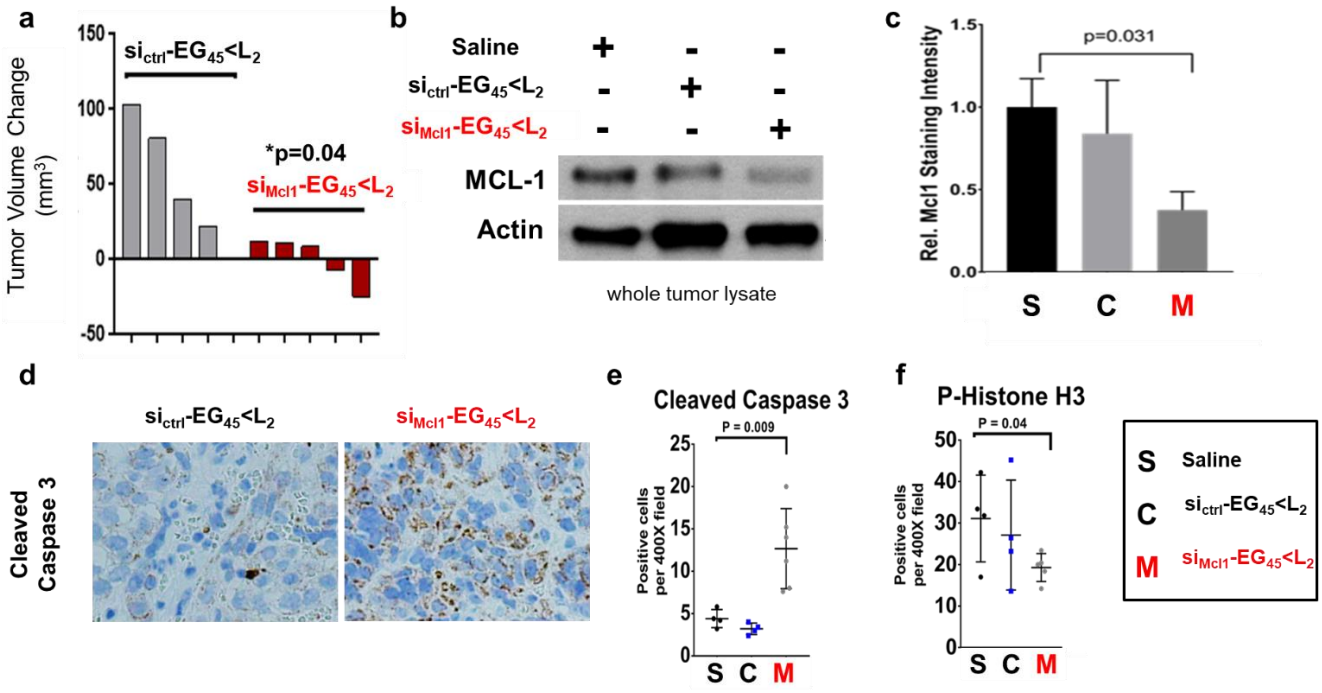

Figure 4.1: "First-generation" siRNA Mcl-1 conjugate demonstrates therapeutic efficacy in HCC1187 TNBC mouse model.
(A) Change in tumor volume from d0 to d7 of treatment regime (B) Western blot protein analysis of tumors harvested at d14 with (C) staining quantitated relative to actin control (D) Immunohistochemical staining of cleaved caspase 3 in tumor samples harvested at day 14 (E) Cleaved caspase 3 and (F) P-histone 3 staining quantification from tumors harvested at d14. (n=4-5)

We then sought to employ our optimized conjugate, which, as described in Chapter 2, shows superior silencing to our "first generation" design. We began by characterizing the ability of this optimized construct to achieve therapeutic efficacy *in vitro* alongside clinically relevant Mcl-1 inhibitor MIK665. In particular, we examined synergistic cell death induced by treatment in combination with EGFR inhibitor afatinib. Previous reports indicate that EGFR inhibition is ineffective as a single agent.

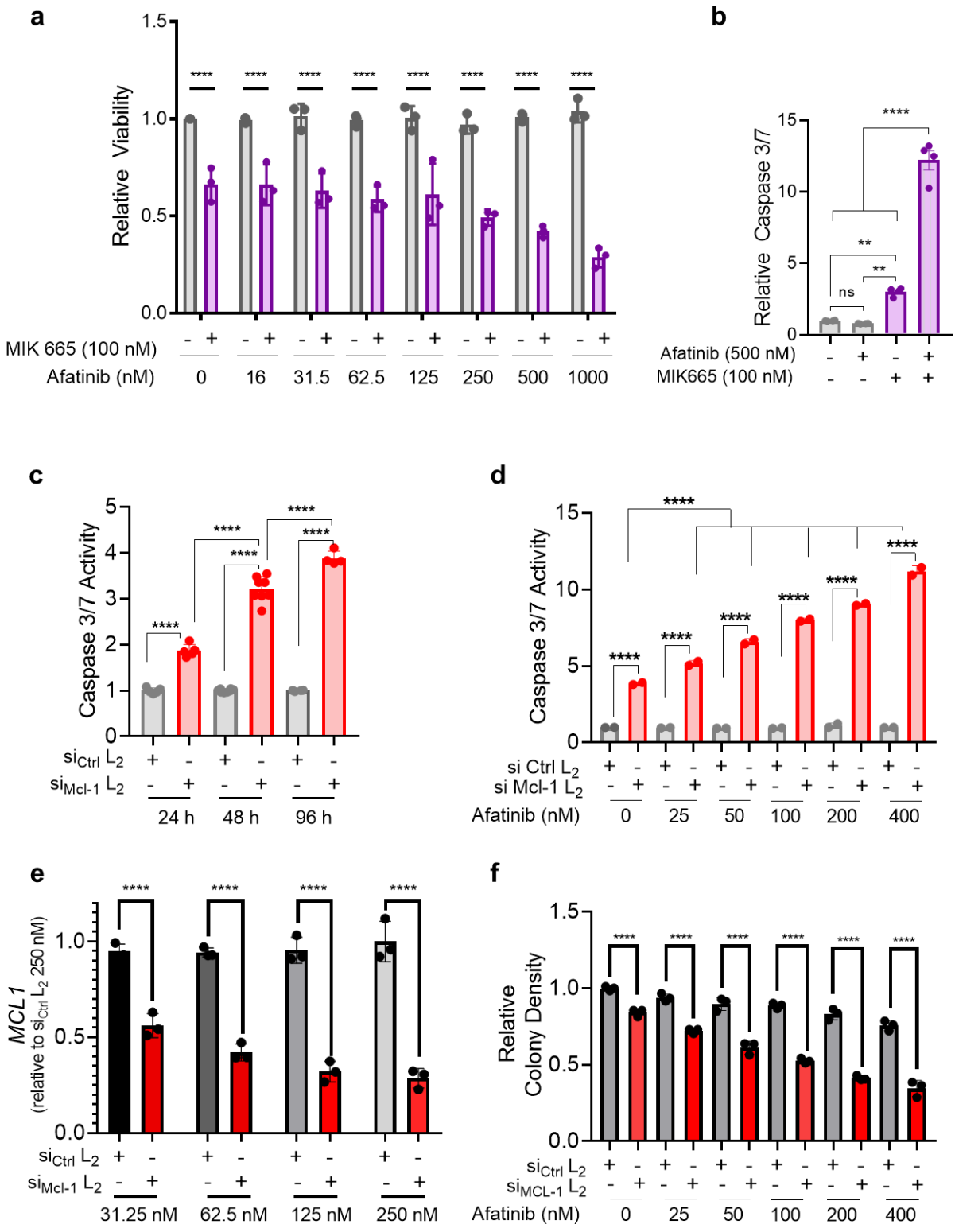

Figure 4.2: Mcl-1 targeting siRNA conjugate induces cell death *via* apoptosis and synergizes with EGFR inhibition comparably to small molecule drug MIK665

(A) Viability of HCC70 TNBC cells treated with small molecule inhibitor of MCL-1, MIK665, with or without EGFR inhibitor afatinib. Caspase 3/7 activity of HCC70 cells treated with (B) MIK665 +/- afatinib (C) 31 nM siRNA conjugate as a single agent or (D) siRNA conjugate +/- afatinib. (E) Mcl-1 mRNA levels in HCC70 cells treated for 24 h with siRNA conjugate (F) Cell viability of HCC70s treated for 96 h with siRNA conjugate +/- afatinib. Significance assessed by 2-way ANOVA with Tukey's multiple comparisons test (n=3).

However, oncogene "addiction" to Mcl-1 has been identified as a key component in this phenomenon. Indeed, we observed that single agent treatment of TNBC cell line HCC70s with afatinib did not result in significant tumor cell death, but introduction of Mcl-1 small molecule inhibitor achieved a synergistic effect (**Fig. 4.2A, Supplementary Fig. 4.1).** This synergy is even more evident when apoptosis is assessed *via* levels of cleaved caspase 3/7 (**Figure 4.2B**). Apoptosis achieved by combined treatment is significantly greater than the combined individual effects of the two treatments. We then sought to establish if we could induce comparable apoptosis and synergy using our siRNA conjugate targeting Mcl-1 in lieu of small molecule treatment. As a single agent at the carrier-free dose of 31.5 nM, apoptosis of HCC70 TNBC cells increased significantly over a time course of 96 h (**Fig. 4.2C**). Further, we demonstrate that our Mcl-1 targeting siRNA conjugate achieves synergy in combination with EGFR inhibitor afatinib at relatively low doses when compared to a control siRNA conjugate (**Fig. 4.2D**). Moreover, we confirm the dose-dependent reduction of Mcl-1 mRNA from *in vitro* treatment with our conjugate compared to a non-targeting control (**Fig. 4.2E**), and that we can achieve dose-dependent reduction of HCC70 TNBC viability (**Fig. 4.2F, Supplementary Fig. 4.2**).

Major toxicities associated with small molecule inhibition of Mcl-1 have limited its clinical translation. For instance, Amgen recently put their clinical studies on one such inhibitor on hold due to cardiotoxicity[51]. Servier pharmaceuticals MCL-1 inhibitor S63845 demonstrates a maximum tolerated dose in humanized MCL-1 mice of 12.5 mg/kg (S63845 has an approximately six-fold higher affinity

for the human compared with the mouse MCL-1 protein)[62]. MCL-1 is important for hematopoietic stem cells[59], and the most significant toxicities induced by the drug are depletion of B-cells in the spleen and bone marrow as well as erythrocyte depletion, hemolysis, and weight loss[113]. We therefore sought to explore the toxicities induced by treatment with our siRNA construct targeting Mcl-1 for comparison. Our data reported in Chapter 2 demonstrate that a bolus of 20 mg/kg can achieve approximately 85% silencing of tumor MCL-1 at 8 days after a single intravenous injection. We therefore sought to characterize the acute toxicities induced by this dose by utilizing an siRNA that targets both mouse and human Mcl-1. As a direct comparison, 12.5 mg/kg of S63845 caused acute toxicities at after two consecutive daily treatments of 12.5 mg/kg. Three days post treatment, we isolated examined blood chemistry markers of toxicity, CBC, and B cells from the bone marrow and spleen of treated and

untreated animals.

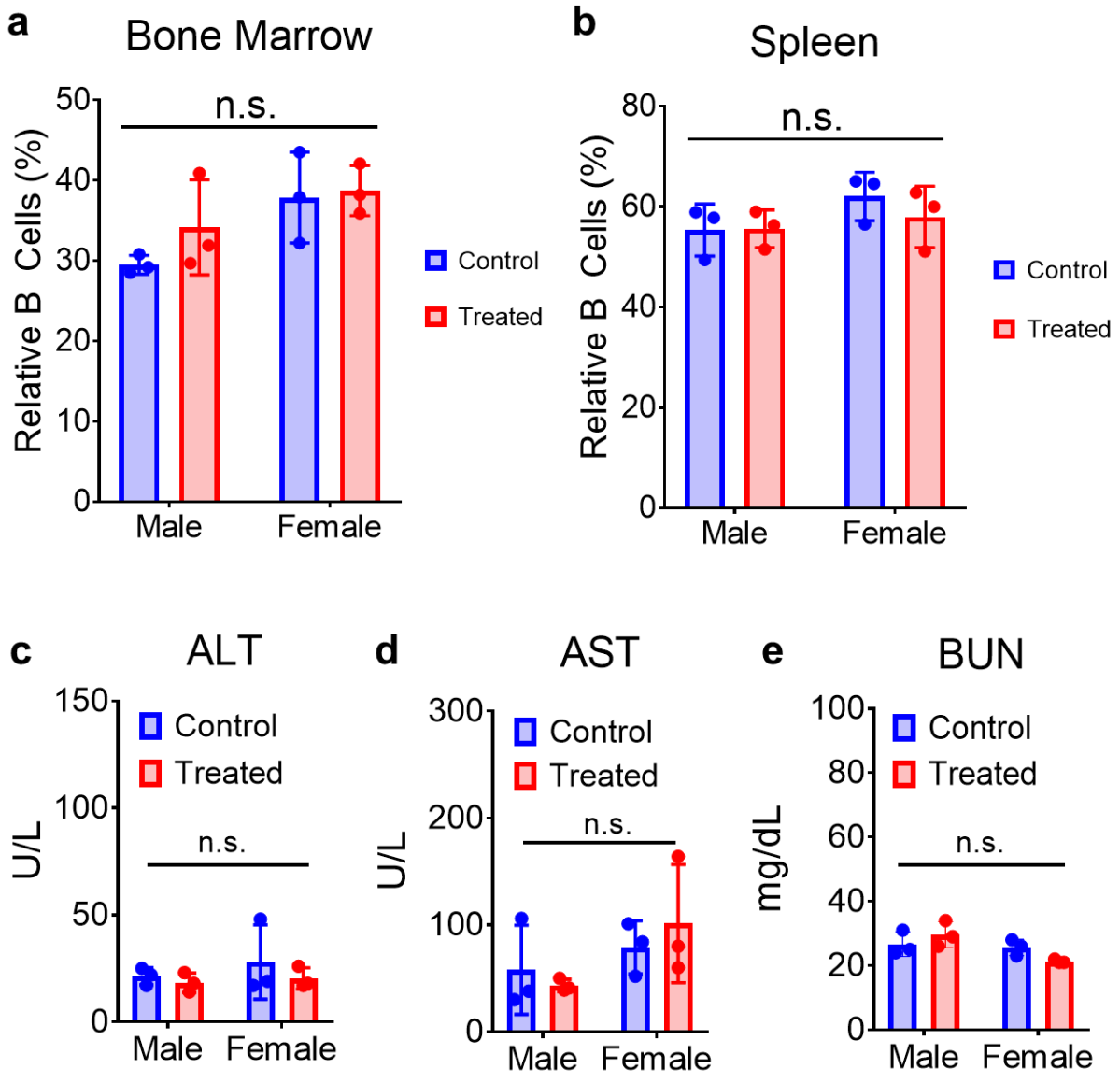

Figure 4.3: siRNA conjugate targeting Mcl-1 avoids acute toxicities associated with small molecule inhibition.

B cells relative to total viable cells isolated from (A) bone marrow and (B) spleen isolated from wild type mice three days after injection with 20 mg/kg siRNA conjugate targeting Mcl-1 compared to untreated controls. Levels of blood chemistry markers (C) alanine aminotransferase (D) aspartate aminotransferase and (E) blood urea nitrogen from sera of treated and untreated mice. Significance assessed by 2-way ANOVA with Tukey's multiple comparisons test (n=3).

Promisingly, there was no significant difference in the viable B cells between treated and untreated mice across both sexes (**Fig. 4.3A-B**). Additionally, the animals did not show any significant changes in blood urea nitrogen (BUN), creatinine, aspartate-aminotransferase (AST), or alanine-aminotransferase (ALT), which can give insight into kidney, heart, and liver-associated toxicities (**Fig. 4.3C-E)**. We further examined indicators of hemolysis, a toxicity noted with small molecule inhibition of MCL-1. Notably, no significant differences in hematocrit, hemoglobin, or red blood cell content were observed (**Supplementary Fig. 4.4**), suggesting that RNAi targeting of Mcl-1 with our construct avoids this manifestation of toxicity.

We then investigated the ability of our construct to achieve a reduction in tumor burden *in vivo* compared to small molecule inhibition. Mice bearing HCC70 TNBC tumors were enrolled into treatment groups after reaching a tumor volume exceeding 50 mm^3. Mice were then treated once weekly with intravenous siRNA conjugate (10 mg/kg) or Mcl-1 small molecule inhibitor MIK 665 (12.5 mg/kg). Starting at day 21, we were able to achieve significantly improved reduction in tumor burden over control conjugate, MIK 665, and MIK 665 vehicle-treated mice (**Fig. 4.4A**). Indeed, at the conclusion of the 28-day treatment regiment, MIK 665 did not demonstrate significantly different tumor growth compared to its vehicle control, whereas treatment with $si_{Mcl\text{-}1}$ conjugate did (**Fig. 4.4B**). On a molar scale, MIK 665 was administered in >18x the amount of siRNA conjugate, underscoring the superior therapeutic window of our platform. Our studies in combination with EGFR inhibitor erlotinib show that MIK 665 is only able to achieve tumor burden reduction when administered as a combination therapy (**Supplementary Fig. 4.5**), whereas siRNA conjugate targeting Mcl-1 is effective as a single agent and for unlocking the therapeutic potential of EGFR inhibitors for use in TNBC.

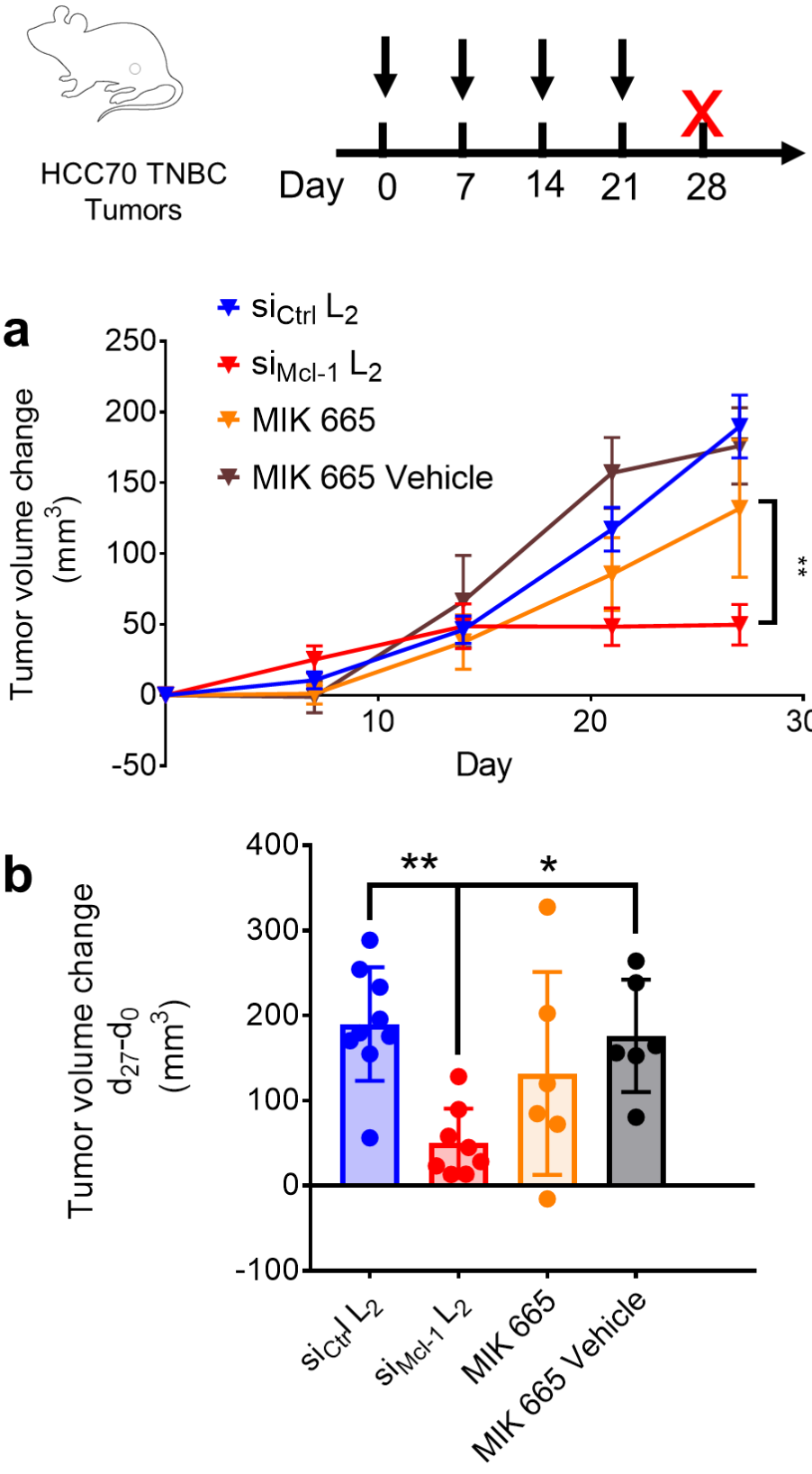
HCC70 TNBC
Tumors
Day 0 7 14 21 28
X
a
siCtrl L2
siMcl-1 L2
MIK 665
MIK 665 Vehicle
Tumor volume change
(mm3)
250
200
150
100
50
0
-50
10
20
30
Day
**
****
b
Tumor volume change
d27-d0
(mm3)
400
300
200
100
0
-100
**
*
siCtrl L2
siMcl-1 L2
MIK 665
MIK 665 Vehicle

Figure 4.4:Treatment with siRNA conjugate targeting Mcl-1 outperforms small molecule MIK665's ability to reduce tumor burden in a HCC70 TNBC mouse xenograft model

(A) Change in tumor volume from day 0 (measured by a blinded observer) over the course of 28 days with once weekly intravenous treatment of either 10mg/kg siRNA or 12.5 mg/kg MIK 665 (Mean +/- SEM plotted). Significance assessed by 2-way ANOVA with Tukey's multiple comparisons test (n=6-9). (B) Tumor volume change on day 28 of treatment. Significance assessed by one-way ANOVA with Tukey's multiple comparisons test (n=6-9).

4.3 Conclusion

Herein, we demonstrated the utility of our previously reported diacyl lipid-modified siRNA targeting against Mcl-1 for decreasing tumor burden in a mouse xenograft model of TNBC through the reduction of Mcl-1 protein and the resultant induction of apoptosis and impeded cell proliferation of tumor cells. This proof-of-concept then warranted in depth examination of our newly optimized siRNA conjugate that has shown significantly improved serum stability, pharmacokinetic properties, and ultimate tumor gene silencing. We show that, compared to clinically relevant Mcl-1 small molecule inhibitor MIK665, we can administer therapeutically effective doses without the induction of toxicities such as hemolysis, B-cell reduction, and erythrocyte depletion. We additionally demonstrate *in vitro* the potent cell death achieved by cotreatment with Mcl-1 targeting therapeutics and EGFR inhibition. Importantly, we show *in vivo* that MIK 665 is ineffective as a single agent treatment, whilst treatment with our Mcl-1 siRNA conjugate is effective both as a monotherapy and in combination with EGFR inhibition. These findings taken collectively showcase the exciting potential for RNAi therapeutics in lieu of traditional small molecule therapies for treating TNBC.

4.4 Materials and Methods

Reagents

PE anti-mouse CD19 Antibody (Catalog No. 115508) and PC anti-mouse/human CD45R/B220 Antibody (Catalog No. 103212) were acquired from Biolegend. Erlotinib HCl (OSI-744) and Captisol (Catalog No. S1023) were purchased from SelleckChem. MIK665 (Cat. No. HY-112218) was purchased from MedChemExpress.

In Vitro Assessment of Therapeutics

Cells were seeded at 100,000/ well in 12-well plates or 10,000/well in 96-well plates in complete media and allowed to adhere overnight. Cells were then treated with siRNA conjugate (31.25 nM) in serum free media for a total of 96 h total. Cells were fed with fresh media (10% serum) containing Afatinib (0, 25 nM, 50 nM, 100 nM, 200 nM, 400 nM) (T0 = 48h after introducing siRNA conjugate) for 48 h. Cells were then assessed for caspase activity using Caspase 3/7-Glo at 24h intervals after adding siRNA conjugate (96-well plates) or fixed and permeabilized with formalin followed by staining with trypan blue for 10 min. Fixed cells were then washed with PBS, photographed, and staining density was measured as the sum of absorbance values across a 16 x 16 grid within each well.

B Cell Flow Cytometry

Spleens were excised and immediately placed into a culture dish containing PBS without Ca^{2+} and Mg^{2+} [PBS (-/-)] + 1mM EDTA. The splenocytes were then released by crushing the spleen 5 times in gentle, circular motions. The dissociated tissue was passed through a 70 µM cell strainer followed by centrifugation at 500 x g for 8 min at 8°C.

Mouse femorae and tibiae were excised, and cells were isolated by flushing the bones using a 25G needle with 10 mL of PBS (-/-) supplemented with 5 mM EDTA plus 1% fetal calf serum. The cell

suspension was then filtered through a 70 µM strainer followed by centrifugation at 500 x g for 8 min at 8°C.

Both spleen and bone marrow cell supernatants were then discarded, and the cell pellets were resuspended in 3 mL of room temperature ACK lysis buffer by vortexing and incubating on ice for 3 min. Samples were then diluted with 10 mL of FACS buffer [PBS (-/-) containing 1% FBS and 2 mM EDTA] followed by centrifugation for 8 min at 500 x g, 8°C. Supernatant was discarded, and pellets were resuspended in FACS buffer for counting. Cells were diluted and 1 x 10^6 cells in 200 µL were added to conical tubes for 1:100 incubation with mouse Fc block for 5 min at room temperature. Antibodies and DAPI were then added at a final staining dilution of 1:200 and 1:400, respectively and allowed to incubate in the dark at 4°C for 30 min. Samples were then diluted with 2 mL of cold FACS buffers and spun and 500 x g for 8mins at 8C. Supernatant was decanted and 2 mL of cold FACS buffer was added followed by vortexing and centrifugation at 500 x g for 8 mins at 8°C. Supernatant was discarded again and 200 µL of FACS buffer was used to resuspend the samples for analysis.

Samples were run on a BD FACS Diva, and compensations and fluorescence minus ones were used to generate flow parameters. B cells were defined as high intensity staining of CD19 PE and B200 APC. Gating can be found in the **Supplementary Fig. 4.2**.

Blood Chemistry and CBC

Whole blood was collected in EDTA-coated tubes or spun down at 2,000 x g for 15 min at 4°C to isolate plasma. Samples were then submitted to the Vanderbilt Translational Pathology Shared Resource for CBC and chemistry analyses.

Tumor-Bearing Mouse Models

HCC70 cells (1 x 10^6) in 100 uL of 50% Matrigel were injected into the inguinal mammary fat pads of 4–6-week-old female athymic Balb/C (*nu/nu*) mice (Envigo). Mice were randomized into treatment groups when tumors exceeded 50 mm^3. Mice were treated once per week with either si_{MCL-1} conjugate or MIK665 with or without erlotinib and respective vehicles. Conjugates were administered intravenously at a 10 mg/kg (based on parent siRNA molecular weight) bolus in 0.9% saline. MIK665 treatments were formulated extemporaneously at 3 mg/mL in 2% vitamin E/d-α-tocopheryl polyethylene glycol 1000 succinate (Sigma-Aldrich) in NaCl 0.9% (wt/vol) and delivered by IV tail-vein injection at 12.5 mg/kg at the indicated schedule. Erlotinib or vehicle (150 mg/mL in captisol) was administered by oral gavage once weekly at a dose of 42.5 mg/kg.

Mice were euthanized and organs collected at necropsy for molecular histological analysis. Tumors were either flash frozen in liquid nitrogen for downstream assays or fixed overnight in formalin followed by storage at 4°C in 70% ethanol.

Chapter 5: Conclusion

5.1 Chapter Summaries and Impact

In the first aim of this dissertation (Chapter 2), we sought to create an siRNA construct optimized for albumin binding by first creating metabolically stable siRNAs and then by varying valency and hydrophilic linker length. Previous work in our lab demonstrated the utility of modifying siRNA with DSPE-PEG_{2000}. However, this moiety was never optimized for the delivery of highly hydrophilic siRNA, and contains hydrolytically degradable ester bonds, a polydisperse PEG linker, and

sterically constrained lipids. Additionally, the synthesis of this "first generation" siRNA conjugate involved two-step click chemistry, which results in low yield and the incorporation of a bulky dibenzocyclooctyne group. Our library of conjugates made with solid phase synthesis demonstrated excellent serum stability while maintaining potency and demonstrated the importance of ligand valency. Our findings demonstrated an optimal length of ethylene glycol linker that demonstrated superior albumin binding, circulation half-life, and ultimate tumor gene silencing.

The second central thrust of this work (Chapter 3) was interrogating structural features of importance within our lead conjugate to aid in elucidating its mechanism of action. We demonstrated the necessity of metabolic stability at the albumin-binding terminus of the construct, the barrier presented to albumin binding by lipid constraint, the advantages of noncovalent binding, and the overshadowing of albumin affinity by hydrophobe-driven interactions. These structure-function relationships help elucidate the mechanism by which the conjugate achieves its effect and inform if additional iterative designs are warranted. For instance, the significant difference in tumor gene silencing between metabolically labile and stable versions of the conjugate suggest that an intact hydrophobe is critical to penetrating cell membranes. This is further supported by the outperformance of conjugate modified with C_{18} stearate over its carboxylic acid modified counterpart, C_{18} stearic acid, which had significantly higher albumin affinity. Additionally, the comparatively poor performance of siRNA directly conjugated to albumin suggests that covalent modification may traffic albumin to degradative rather than recycling pathways or underscore that binding mediated by a hydrophobe is more important than achieving maximized binding.

The third major part of this work (Chapter 4) investigated the utility of our siRNA conjugate platform when targeted against Mcl-1 for achieving therapeutic outcomes in TNBC. We demonstrate proof-of-concept using our "first generation" conjugate, an siRNA modified with a PEG-diacyl lipid to

demonstrate that siRNA inhibition of Mcl-1 in a mouse xenograft model of TNBC results in the induction of tumor cell apoptosis and reduction of cell proliferation. We then characterized the toxicity profile of our siRNA conjugate to demonstrate the improved therapeutic window unlocked with our construct compared to small molecule inhibitors of Mcl-1. We then investigate the *in vitro* and *in vivo* potency of our conjugate with and without co-treatment with EGFR inhibitors alongside small molecule MIK 665. We demonstrate that, whereas MIK 665 requires co-treatment to achieve efficacy, our platform achieves reduction of tumor burden as a single agent therapy.

This work has broad implications for the field by shedding new light on our understanding of the structure-function relationship of lipid-modified siRNAs. Our systematic optimization and interrogation of structure has yielded a conjugate that can achieve potent tumor gene silencing without significant off-target effects. We have demonstrated promising tumor burden reduction through targeting Mcl-1, but this system is amenable to targeting a wide variety of oncogenes owing to its modular nature. Additionally, this platform further lends itself to use in other pathologies where inflammation and albumin accumulation can be leveraged to deliver siRNA payloads.

5.2 Shortcomings

Throughout this work, we utilize a synthetic, blunt ended 19-mer siRNA that is modified with alternating 2'F and 2'OMe modifications in a "zipper" pattern. However, much work has been recently done to demonstrate that an overhang on the 3' end of the antisense strand can confer superior gene silencing over a blunt ended counterpart[89]. In addition, it has been reported that more judicious utility of 2'F modifications within the siRNA duplex can dramatically increase potency *in vivo,* allowing the overall dose to achieve efficacy to be greatly reduced[114]. Finally, in this work, we use a 5' phosphate

group on the antisense strand. However, this group is susceptible to phosphatases when administered systemically. Substituting this group with a vinyl phosphonate group instead, a phosphate analog with greater metabolic stability, has been shown to improve tissue accumulation and efficacy of siRNAs after i.v. administration[115]. Thus, despite the exciting advances reported in this work, much improvement could be made to the siRNA portion of the construct.

To determine relative tissue biodistribution, we utilized a fluorophore to label our siRNA constructs that could be detected by epifluorescence and flow cytometry. Though this labeling technique was consistent across our library of candidates, drawing stand-alone conclusions about tissue accumulation of the conjugates based on this readout is dubious. Fluorophores have been demonstrated to affect cellular accumulation and gene silencing activity of hydrophobe-modified siRNAs *in vitro*[116, 117]. It was reported that Cy5.5 attached on the side of the duplex opposite of the hydrophobe increases nonproductive intracellular accumulation of the conjugate when delivered carrier-free *in vitro*. Additionally, the fluorophore used in the studies described herein was attached with a phosphodiester, a linkage which is susceptible to degradation by exonucleases. Thus, only early timepoints after systemic administration could be considered, given that the fluorophore might otherwise be liberated from the duplex. Instead, measurements that quantify intact antisense strands, such as stem-loop PCR or hybridization assays, should be used to determine absolute amounts of siRNA conjugate in tissues of interest or in the blood.

Our conjugates were delivered by intravenous injection in the *in vivo* studies detailed in this work. Though this is standard for chemotherapy, clinically relevant siRNA conjugates can be administered subcutaneously, which is far less invasive and could in theory be administered outside of a medical setting[118]. We have performed some preliminary work to explore whether our system could be administered subcutaneously with limited success compared to our intravenous route of administration.

Further optimization of the system or examination at different timepoints may be needed to achieve this more advantageous route of administration.

Finally, toxicity studies involving our construct were performed in wild-type, healthy mice. We created an siRNA construct for this purpose specifically to be able to look at "on target" toxicity in mice while treating human-derived tumors. However, ultimately it would be ideal to be able to optimize the siRNA sequence for efficacy in silencing human Mcl-1 only and not mouse. Clinically relevant Mcl-1 targeting small molecules have been shown to have much greater affinity for human Mcl-1 compared to mouse, confounding traditionally performed toxicity studies. Thus, to determine a more accurate maximum tolerated dose, humanized Mcl-1 mouse models were utilized to better characterize toxicity[62]. To determine a more accurate maximum tolerated dose, our platform should be optimized for human Mcl-1 and compared in a humanized Mcl-1 mouse model with a clinically relevant Mcl-1 inhibitor as a positive control. Additionally, we used immunodeficient mice with human tumor xenografts to examine therapeutic efficacy of our construct. Patient-derived xenografts would provide a more relevant model for examining our therapeutic as they maintain high tumor microenvironment fidelity compared to tumors created from *in vitro* cell expansion. Further, this construct would benefit from testing in a spontaneous mouse tumor model to examine treatment outcomes more closely in an immune competent mouse.

5.3 Future Work and Potential Applications

Though we have achieved exciting progress in the field with the identification of our new construct and its therapeutic effects, there are several exciting avenues for improvement and advancement with this system. First, though we hypothesize that cell membrane penetration is achieved through the use of our hydrocarbon tails, there is room for improvement by introducing a dedicated

module for endosome escape. For instance, recent reports have demonstrated that small molecules such as chloroquine can be used to induce potent endosome escape of hydrophobe-modified siRNAs[119]. Our group is currently investigating incorporating chloroquine *via* solid phase synthesis into our construct to interrogate its effect on endosome escape and ultimate gene silencing efficacy.

Currently, this design is limited to modification of the 5' end of the sense strand for albumin binding. However, additional moieties can be added to the construct through the use of an asymmetric "doubler" phosphoramidite. This allows classic solid phase synthesis to be performed on one "branch," while the other remains protected. The other "branch" can then be deprotected post-synthesis for the incorporation of additional ligands such as endosomolytic compounds or additional targeting moieties. For example, our construct currently only uses albumin-binding to traffic it to tumors. To increase specificity, additional tumor-targeting ligands such as folate could be incorporated into the construct using this synthetic approach.

While oncogene Mcl-1 is well-vetted and had a clinically relevant small molecule inhibitor to use for comparison in our studies, other oncogenes or co-targeting of multiple oncogenes may be superior to RNAi of Mcl-1 alone. Because of the modular nature of our siRNA construct, alternative targets and co-targets for TNBC and other cancers can be screened with facile synthesis. For example, analysis of 89 surgically resected TNBCs resistant to neoadjuvant chemotherapy showed Mcl-1 is the second most common genetic alteration, with oncogene c-Myc being first [49]. The transcription factor c-Myc (*MYC*) drives cell proliferation and metabolism [120-124], and is often accompanied by Mcl-1 dependent survival. Indeed, Mcl-1 regulates mitochondrial metabolism in TNBCs through cooperation with c-Myc[105]. Frequent Mcl-1/c-Myc co-amplification in TNBC clinical samples, including those resistant to neoadjuvant chemotherapy[49], and cell lines supports their inter-dependence in driving TNBC metabolism/proliferation/growth and motivates testing efficacy of c-Myc/Mcl-1 co-inhibition.

While albumin's properties confer it with tumor tropism that we have leveraged for treating TNBC, there is also great promise for using this platform to treat other pathologies characterized by inflammation and/or vascular leakiness. For example, arthritis, whether caused by age, trauma, or autoimmunity, is one such inflammatory disease for which we have already collected exciting preliminary results. Our data suggest that we can systemically administer our construct and achieve targeting of inflamed joints, and that by using an siRNA that targets matrix metalloproteinase-13 (MMP-13), a driver of inflammation and arthritis pathology, we can achieve significant rescue of the joints from the diseased phenotype. In addition, many neurodegenerative diseases are associated with increased permeability of the blood-brain-barrier (BBB) to albumin penetration[125]. The healthy BBB typically is impermeable to large molecule therapeutics, but increased transcytosis of albumin associated with onset of CNS disease may present a therapeutic gateway for delivery. Our preliminary data indicate that our systemically administered, albumin-binding construct can achieve significantly increased accumulation in the aged mouse brain compared to healthy controls. Further, this phenomenon is not achieved with systemically administered "parent" siRNA, suggesting a more specific mechanism relating to albumin. This hypothesis is further supported by the same observations performed with albumin-binding dye, Evans Blue, in aged and young mice.

Taken together, the construct optimized and tested in this work holds immense promise for not only oncology, but a myriad of diseases. Moreover, the modular nature of this therapeutic lends itself to facile screening of a range of targets within these pathologies.

Appendix A: Supplementary Material for Chapter 2

Supplementary Table 2.1: siRNA Sequence Details

	Sequence (5’ to 3’)
Luciferase (Luc) Antisense	(PHO) (OMeU)*(fU)*(OMeC) (fA) (OMeU) (fU) (OMeA) (fU) (OMeC) (fA) (OMeG) (fU) (OMeG) (fC) (OMeA) (fA) (OMeU)*(fU)*(OMeG)
Luc Sense	(fC)*(OMeA)*(fA) (OMeU) (fU) (OMeG) (fC) (OMeA) (fC) (OMeU) (fG) (OMeA) (fU) (OMeA) (fA) (OMeU) (fG)*(OMeA)*(fA)
Scrambled (Scr) Antisense	(PHO) (OMeG)*(fU)*(OMeA) (fU) (OMeU) (fA) (OMeU) (fA) (OMeC) (fG) (OMeC) (fG) (OMeA) (fU) (OMeU) (fA) (OMeA) (fC) (OMeG)*(fA)*(OMeC)
Scr Sense	(fC)*(OMeG)*(fU) (OMeU) (fA) (OMeA) (fU) (OMeC) (fG) (OMeC) (fG) (OMeU) (fA) (OMeU) (fA) (OMeA) (fU)*(OMeA)*(fC)
Cy5-labeled Luc Antisense	(Cy5) (OMeU)*(fU)*(OMeC) (fA) (OMeU) (fU) (OMeA) (fU) (OMeC) (fA) (OMeG) (fU) (OMeG) (fC) (OMeA) (fA) (OMeU)*(fU)*(OMeG)
Biotin-TEG-labeled Luc Antisense	(BTN-TEG)*(OMeU)*(fU)*(OMeC) (fA) (OMeU) (fU) (OMeA) (fU) (OMeC) (fA) (OMeG) (fU) (OMeG) (fC) (OMeA) (fA) (OMeU)*(fU)*(OMeG)
Phosphorothioate bond (X)(X)* *Phosphodiester bond (X) (X)* *2’F substituted base (fX)* *2’OMe substituted base (OMeX)*	

Supplementary Figure 2.1: LC-MS characterization of siRNA and siRNA conjugates

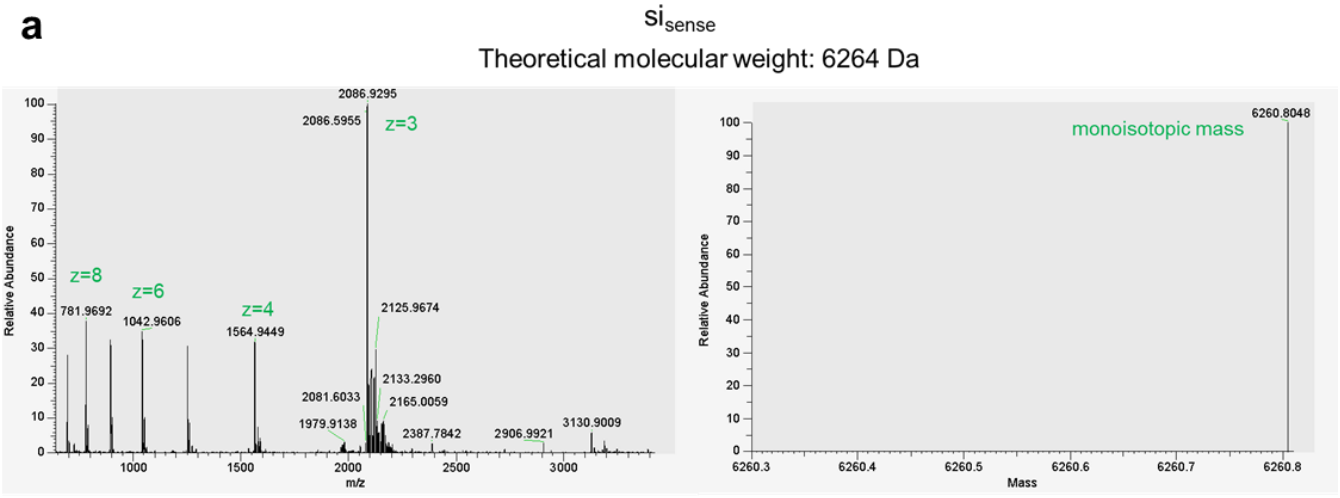

$si_{antisense}$-TEG-Biotin

Theoretical molecular weight: 6920 Da

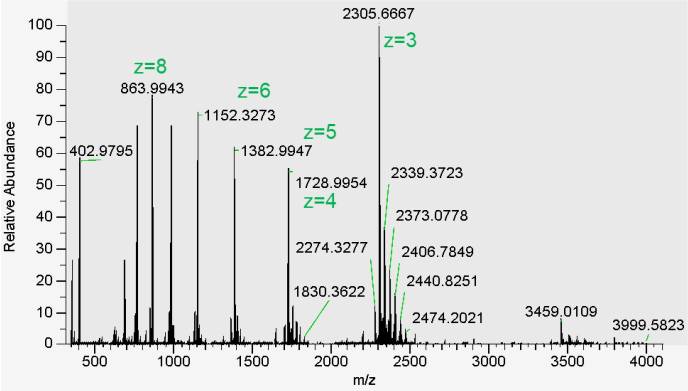

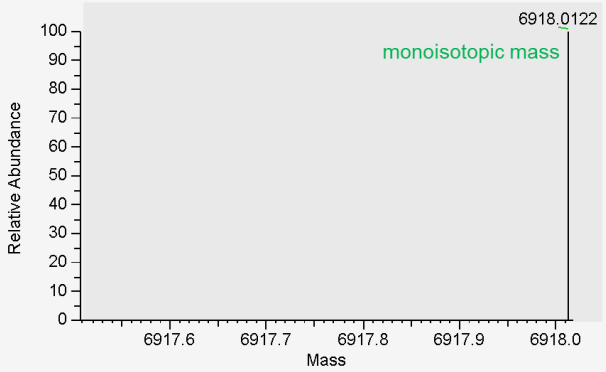

$si_{antisense}$-Cyanine 5

Theoretical molecular weight: 6740 Da

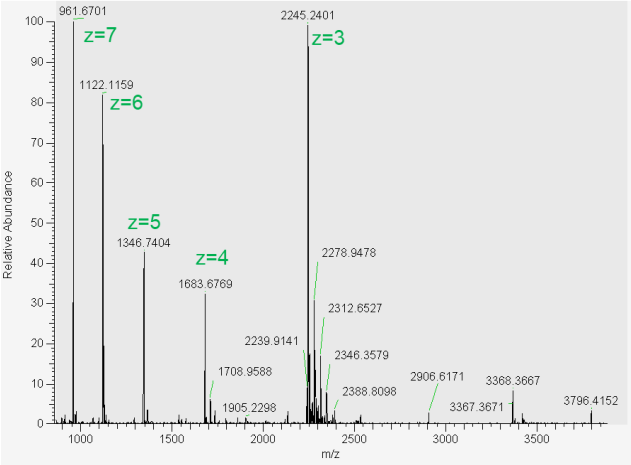

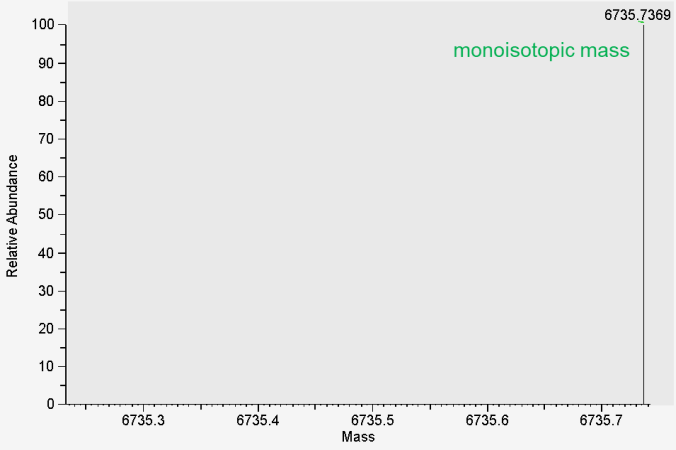

si-L_1

Theoretical molecular weight: 6612 Da

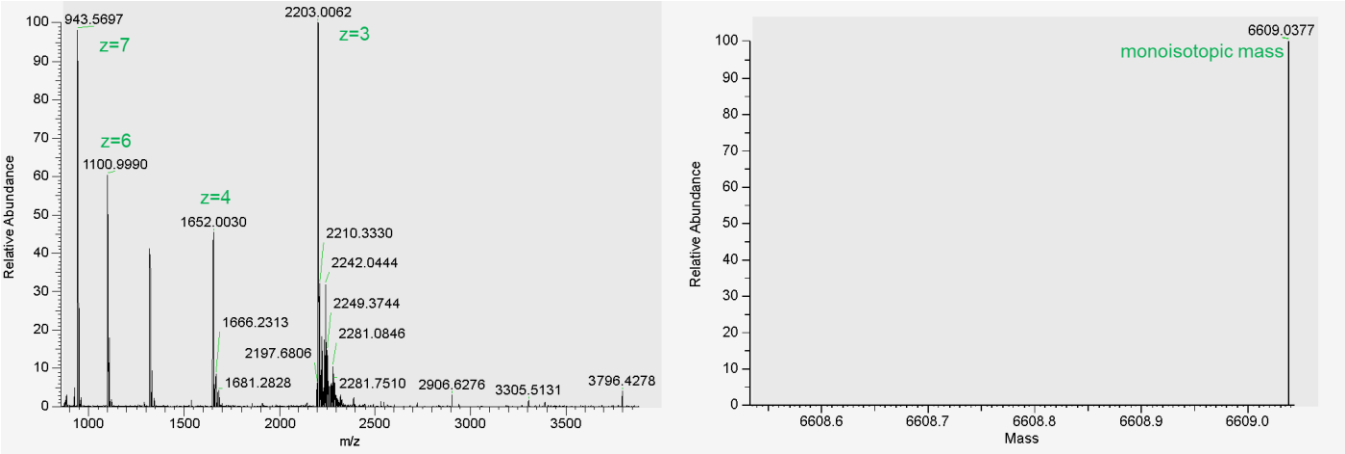

si-EG_3-chol

Theoretical molecular weight: 6963 Da

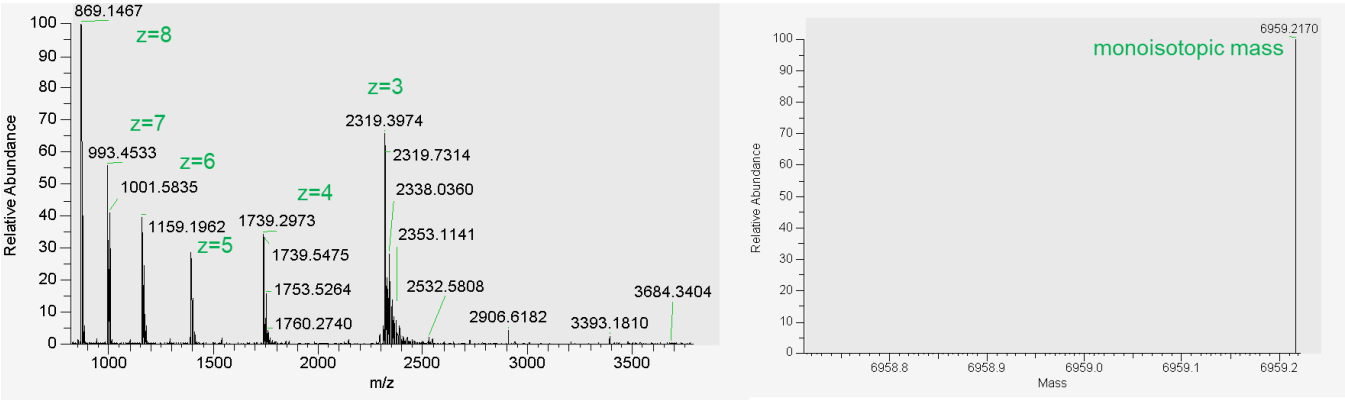

si<$(EG_0L)_2$

Theoretical molecular weight: 7126 Da

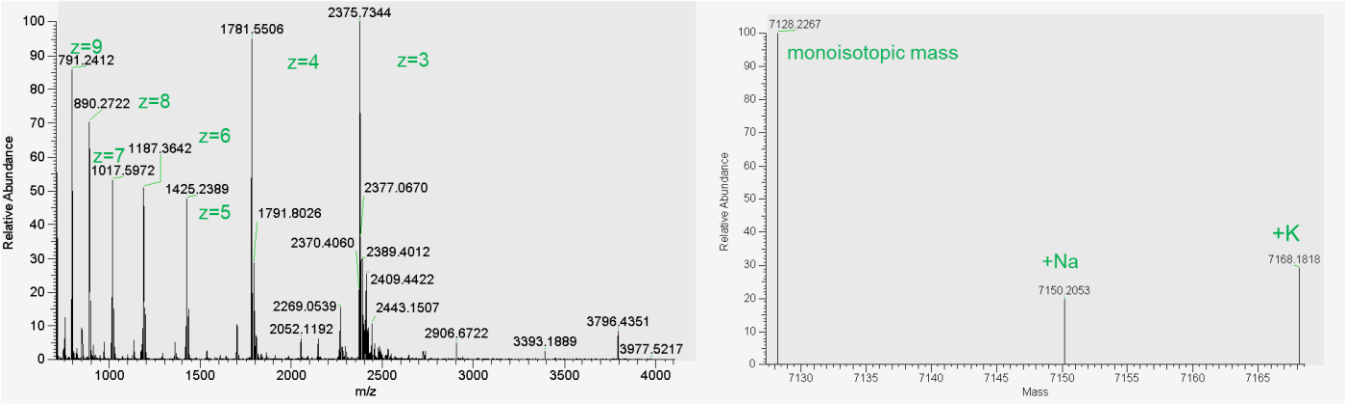

si<$(EG_6L)_2$

Theoretical molecular weight: 7846 Da

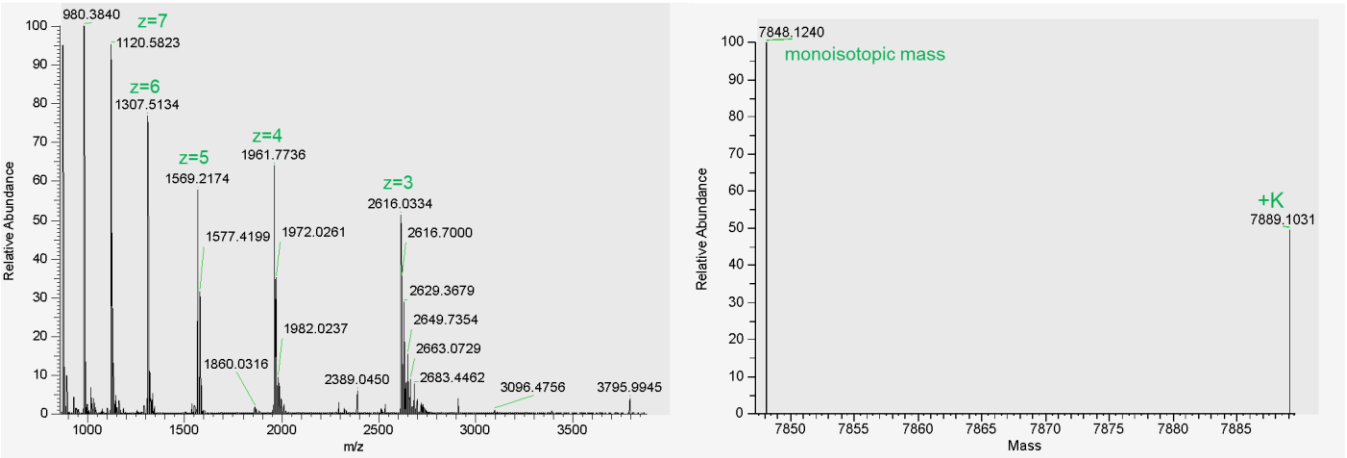

si<$(EG_{18}L)_2$

Theoretical molecular weight: 9291 Da

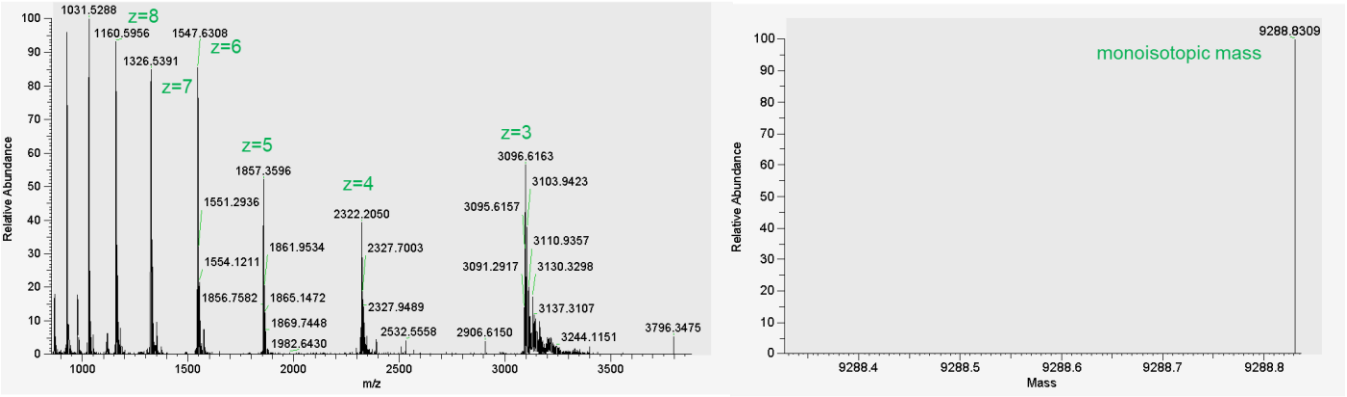

si<$(EG_{30}L)_2$

Theoretical molecular weight: 10,735 Da

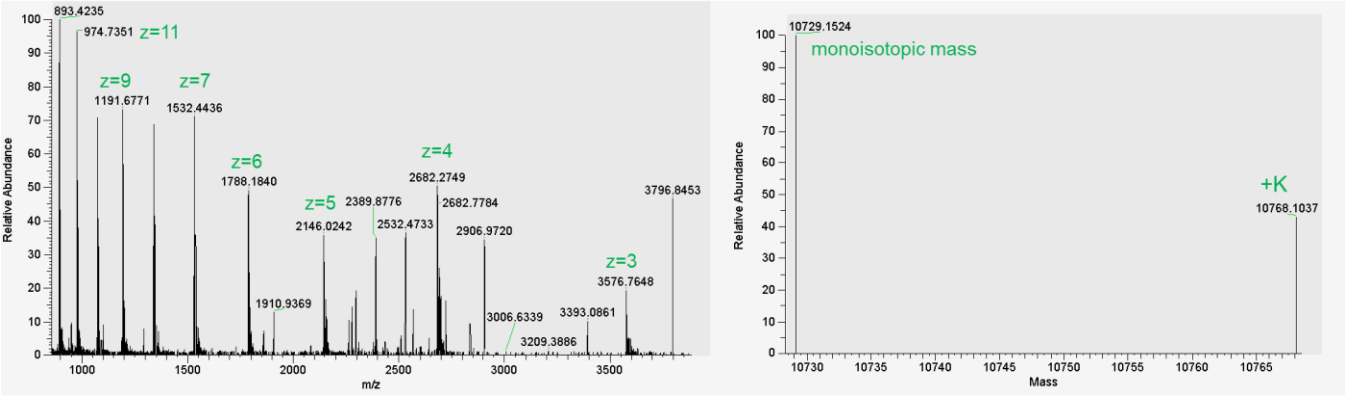

si<$(EG_{18}L)_2$No 5' PS or Binder PS

Theoretical molecular weight: 9115 Da

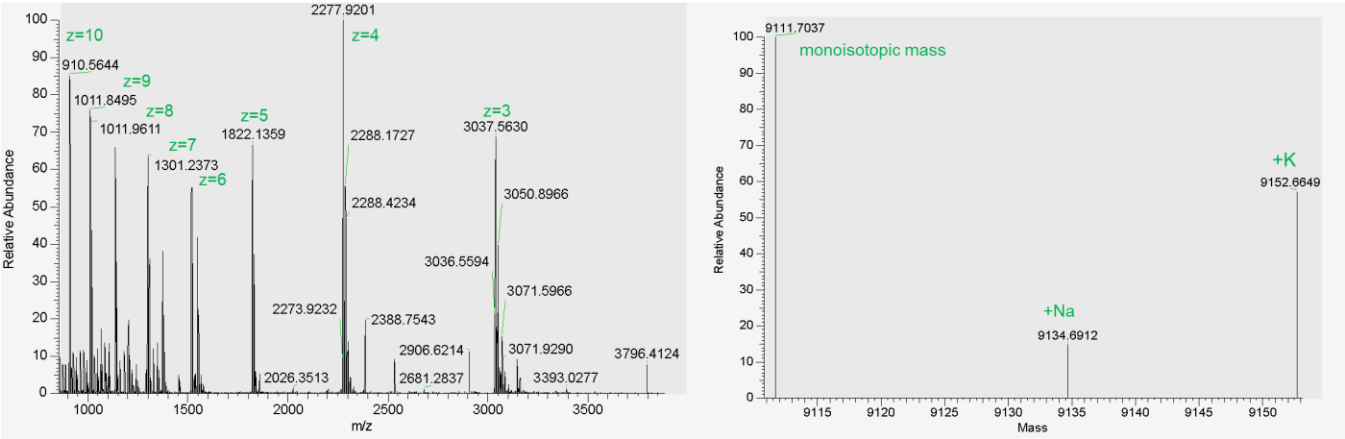

si<$(EG_{18}L)_2$No 5' PS

Theoretical molecular weight: 9260 Da

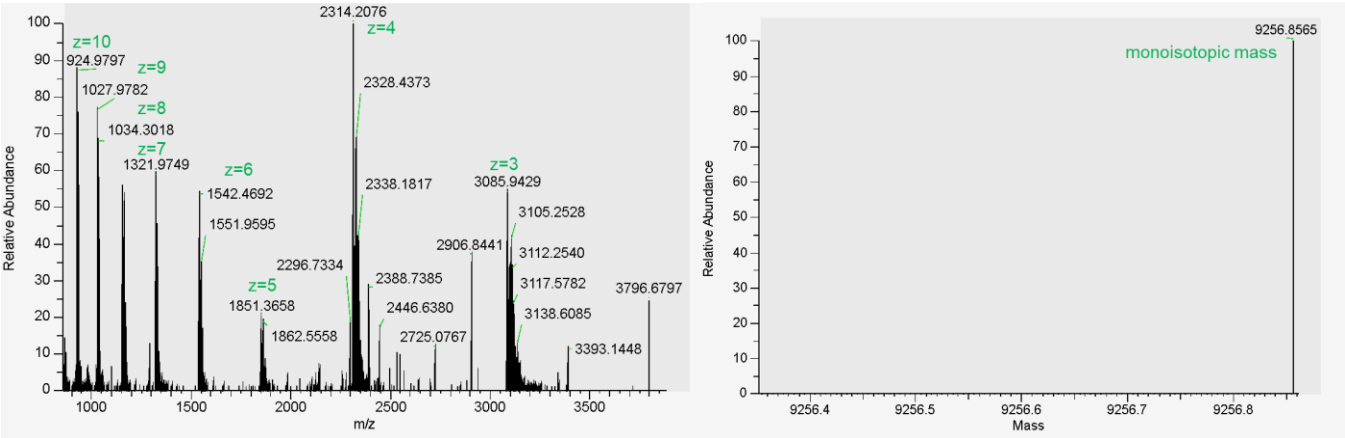

si-EG_{18}<L_2

Theoretical molecular weight: 8211 Da

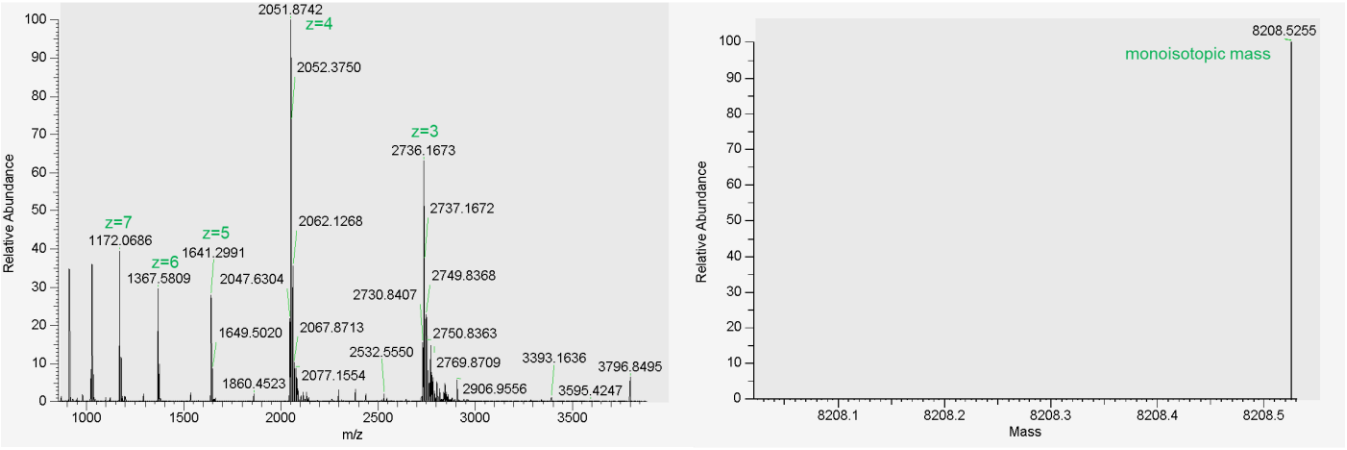

si-EG_{36}<L_2

Theoretical molecular weight: 9292 Da

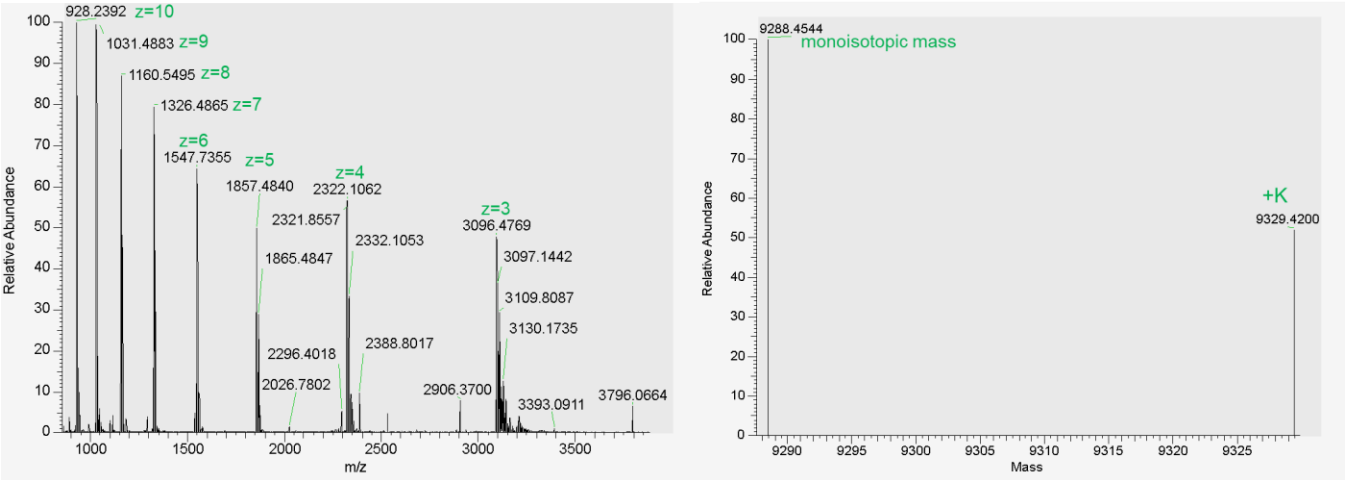

si<($EG_{18}L_{unsaturated}$)$_2$

Target molecular weight 9490

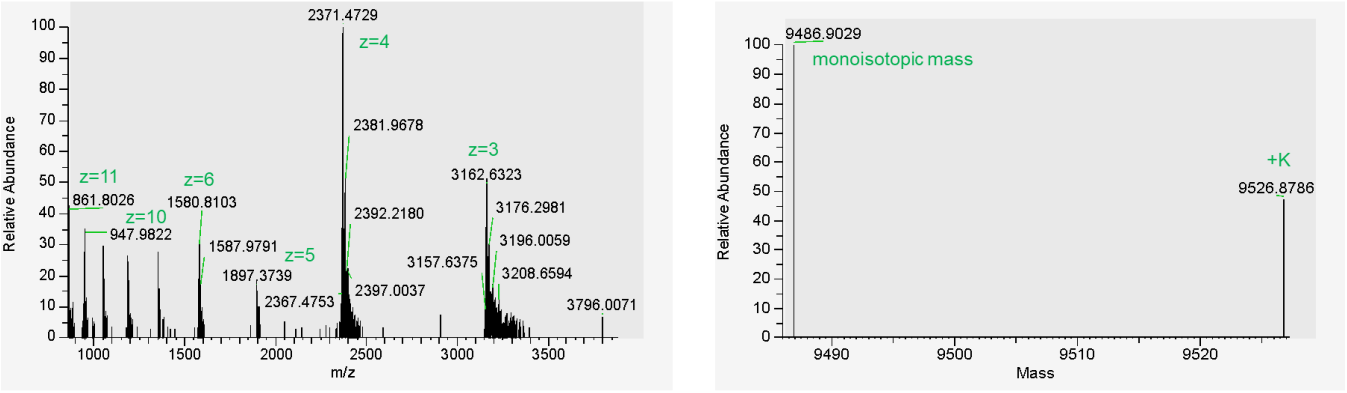

si<$(EG_{18}L_{diacid})_2$

Target molecular weight 9554

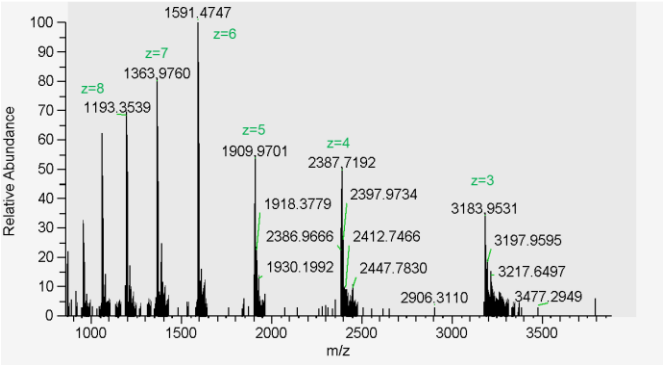

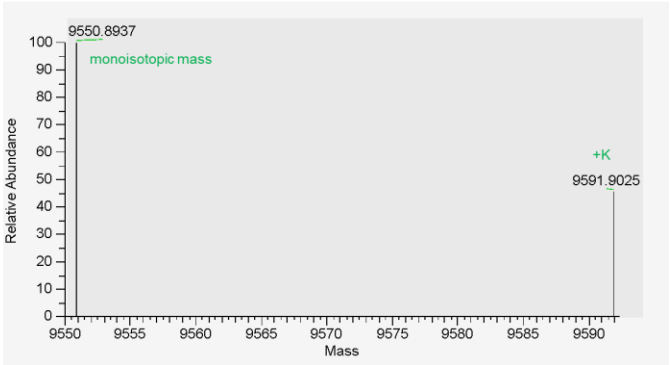

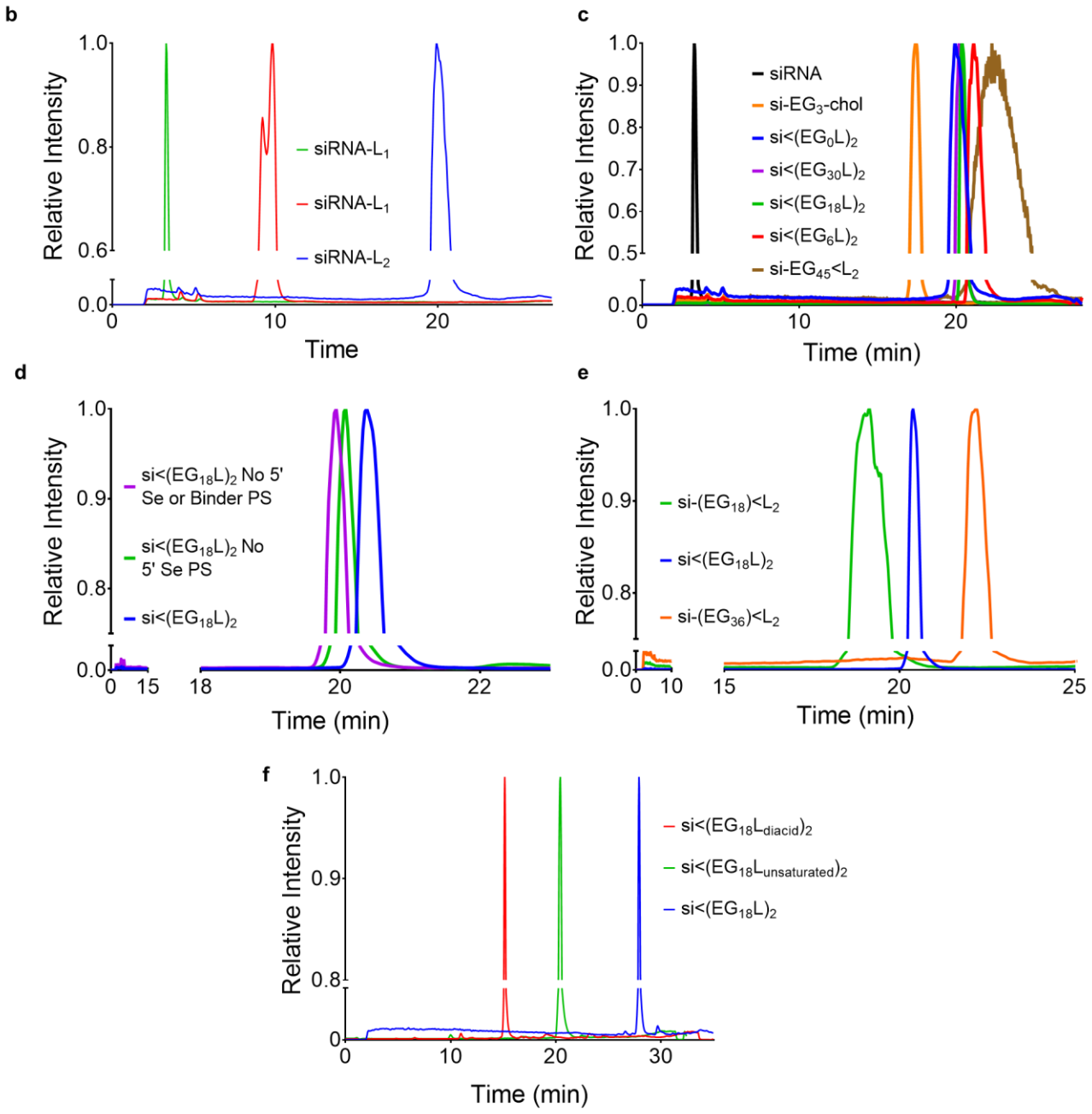

Supplementary Figure 2.1: LC-MS characterization of siRNA and siRNA conjugates.

Conjugate purity and mass fidelity were confirmed by LCMS ESI-. LC was performed using a Waters XBridge Oligonucleotide BEH C18 Column under a linear gradient from 85% A (16.3 mM triethylamine – 400 mM hexafluoroisopropanol) to 100% B (methanol) at 45°C. (A) Full spectrum presented on left and deconvoluted mass presented on right as calculated by ThermoFisher FreeStyle Software. Molecular weight of si<$PEG_{45}L_2$ was validated using MALDI-TOF mass spectrometry.

Chromatograms of valency (B), ethylene glycol (C), phosporothioate content (D), branching architecture (E), and lipid (F) variants displayed with axes adjusted to visualize differences in elution time.

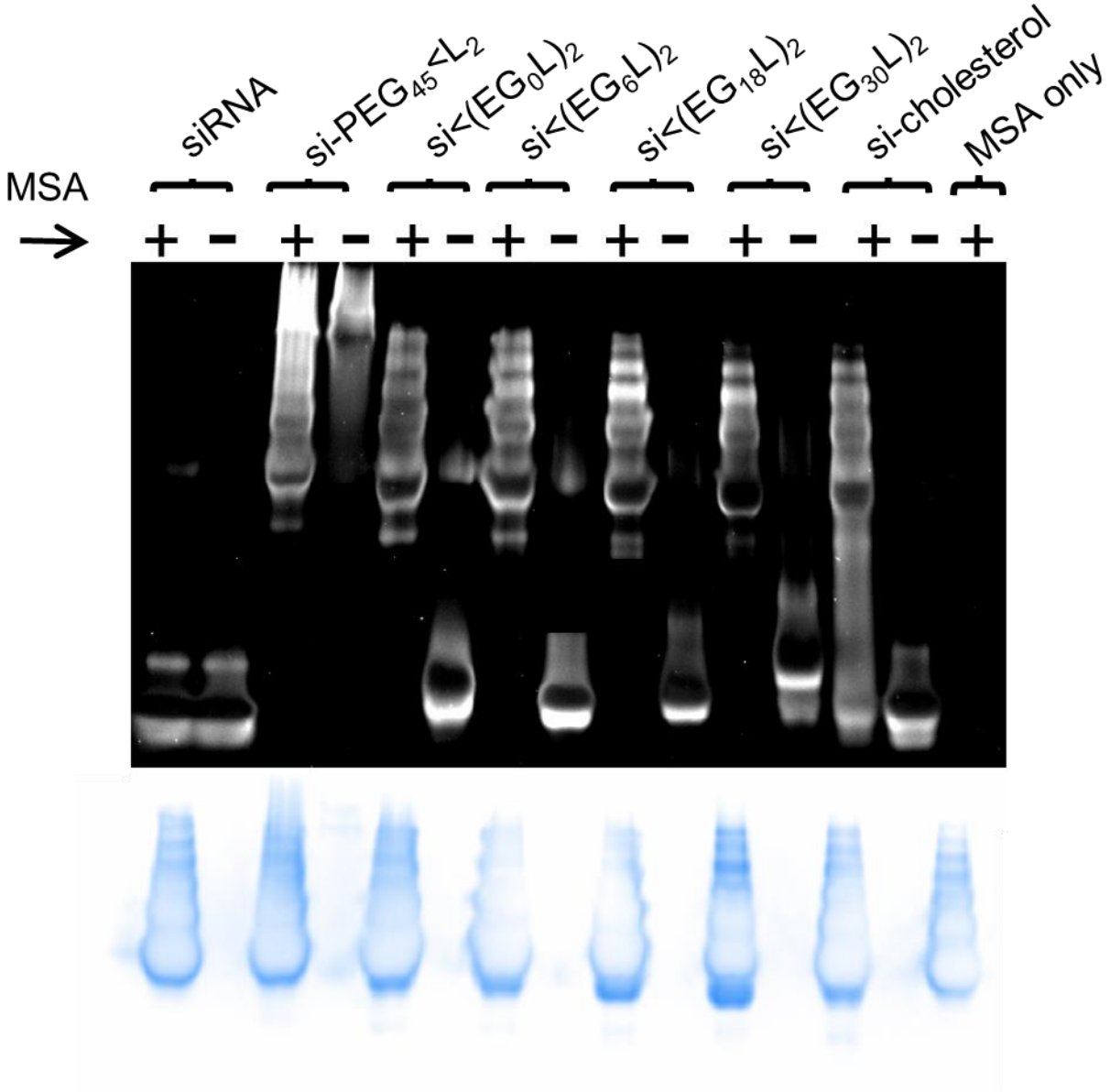

Supplementary Figure 2.2: Native PAGE Gel of siRNA conjugates run in the presence or absence of mouse serum albumin (MSA). Albumin colocalization can be seen by an upwards shift of nucleic acid staining to coincide with albumin (indicated in bottom panel by staining of the same gel with Coomassie blue).

a

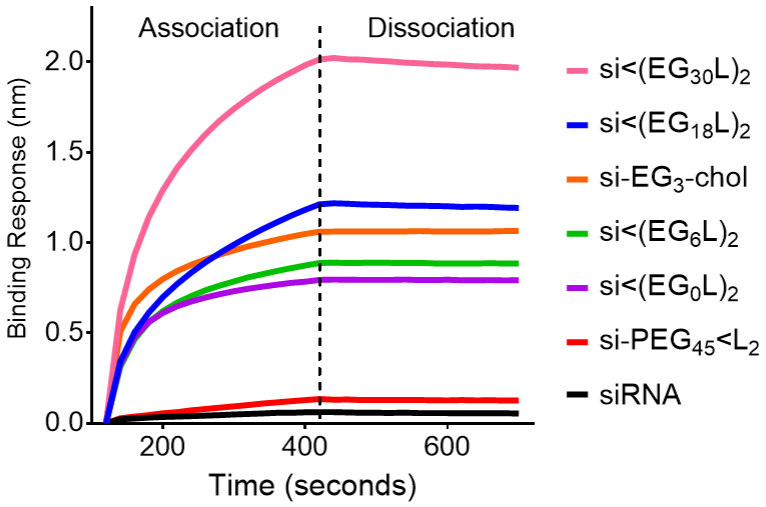

b

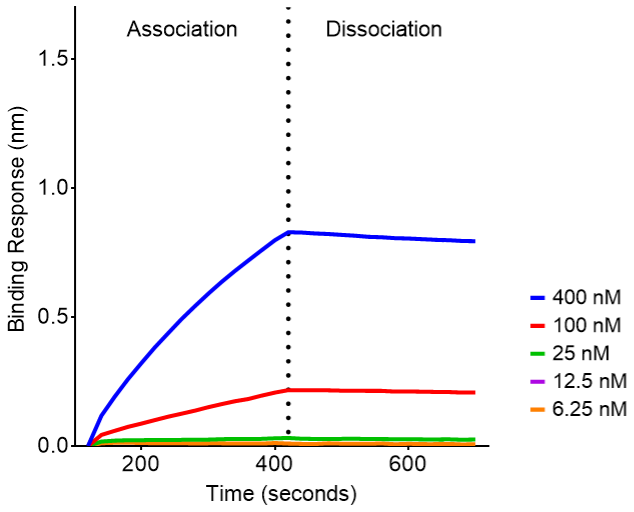

c

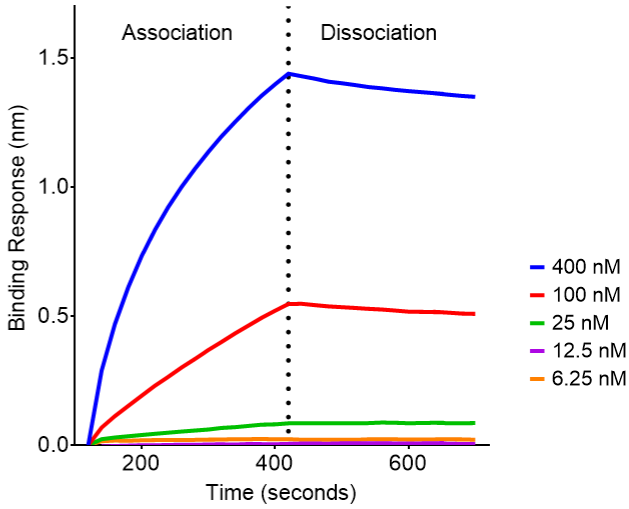

d

	K_D (nM)	k_{on} (1/Ms)	k_{off} (1/s)
si<(EG$_{18}$L)$_2$	30 ± 0.3	6.97×10^3 ±152	2.09×10^{-4} ± 1.75×10^{-6}
si<(EG$_{30}$L)$_2$	9.49 ± 0.1	1.85×10^4 ± 340	1.75×10^{-4} ± 2.09×10^{-6}

Supplementary Figure 2.3: Extended binding kinetics of siRNA conjugate library. (A) Binding response of siRNA conjugates to 400 nM mouse serum albumin as measured by biolayer interferometry. Full panel of B) si<$(EG_{18}L)_2$ and C) si<$(EG_{36}L)_2$ binding responses to HSA used to determine D) binding kinetic parameters.

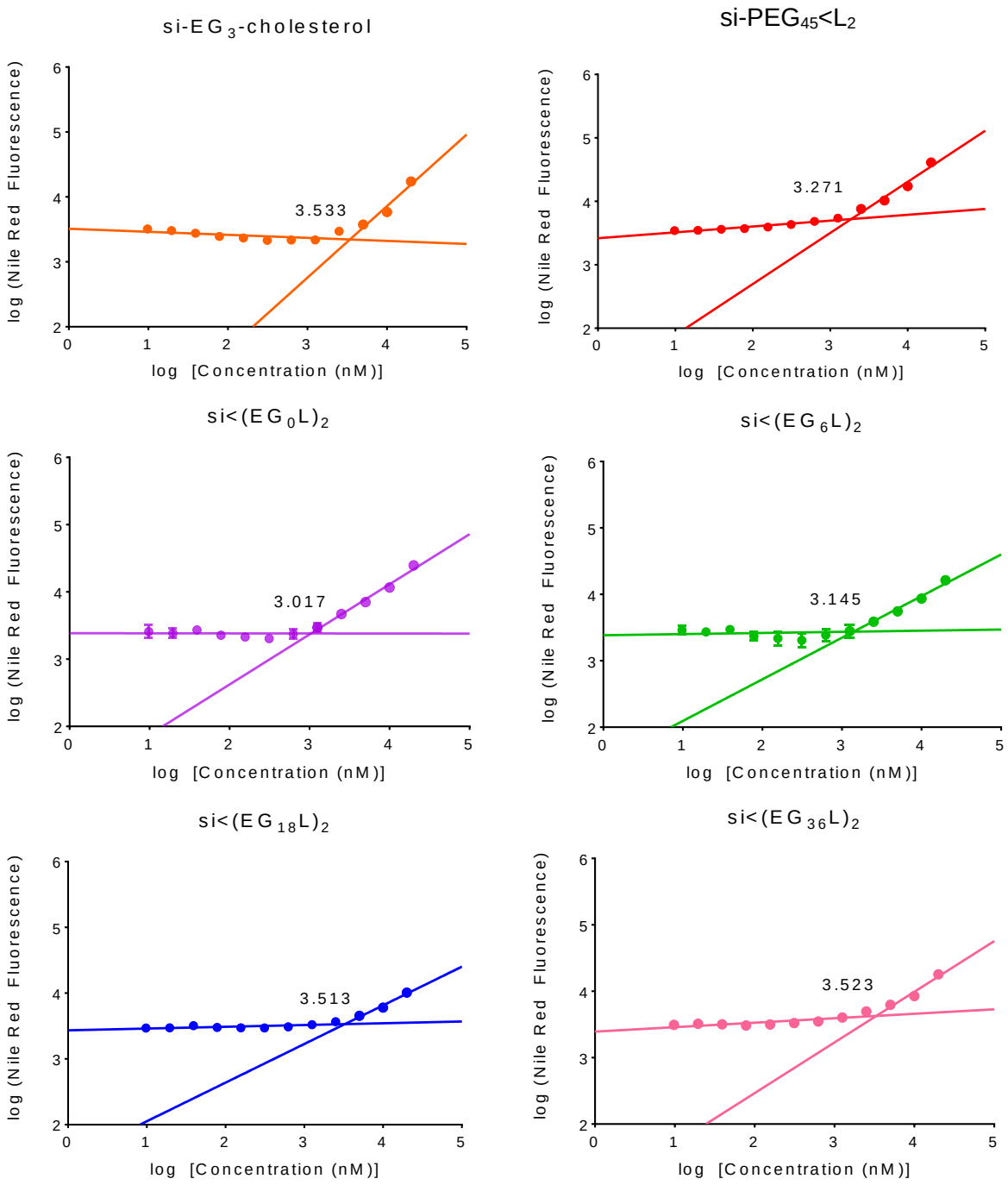

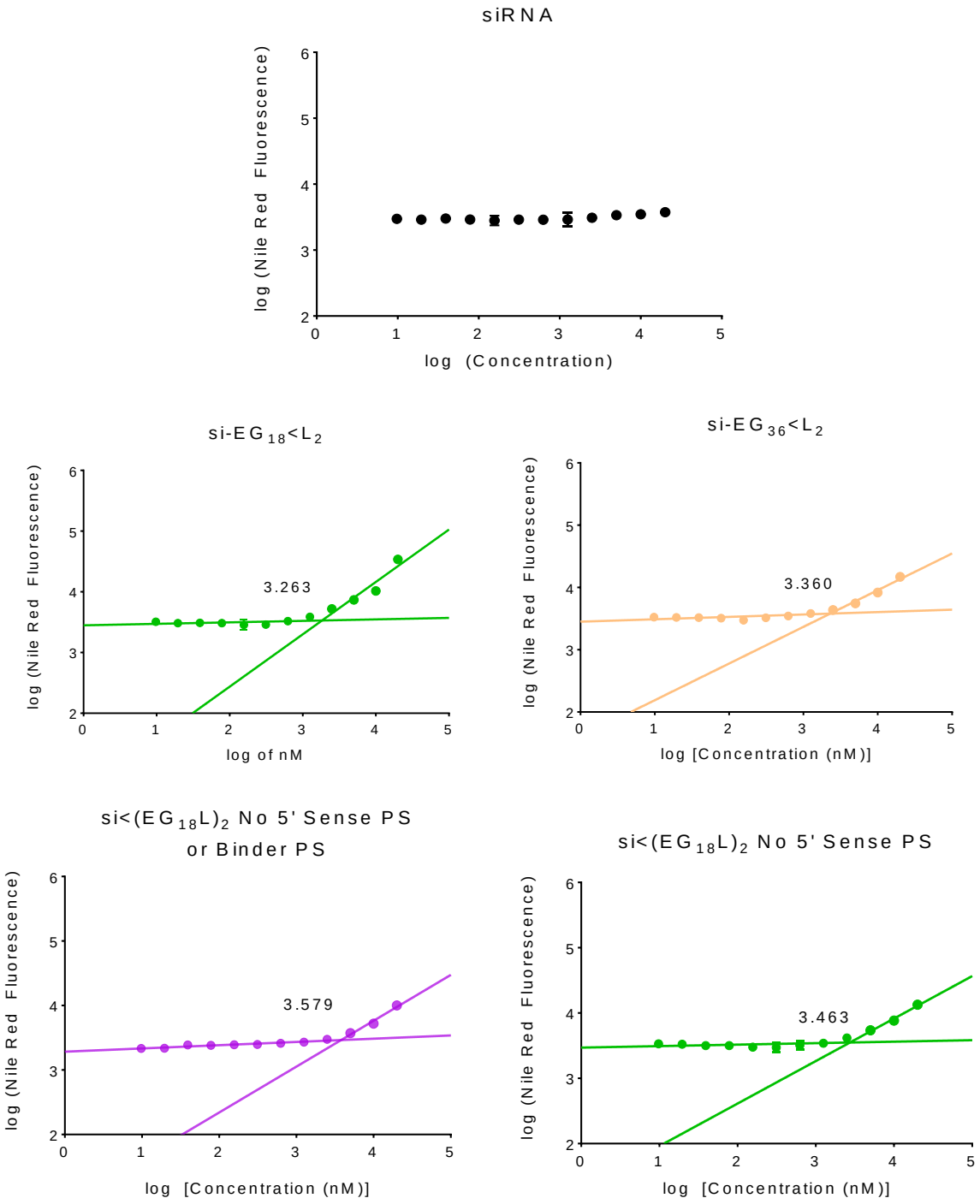

Supplementary Figure 2.4: Critical micelle concentration (CMC) plots for full siRNA conjugate library.

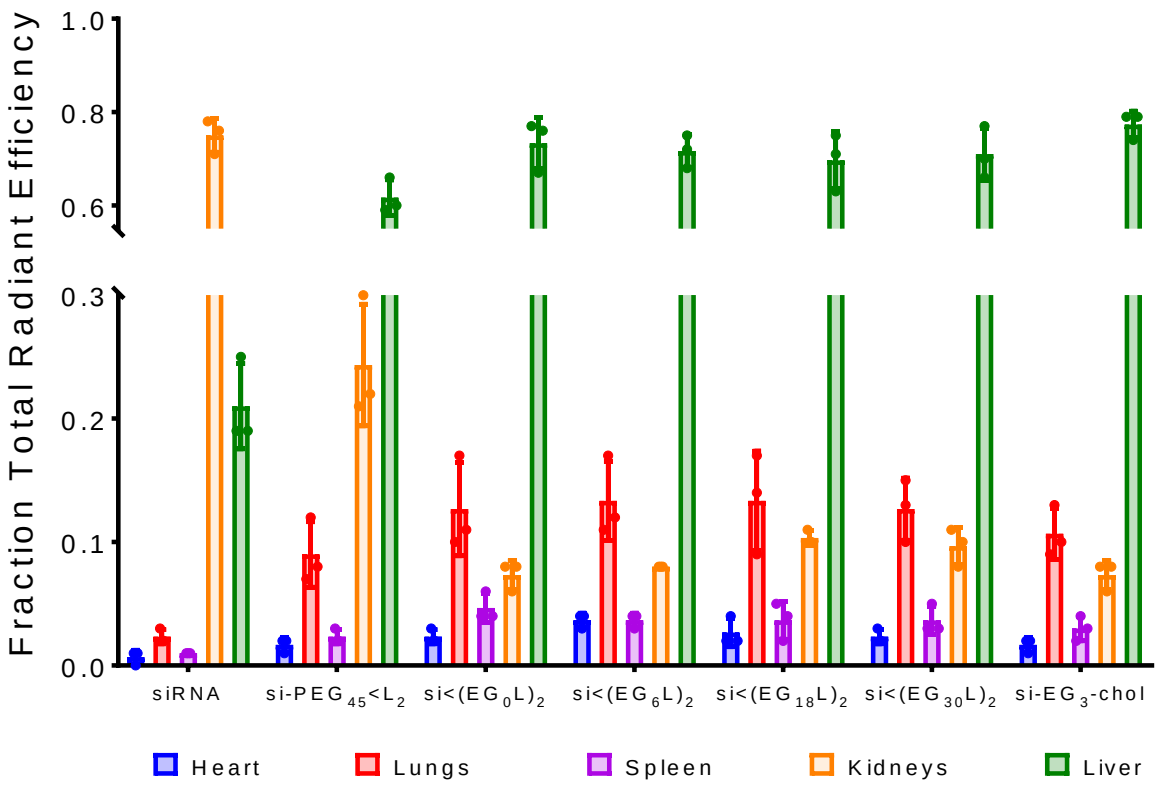

Supplementary Figure 2.5: Biodistribution of Cy5-labeled siRNA conjugates in non-tumor bearing mice. Organs harvested approximately 45 minutes after injection at 1mg/kg intravenously *via* tail vein (n=3).

Supplementary Table 2.2: Pharmacokinetic parameters for full siRNA conjugate library determined from intravital microscopy

		$t_{1/2}$ (min)	$AUC_{0\text{-}35m}$ (μg·min)/(mL)	CL (mL)/(min)
	siRNA	14 ± 3.5	210 ± 25	0.069 ± 0.012
	si-EG_3-cholesterol	28 ± 12	410 ± 42	0.025 ± 0.0079
	si-PEG_{45}<L_2	27 ± 5.3	390 ± 25	0.026 ± 0.0046
EG Variants	si<$(EG_0L)_2$	33 ± 6.6	416 ± 55	0.028 ± 0.0059
EG Variants	si<$(EG_6L)_2$	36 ± 4.6	450 ± 15	0.019 ± 0.0022
EG Variants	si<$(EG_{18}L)_2$	64 ± 23	470 ± 52	0.012 ± 0.0032
EG Variants	si<$(EG_{30}L)_2$	37 ± 6.6	440 ± 36	0.019 ± 0.0043
PS Variants	si<$(EG_{18}L)_2$ No 5'Se PS	37 ± 12	430 ± 50	0.020 ± 0.0060
PS Variants	si<$(EG_{18}L)_2$ No 5'Se or Binder PS	15 ± 1.5	300 ± 36	0.047 ± 0.0070
Branching Variants	si-(EG_{18})<L_2	67 ± 32	490 ± 35	0.012 ± 0.0070
Branching Variants	si-(EG_{36})<L_2	41 ± 13	450 ± 27	0.018 ± 0.0050
Lipid Variants	si<$(EG_{18}L_{diacid})_2$	47 ± 21	469 ± 64	0.017 ± 0.0073
Lipid Variants	si<$(EG_{18}L_{unsaturated})_2$	34 ± 26	391 ± 121	0.029 ± 0.016

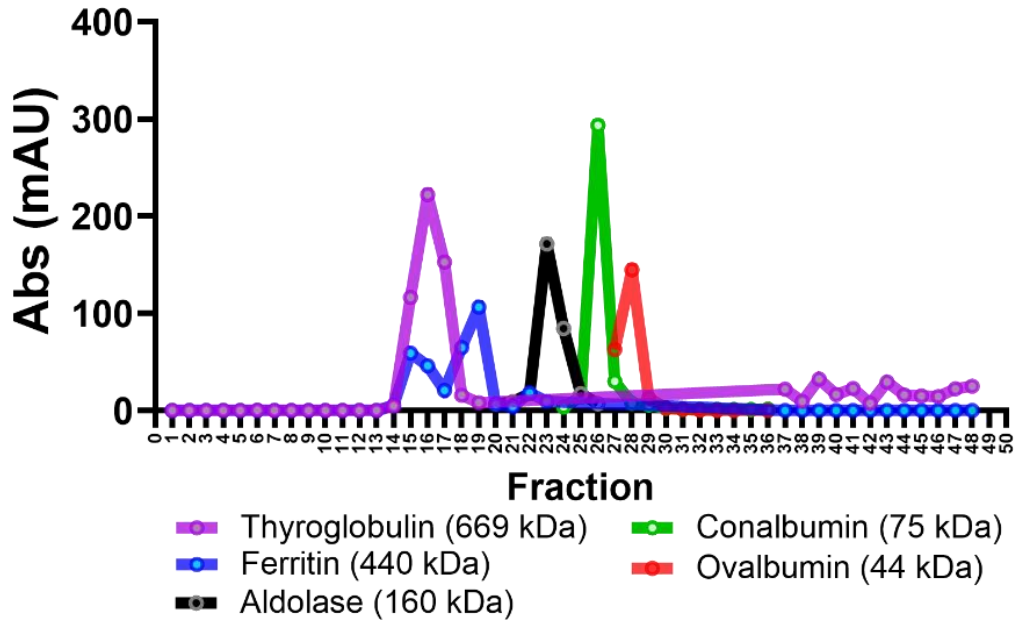

Supplementary Figure 2.6: Size exclusion chromatography (SEC) of protein standards.

Representative protein standards run on SEC system to demonstrate resolution by molecular weight.

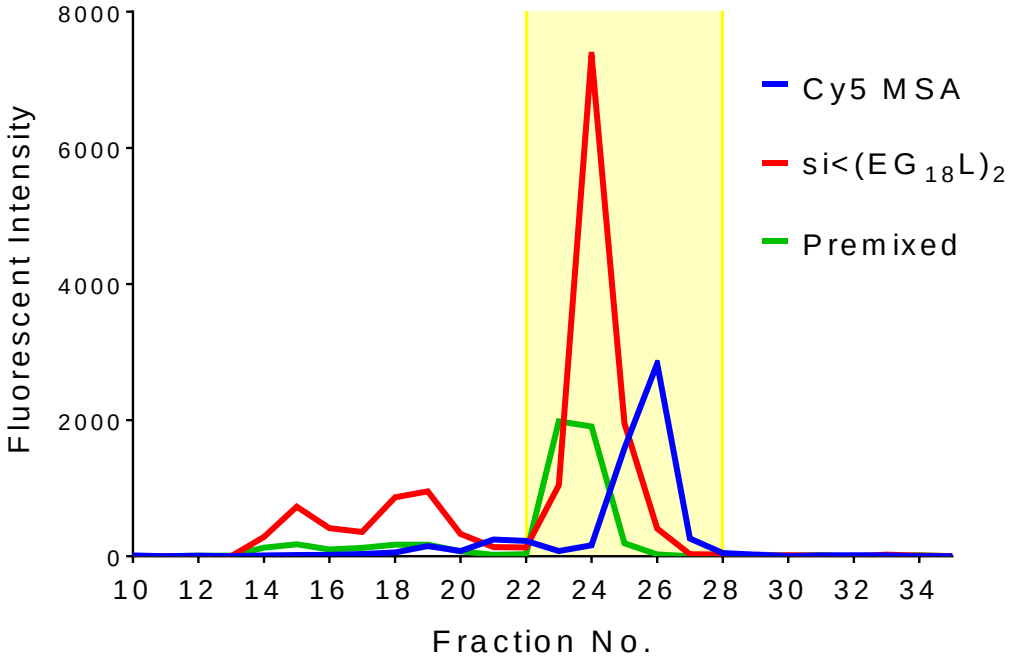

Supplementary Figure 2.7: Size exclusion chromatography (SEC) of mouse plasma after injection with siRNA conjugate +/- MSA versus MSA alone. Mice were injected at 1 mg/kg intravenously via

tail vein and plasma was harvested approximately 45 minutes after injection**.** Fractions highlighted in yellow were used for calculating albumin-bound fraction.

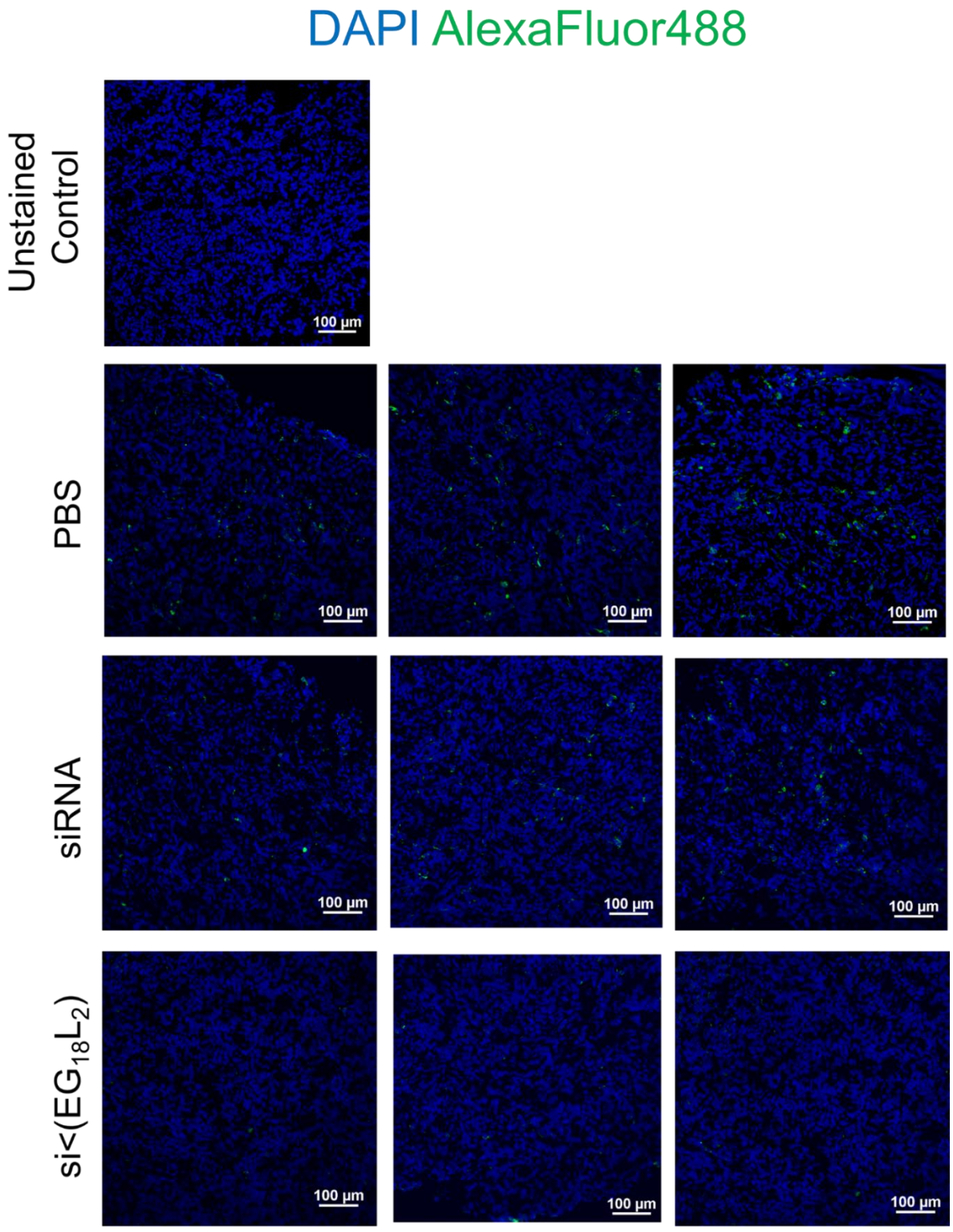

Supplementary Figure 2.8: Extended images of tumors sectioned and stained for Firefly Luciferase protein (green, Alexafluor488) and cell nuclei (blue, DAPI).

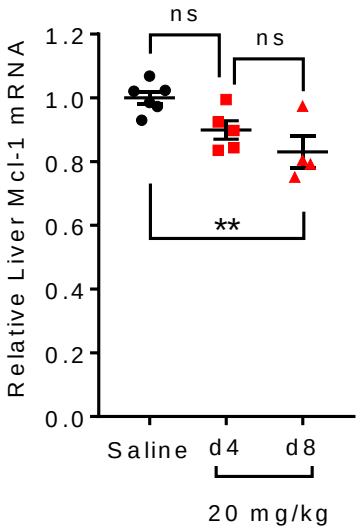

Supplementary Figure 2.9: Liver knockdown of Mcl-1 mRNA after bolus i.v. injection of si$_{Mcl-1}$<(EG$_{18}$L)$_2$. Significance assessed by 1-way ANOVA with Tukey's multiple comparisons test (n=4-6).

Appendix B: Supplementary Material for Chapter 3

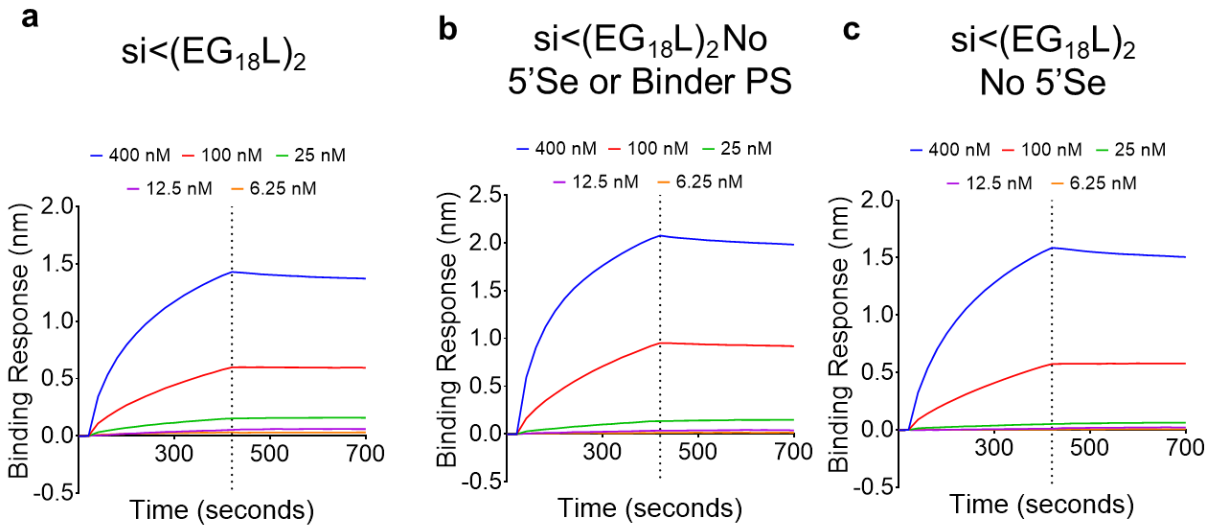

d

	KD (nM)	ka (1/Ms)	kdis (1/s)
si<(EG$_{18}$L)$_2$	3.89 ± 0.13	2.35x10^4 ± 6.37	9.14x10^{-5} ± 3.09x10^{-6}
si<(EG$_{18}$L)$_2$ No 5'Se or Binder PS	2.81 ± 0.10	3.01x10^4 ± 7.47	8.46x10^{-5} ± 3.05x10^{-6}
si<(EG$_{18}$L)$_2$ No 5'Se	5.58 ± 0.10	2.08x10^4 ± 3.91	1.16x10^{-4} ± 2.07x10^{-6}

Supplementary Figure 3.1: Extended characterization of si<(EG$_{18}$L)$_2$ phosphorothioate variants. **(**A-C) Full panel of binding responses to HSA at varied concentrations measured by biolayer interferometry used to determine D) binding kinetic parameters

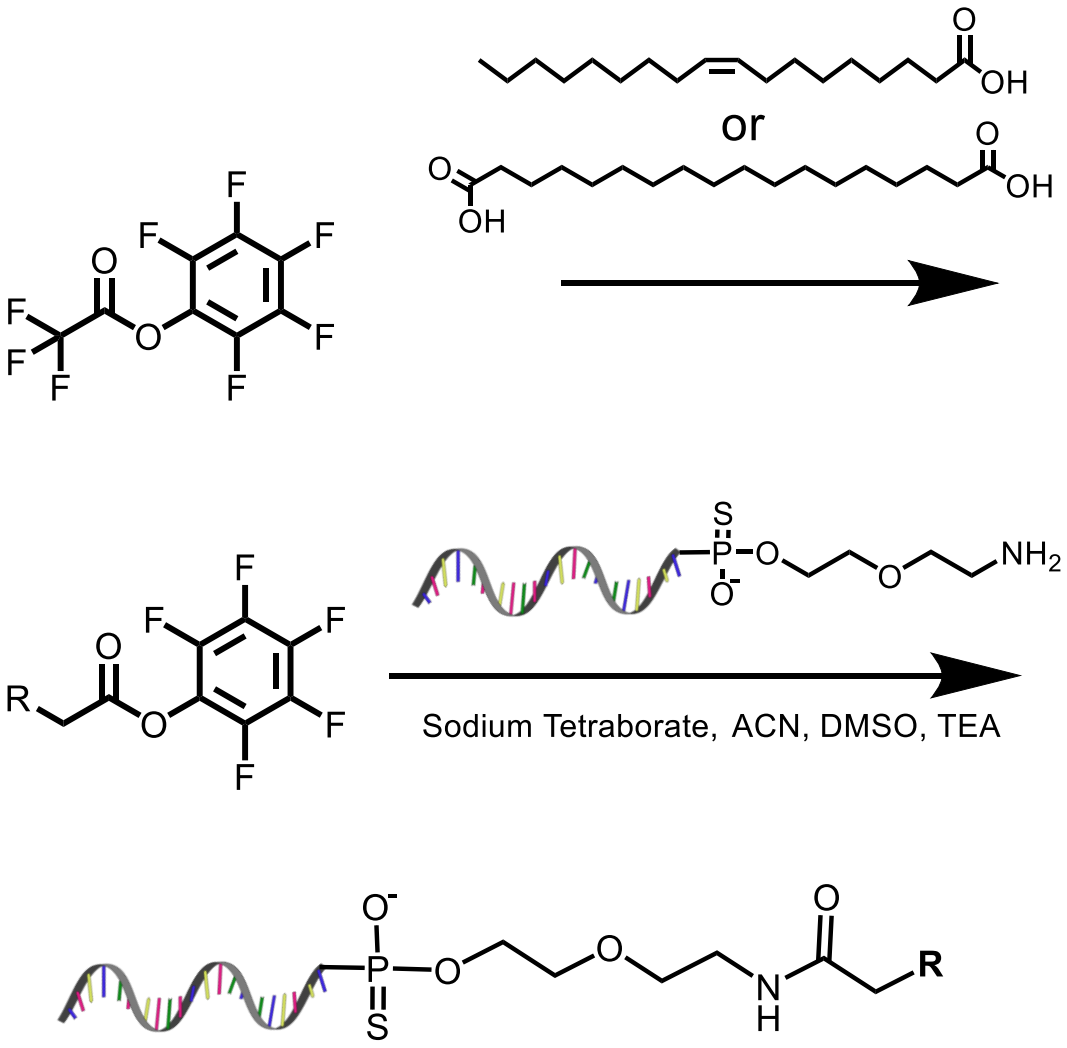

Supplementary Figure 3.2: Graphic overview of synthesis of si<(EG$_{18}$L)$_2$ lipid variants

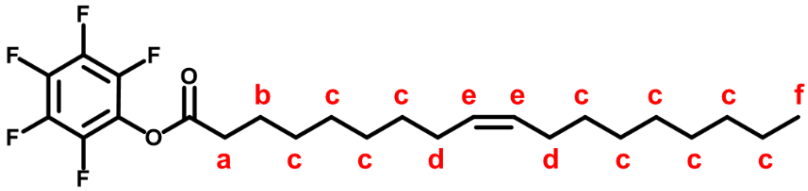
F
F
F
F
F
O
O
a c c d d c c c
b c c e e c c c f

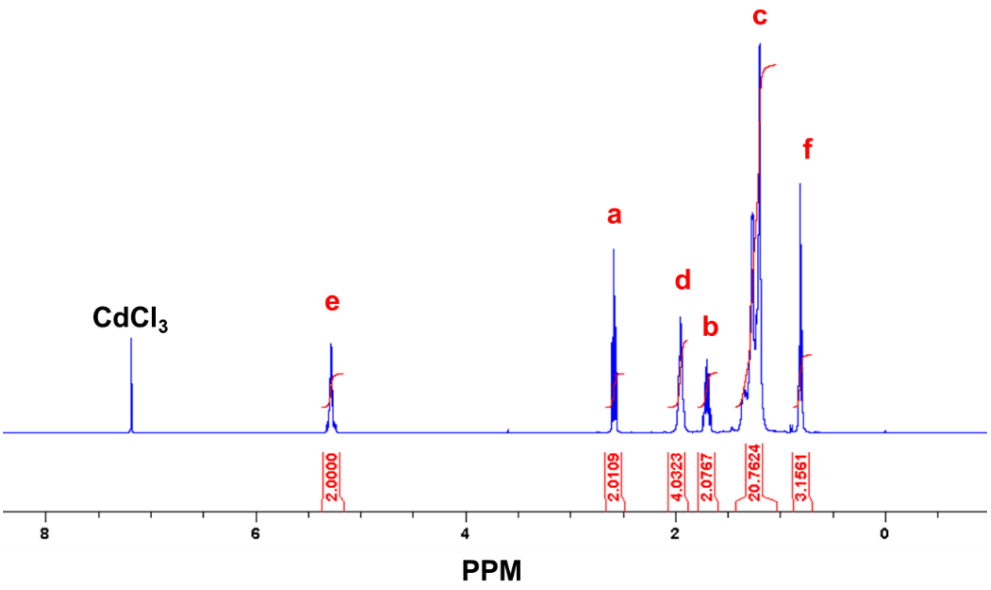
CdCl3
e
a
d
b
c
f
2.0000
2.0109
4.0323
2.0767
20.7624
3.1561
8
6
4
2
0
PPM

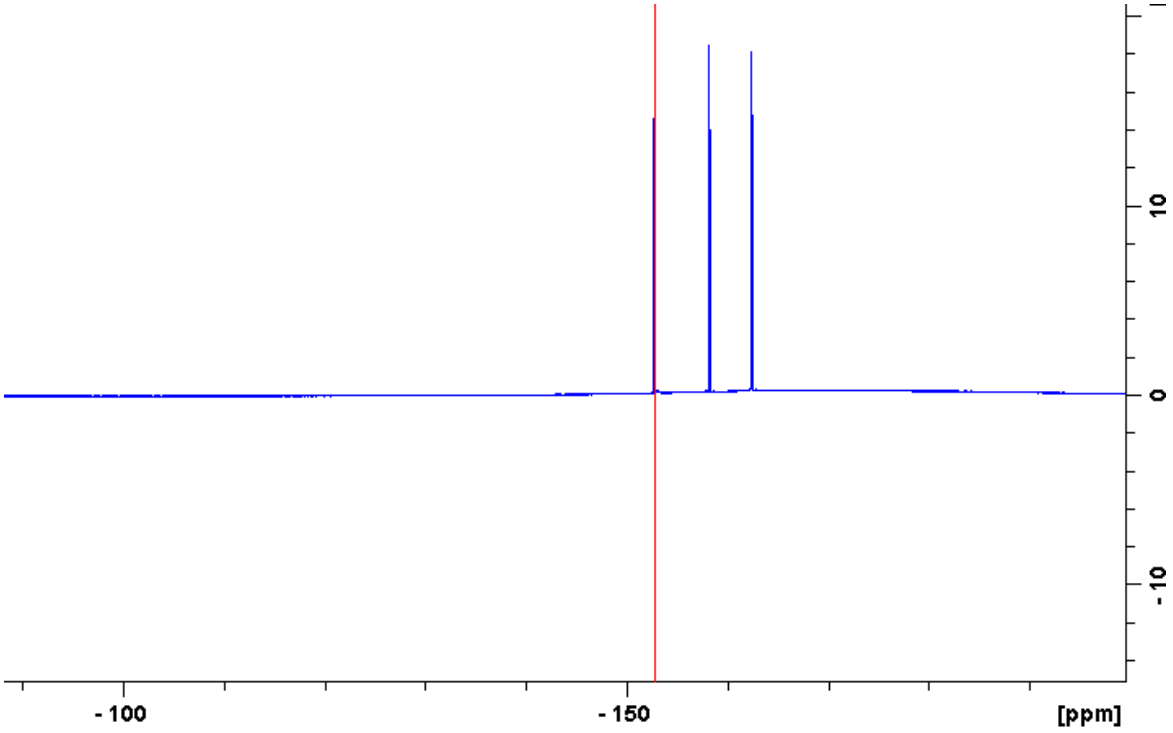
10
0
-10
- 100
- 150
[ppm]

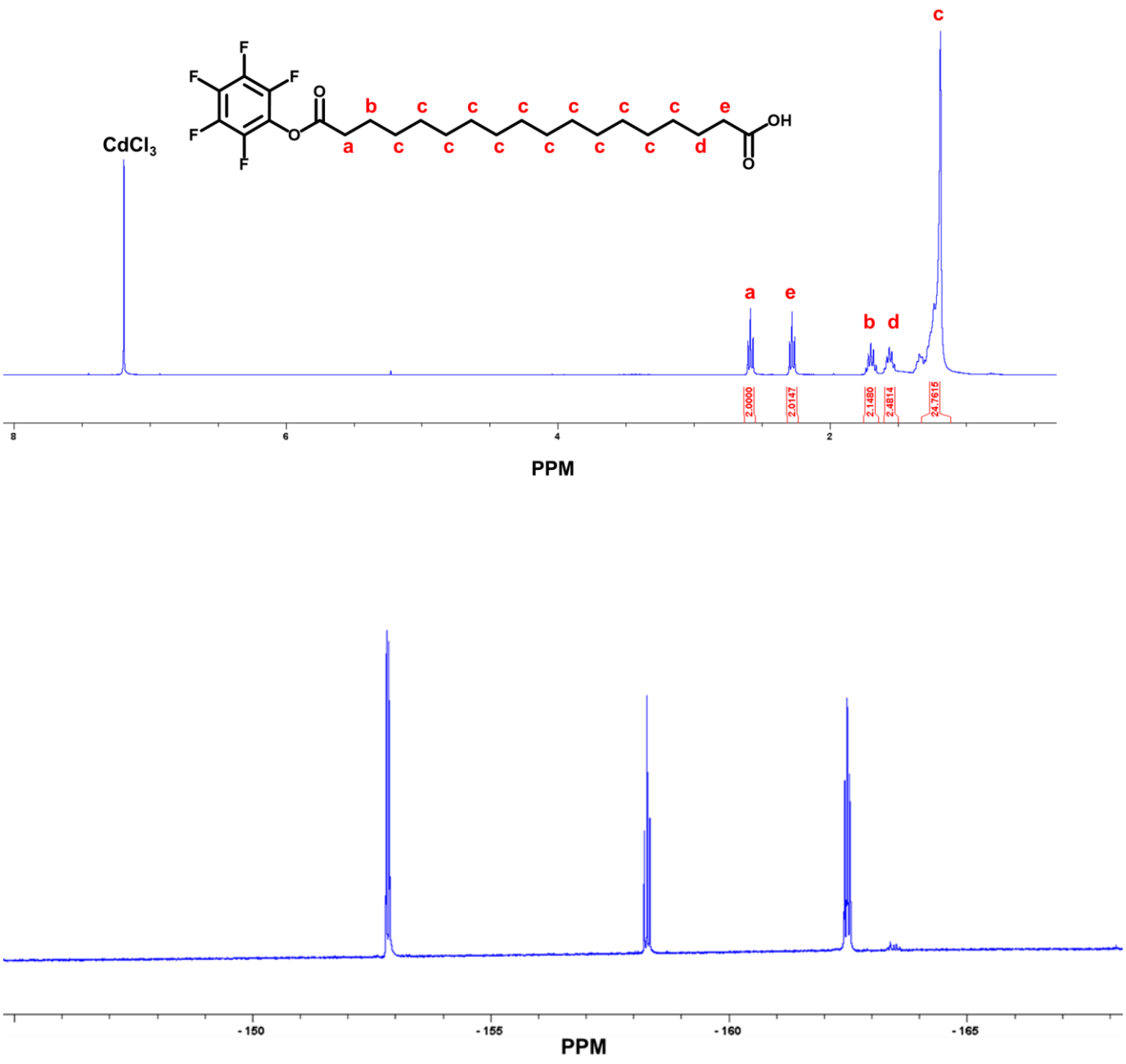

Supplementary Figure 3.3: H and F NMR traces of pentafluorophenyl-lipid variants after silica gel chromatography.

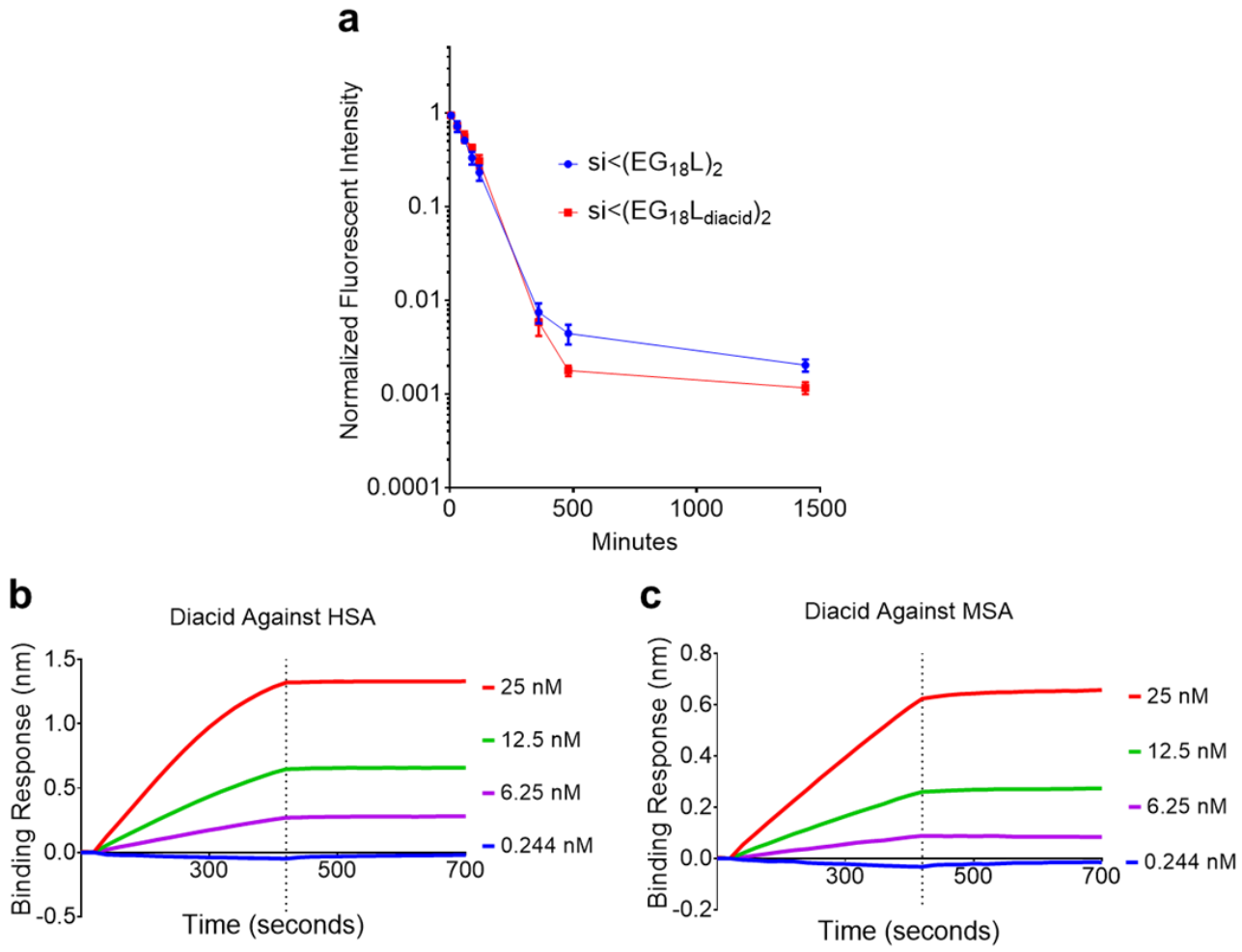

d HSA Binding Kinetics

	KD (nM)	ka (1/Ms)	kdis (1/s)
si<(EG$_{18}$L$_{diacid}$)$_2$	0.15 ± 0.002	1.31×10^{5} ± 712	1.93×10^{-5} ± 2.92×10^{-6}
si<(EG$_{18}$L)$_2$	30 ± 0.3	6.97×10^{3} ±152	2.09×10^{-4} ± 1.75×10^{-6}

Supplementary Figure 3.4: Extended characterization of diacid-modified si<(EG$_{18}$L)$_2$.
(A) Mice were injected intravenously with 5 mg/kg of Cy5-labeled siRNA conjugate (n=3-4). At various timepoints, blood was sampled from the opposite vein from injection and fluorescence was measured to determine PK profiles at later timepoints. (B-C) Binding responses to HSA and MSA at

varied concentrations measured by biolayer interferometry used to determine D) binding kinetic parameters

Appendix C: Supplementary Material for Chapter 4

Supplementary Table 4.1: siRNA Sequences

Gene/Strand	Sequence (5' to 3')
Mcl-1 (Human) Antisense	(PHO)(MeA)*(fA)*(MeA) (fU) (MeU) (fC) (MeG) (fA) (MeU) (fA) (MeC) (fU) (MeU) (fC) (MeC) (fU) (MeU)*(fC)*(MeG)
Mcl-1 (Human) Sense	(fC)*(MeG)*(fA) (MeA) (fG) (MeG) (fA) (MeA) (fG) (MeU) (fA) (MeU) (fC) (MeG) (fA) (MeA) (fU)*(MeU)*(fU)
Mcl-1 (Human and Mouse) Antisense	(PHO) (MeU)*(fU)*(MeC) (fU) (MeG) (fC) (MeU) (fA) (MeA) (fU) (MeG) (fG) (MeU) (fU) (MeC) (fG) (MeA)*(fU)*(MeG)
Mcl-1 (Human and Mouse) Sense	(fC)*(MeA)*(fU) (MeC) (fG) (MeA) (fA) (MeC) (fC) (MeA) (fU) (MeU) (fA) (MeG) (fC) (MeA) (fG)*(MeA)*(fA)
Control Antisense	(PHO) (MeU)*(fU)*(MeC) (fA) (MeU) (fU) (MeA) (fU) (MeC) (fA) (MeG) (fU) (MeG) (fC) (MeA) (fA) (MeU)*(fU)*(MeG)
Control Sense	(fC)*(MeA)*(fA) (MeU) (fU) (MeG) (fC) (MeA) (fC) (MeU) (fG) (MeA) (fU) (MeA) (fA) (MeU) (fG)*(MeA)*(fA)
Phosphorothioate bond (X)(X)* *Phosphodiester bond (X) (X)* *2'F substituted base (fX)* *2'OMe substituted base (MeX)*	

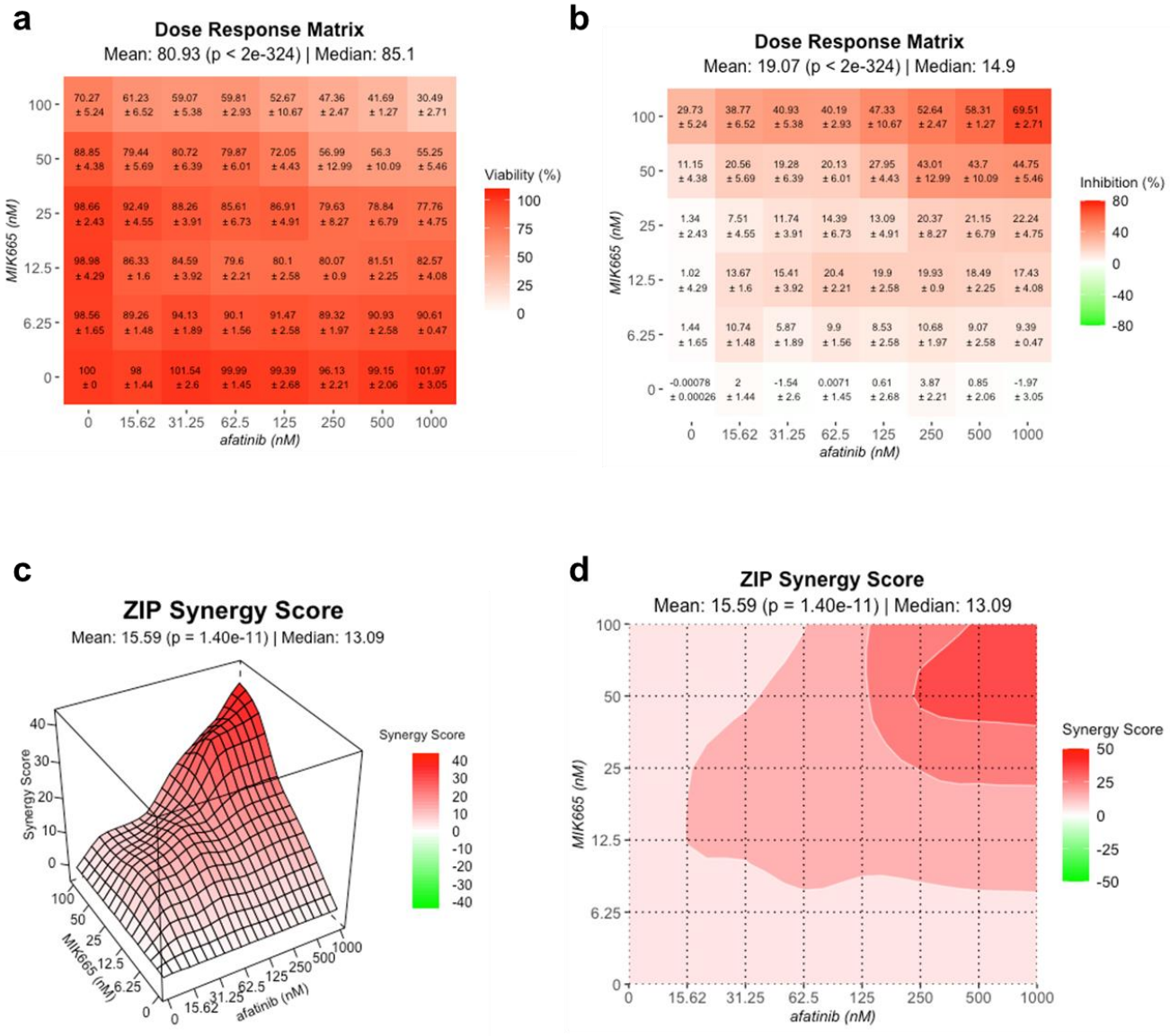

Supplementary Figure 4.1: Dose response matrices for (A) viability and (B) inhibition for co-treatment with MIK 665 and EGFR inhibitor afatinib in HCC70 cells. ZIP synergy score of co-treatment depicted in (C) three dimensions and (D) contour mapped.

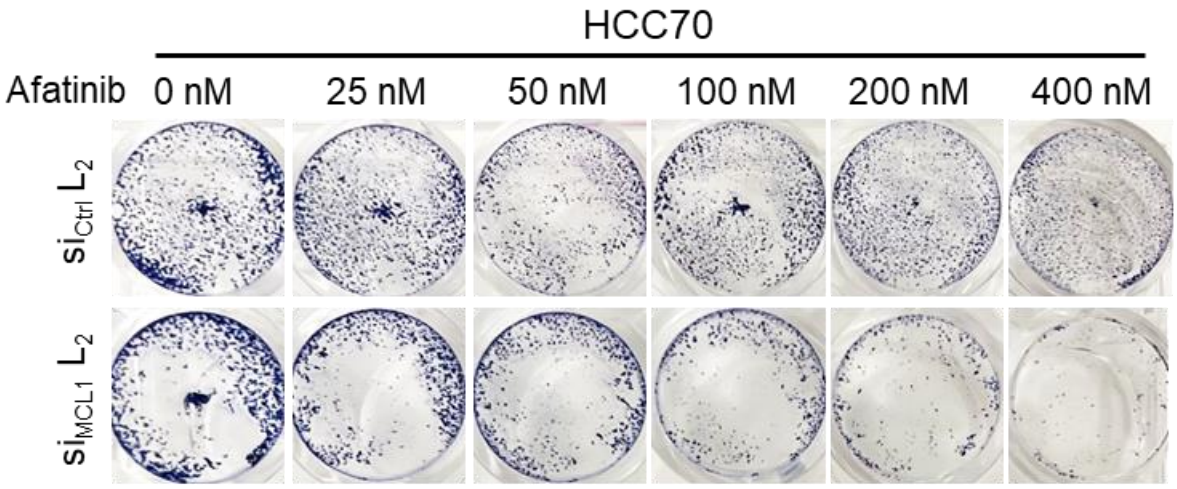

Supplementary Figure 4.2: Images of colony assay after treatment with siRNA conjugate (31.25 nM) with EGFR inhibitor afatinib for a total duration of 96 h.

BD FACSDiva 8.0.1

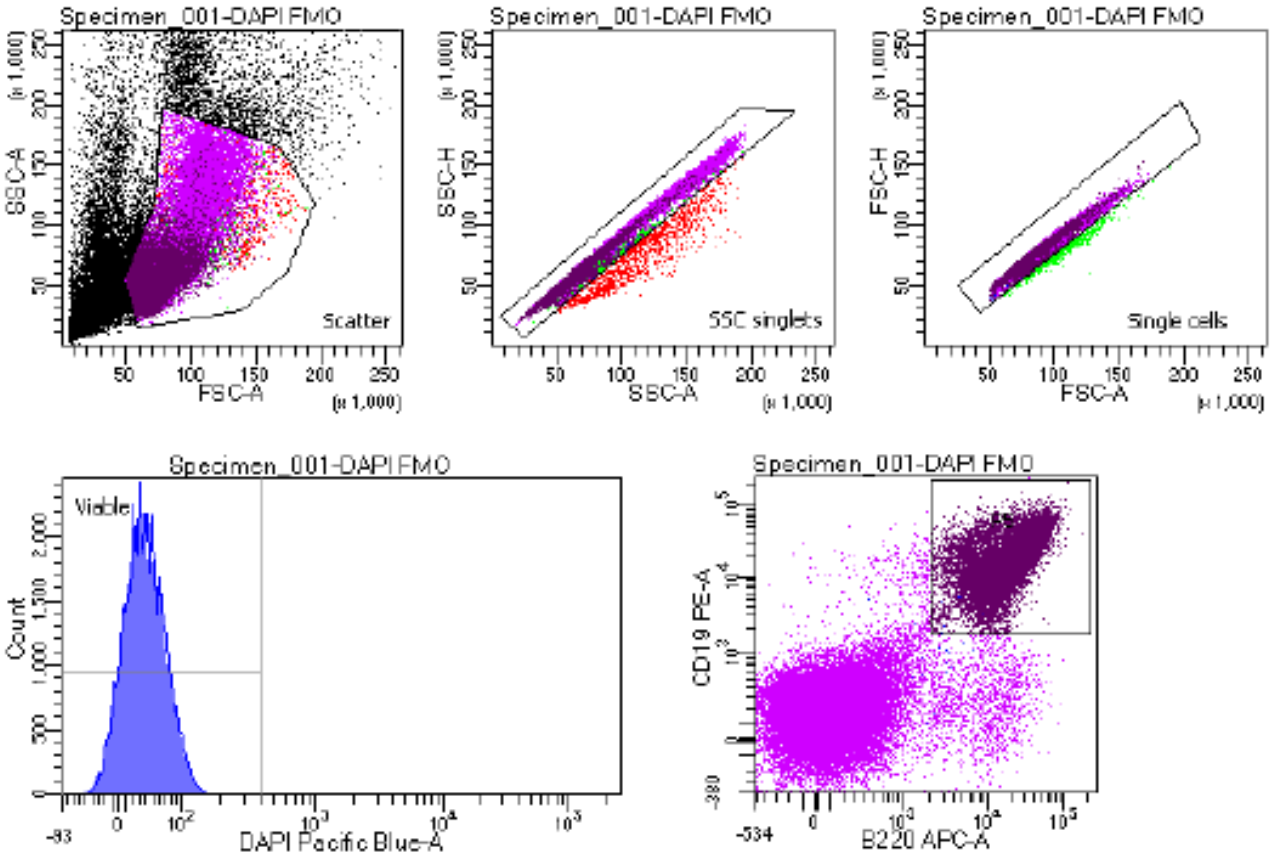

Tube: DAPI FMO

Population	#Events	%Parent	%Total
All Events	81,448	####	100.0
Scatter	52,307	64.2	64.2
SSC singlets	51,112	97.7	62.8
Single cells	50,376	98.6	61.9
Viable	50,302	99.9	61.8
P5	23,910	47.5	29.4

BD FACSDiva 8.0.1

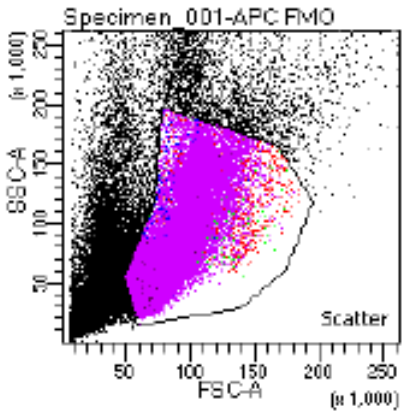

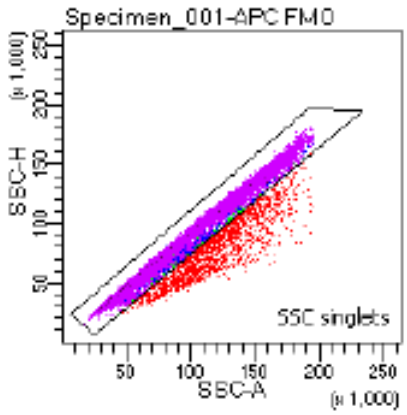

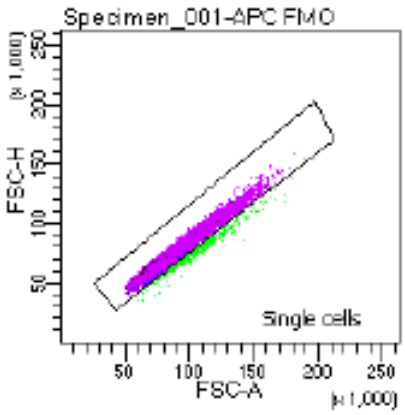

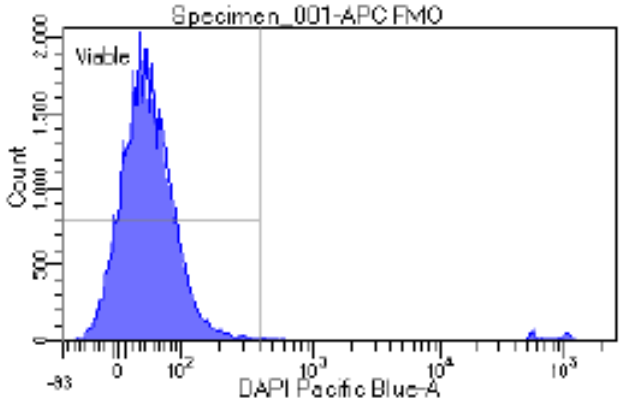

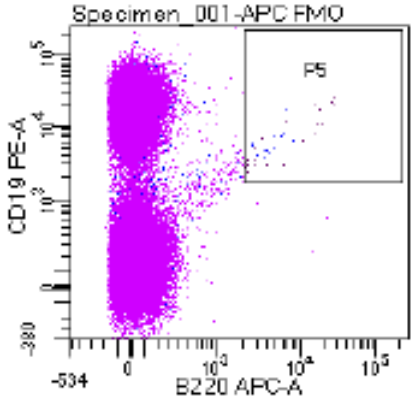

Tube: APC FMO

Population	#Events	%Parent	%Total
All Events	91,421	####	100.0
Scatter	54,222	59.3	59.3
SSC singlets	52,697	97.2	57.6
Single cells	52,084	98.8	57.0
Viable	50,115	96.2	54.8
P5	26	0.1	0.0

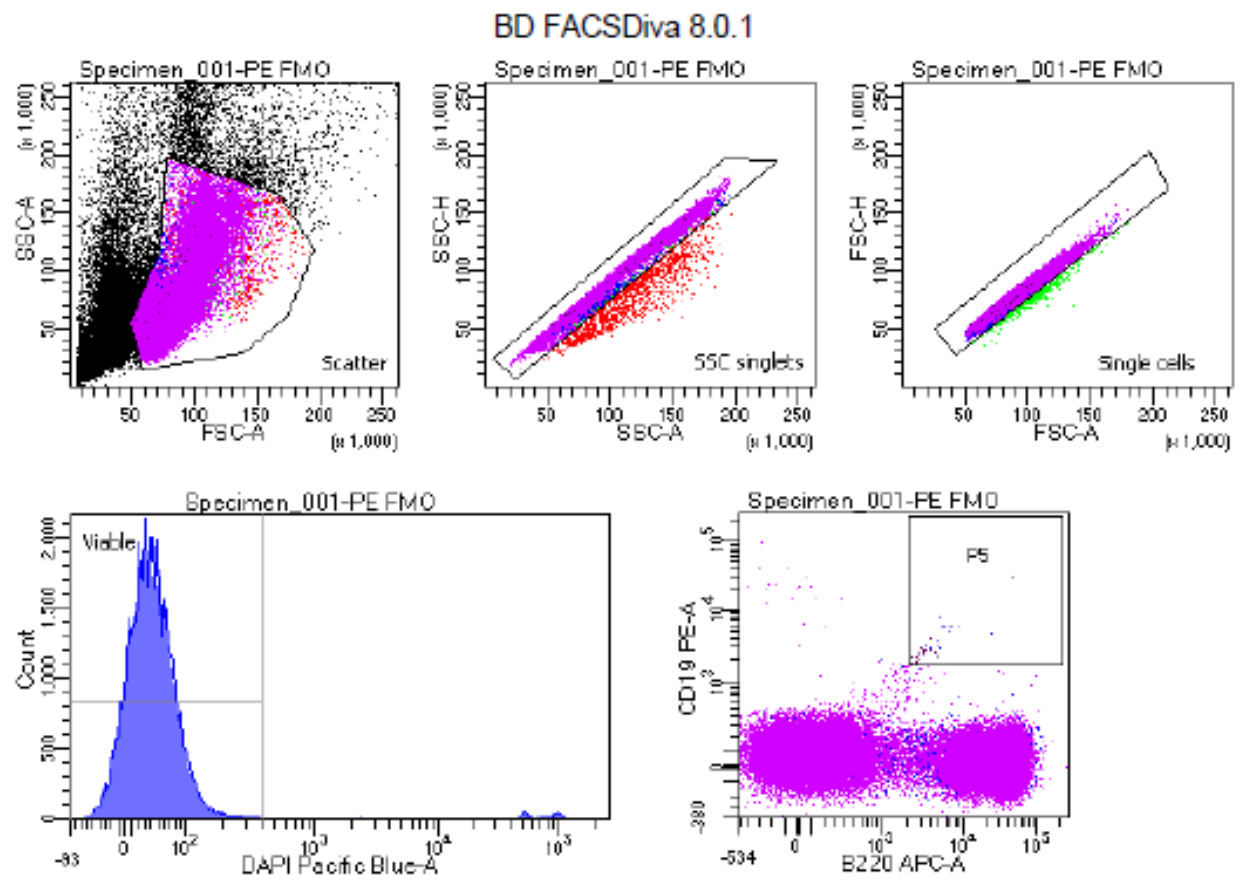

Tube: PE FMO

Population	#Events	%Parent	%Total
All Events	87,769	####	100.0
Scatter	53,736	61.2	61.2
SSC singlets	52,424	97.6	59.7
Single cells	51,826	98.9	59.0
Viable	50,085	96.6	57.1
P5	23	0.0	0.0

BD FACSDiva 8.0.1

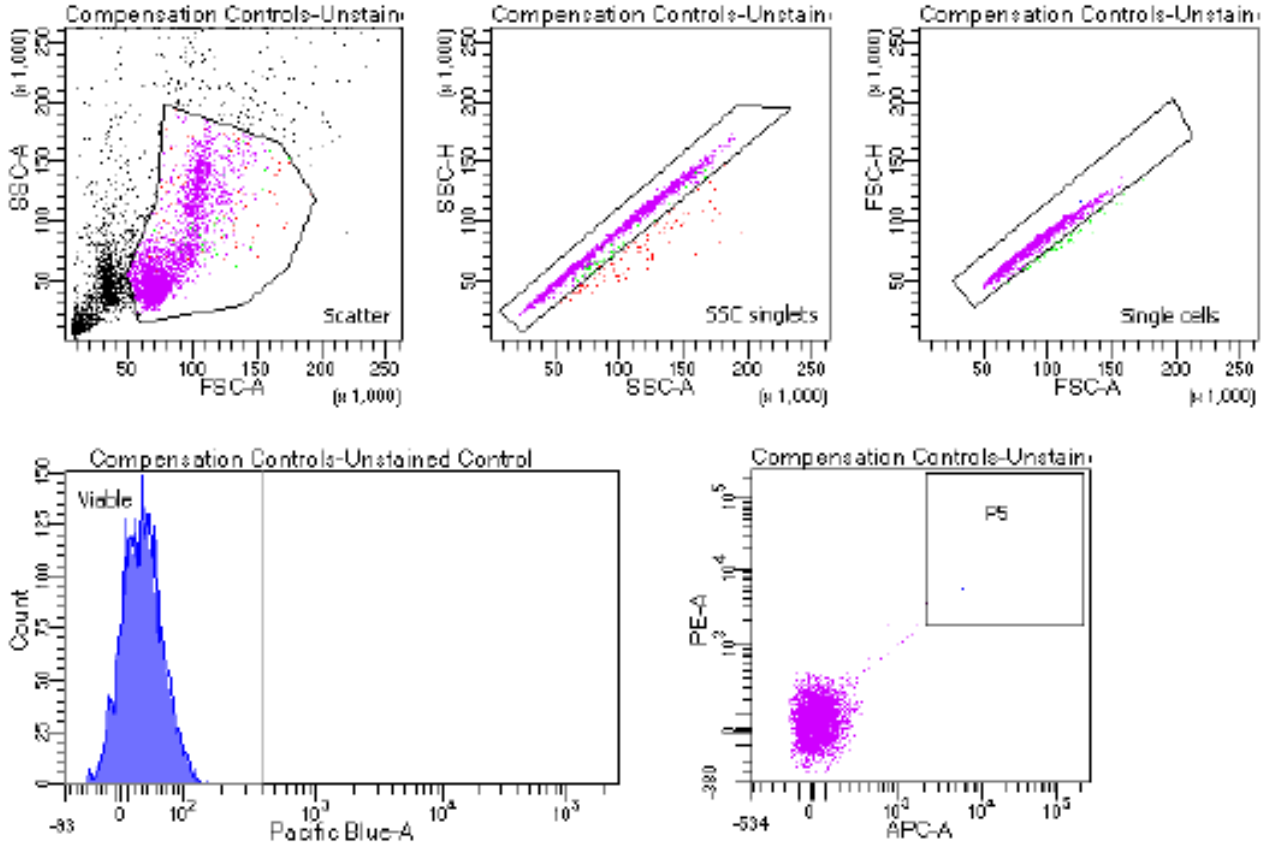

Tube: Unstained Control

Population	#Events	%Parent	%Total
All Events	5,000	####	100.0
Scatter	3,128	62.6	62.6
SSC singlets	3,042	97.3	60.8
Single cells	2,992	98.4	59.8
Viable	2,991	100.0	59.8
P5	1	0.0	0.0

BD FACSDiva 8.0.1

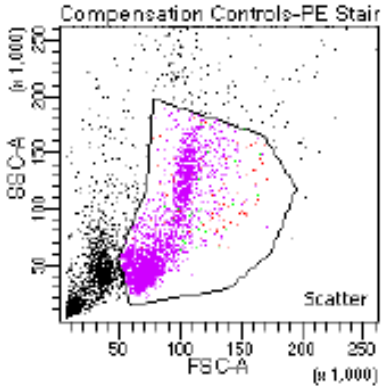

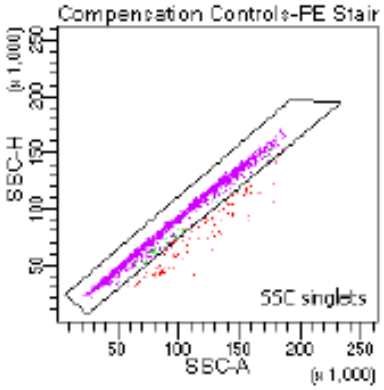

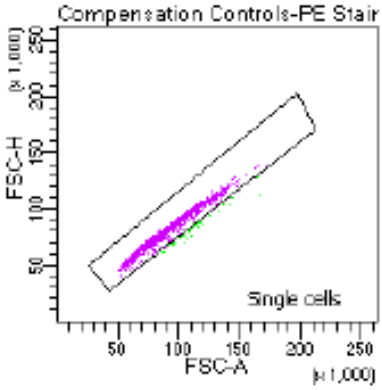

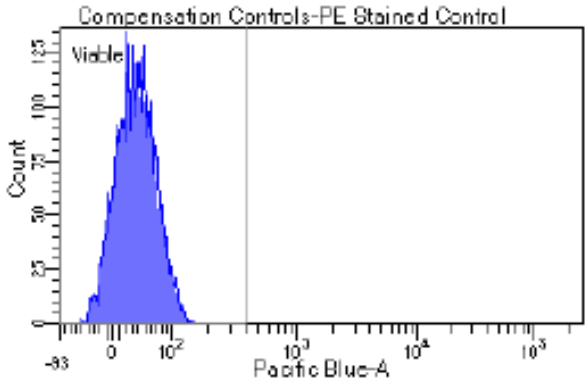

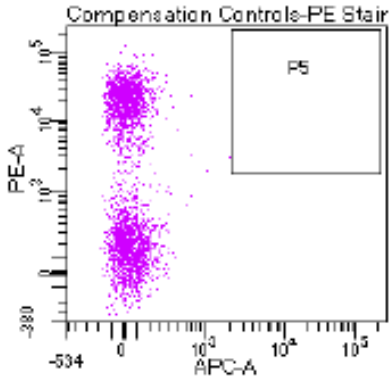

Tube: PE Stained Control

Population	#Events	%Parent	%Total
All Events	5,000	####	100.0
Scatter	3,075	61.5	61.5
SSC singlets	2,974	96.7	59.5
Single cells	2,925	98.4	58.5
Viable	2,925	100.0	58.5
P5	0	0.0	0.0

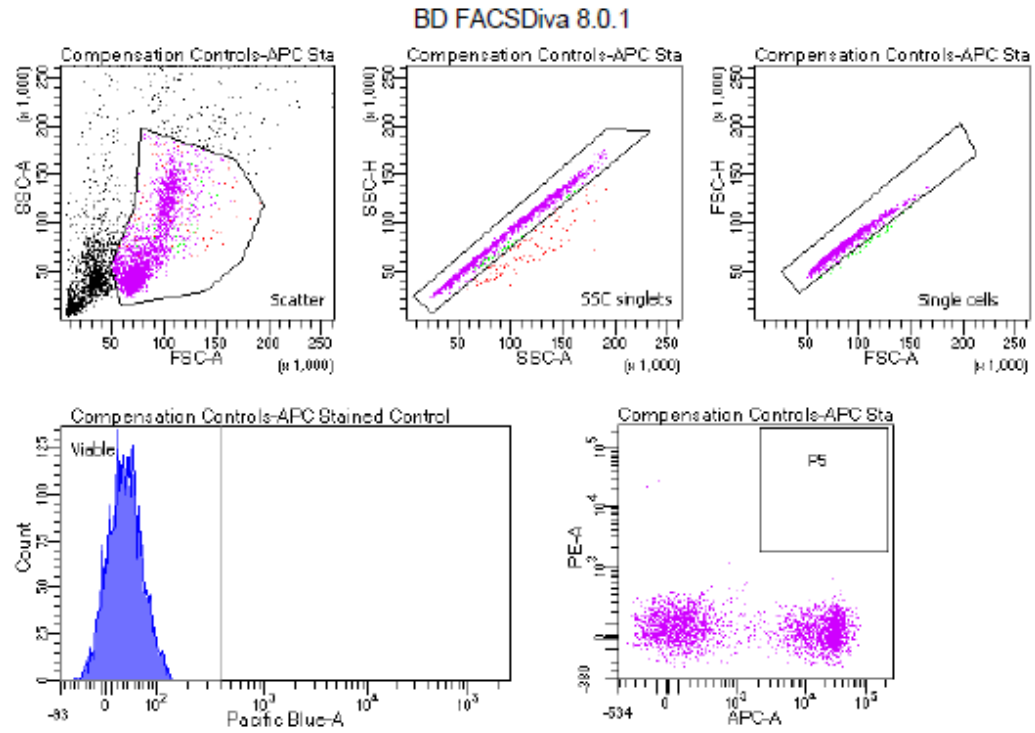

Tube: APC Stained Control

Population	#Events	%Parent	%Total
All Events	5,000	####	100.0
Scatter	3,005	60.1	60.1
SSC singlets	2,907	96.7	58.1
Single cells	2,862	98.5	57.2
Viable	2,862	100.0	57.2
P5	0	0.0	0.0

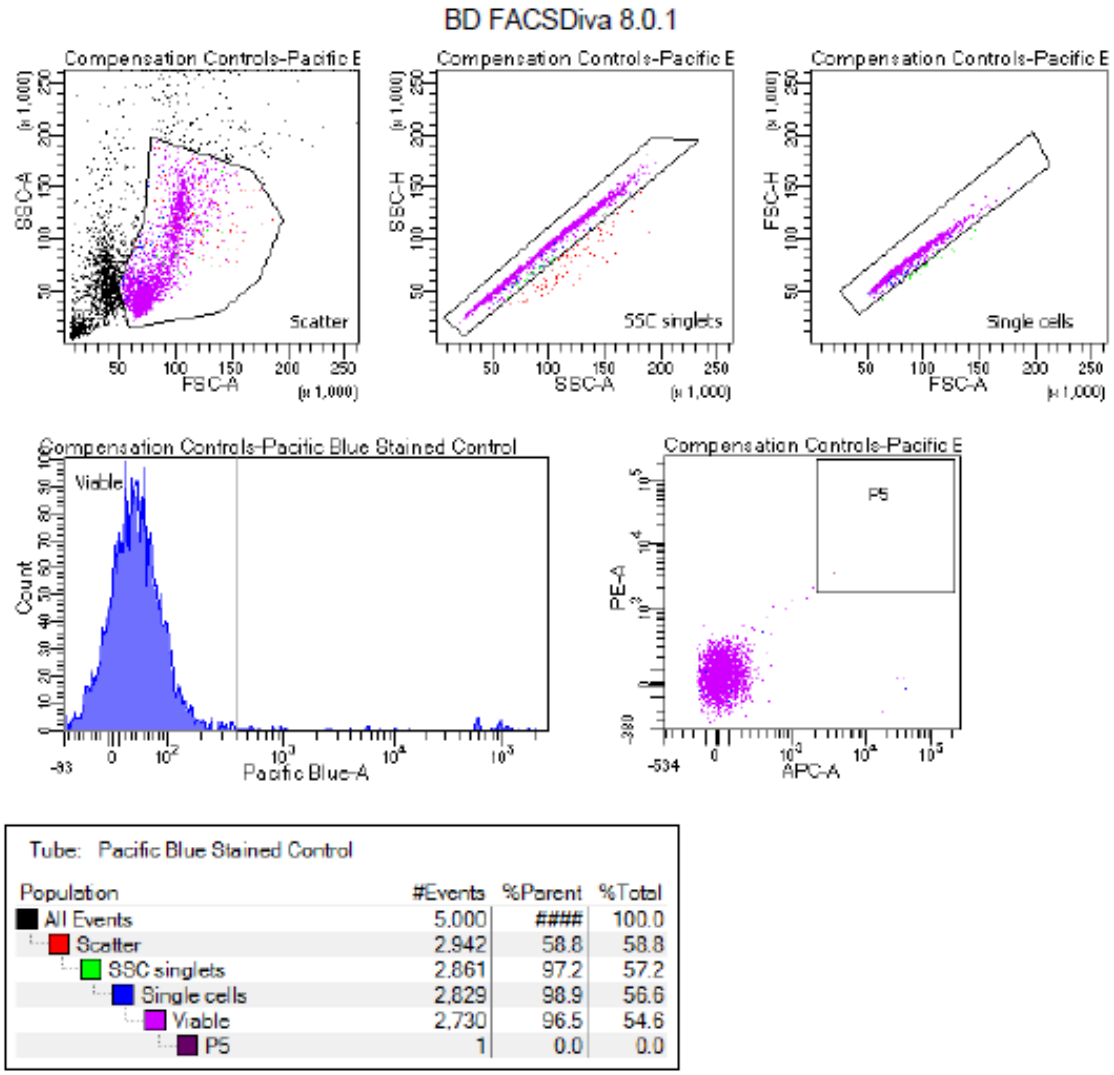

Supplementary Figure 4.3: Flow gating for B cells harvested from mouse spleens and livers

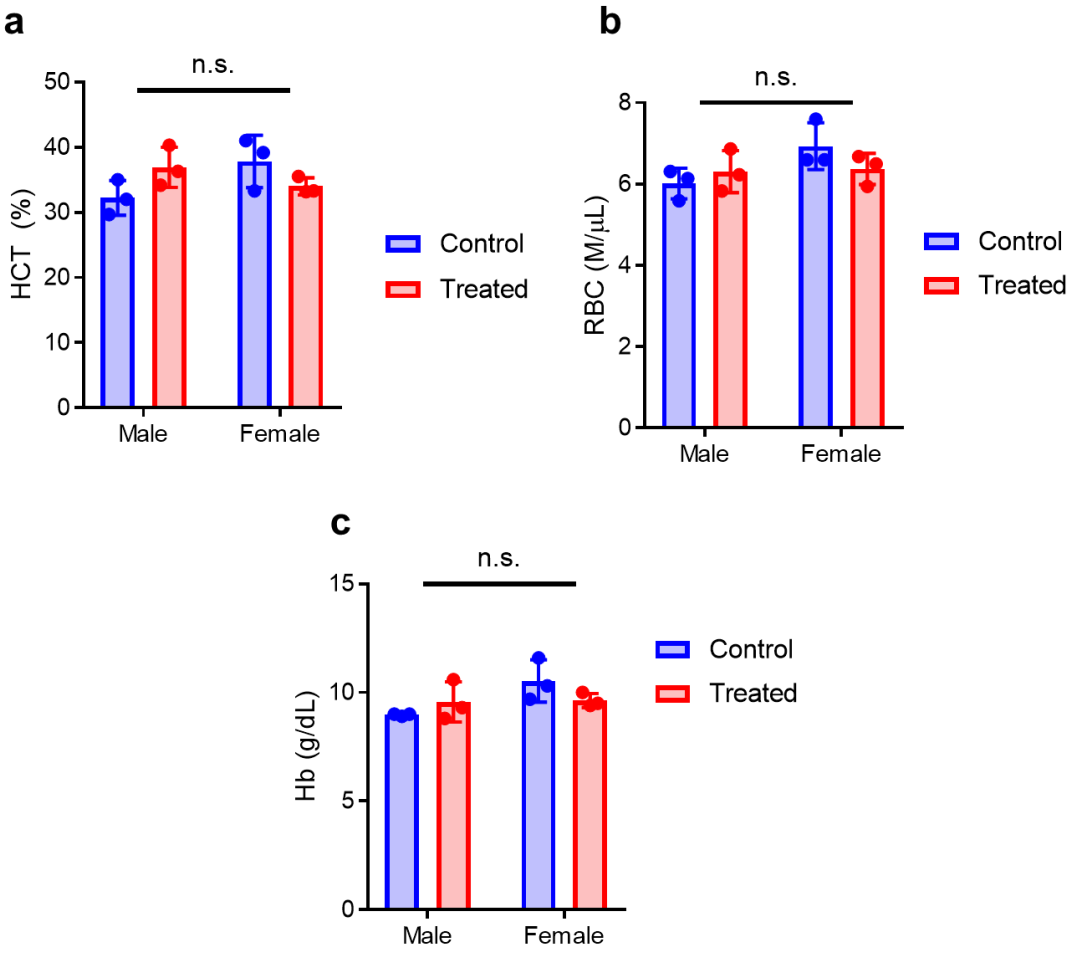

Supplementary Figure 4.4: Complete blood count values collected from mice 3 days after injection with 20 mg/kg of siRNA conjugate targeting Mcl-1. Significance assessed by 2-way ANOVA (n=3).

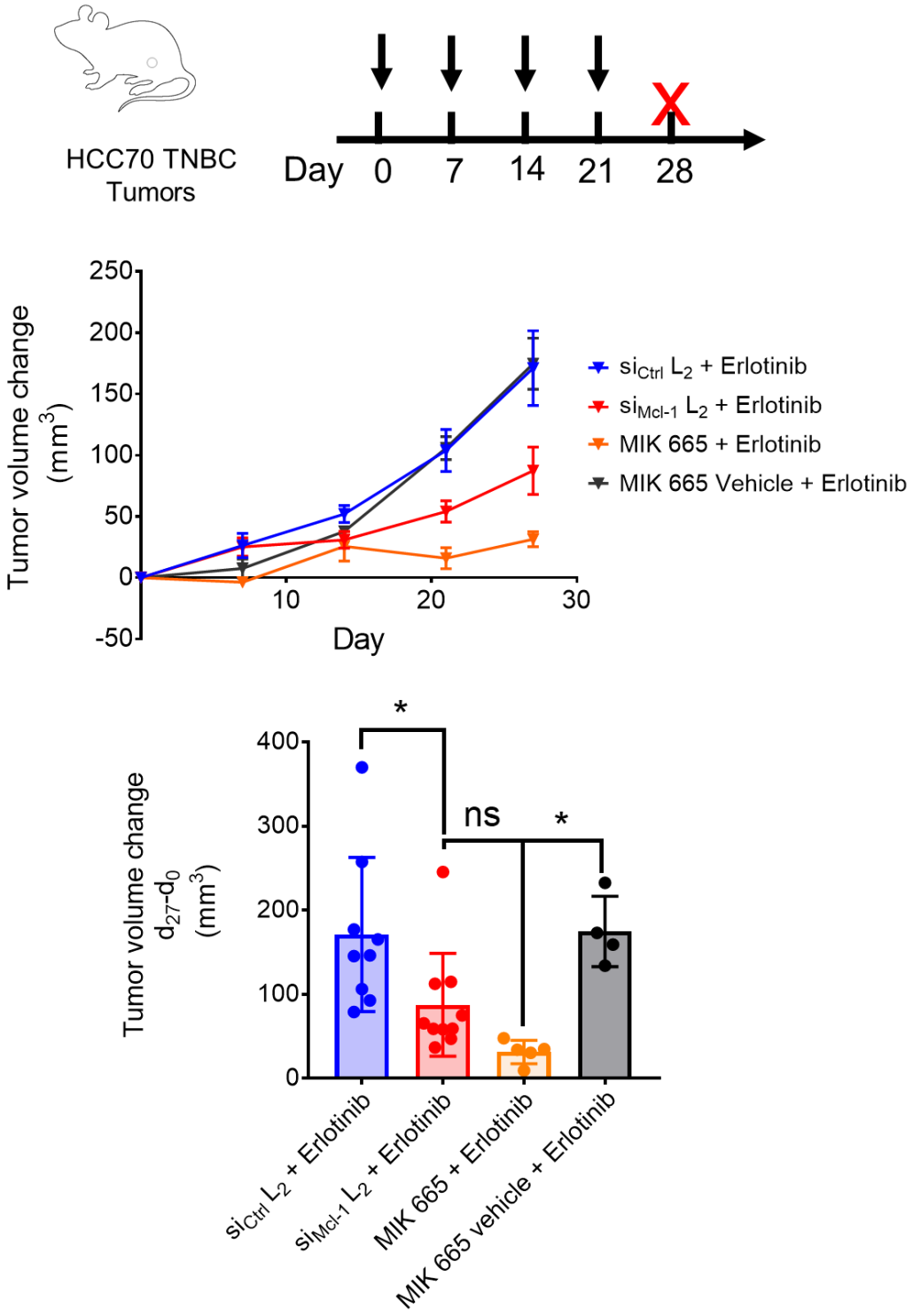

Supplementary Figure 4.5: Small molecule inhibitor MIK 665 requires cotreatment with EGFR inhibitor to achieve reduction in tumor burden (A) Change in tumor volume from day 0 (measured by a blinded observer) over the course of 28 days with once weekly intravenous treatment of either

10mg/kg siRNA or 12.5 mg/kg MIK 665 +/- oral treatment with 42.5 mg/kg erlotinib (Mean +/- SEM plotted) (n=6-9). (B) Tumor volume change on day 28 of treatment. Significance assessed by one-way ANOVA with Sidak's multiple comparisons test (n=6-9).

BIBIOLOGRAPHY

1. Hu, B. et al. Therapeutic siRNA: state of the art. *Signal Transduct Target Ther* **5**, 101 (2020).
2. Caplen, N.J. & Mousses, S. Short interfering RNA (siRNA)-mediated RNA interference (RNAi) in human cells. *Ann N Y Acad Sci* **1002**, 56-62 (2003).
3. Adams, D. et al. Patisiran, an RNAi Therapeutic, for Hereditary Transthyretin Amyloidosis. *N Engl J Med* **379**, 11-21 (2018).
4. Moss, K.H., Popova, P., Hadrup, S.R., Astakhova, K. & Taskova, M. Lipid Nanoparticles for Delivery of Therapeutic RNA Oligonucleotides. *Mol Pharm* **16**, 2265-2277 (2019).
5. Kulkarni, J.A., Witzigmann, D., Leung, J., Tam, Y.Y.C. & Cullis, P.R. On the role of helper lipids in lipid nanoparticle formulations of siRNA. *Nanoscale* **11**, 21733-21739 (2019).
6. Hoy, S.M. Patisiran: First Global Approval. *Drugs* **78**, 1625-1631 (2018).
7. Garber, K. Worth the RISC? *Nat Biotechnol* **35**, 198-202 (2017).
8. Weiss, W.A., Taylor, S.S. & Shokat, K.M. Recognizing and exploiting differences between RNAi and small-molecule inhibitors. *Nat Chem Biol* **3**, 739-744 (2007).
9. Patel, M.N., Halling-Brown, M.D., Tym, J.E., Workman, P. & Al-Lazikani, B. Objective assessment of cancer genes for drug discovery. *Nat Rev Drug Discov* **12**, 35-50 (2013).
10. Bae, Y.H. & Park, K. Targeted drug delivery to tumors: myths, reality and possibility. *J Control Release* **153**, 198-205 (2011).
11. Danhier, F. To exploit the tumor microenvironment: Since the EPR effect fails in the clinic, what is the future of nanomedicine? *Journal of Controlled Release* **244**, 108-121 (2016).
12. Maeda, H., Sawa, T. & Konno, T. Mechanism of tumor-targeted delivery of macromolecular drugs, including the EPR effect in solid tumor and clinical overview of the prototype polymeric drug SMANCS. *J Control Release* **74**, 47-61 (2001).
13. Matsumura, Y. & Maeda, H. A new concept for macromolecular therapeutics in cancer chemotherapy: mechanism of tumoritropic accumulation of proteins and the antitumor agent smancs. *Cancer research* **46**, 6387-6392 (1986).
14. Hoogenboezem, E.N. & Duvall, C.L. Harnessing albumin as a carrier for cancer therapies. *Adv Drug Deliv Rev* **130**, 73-89 (2018).
15. Evans, T.W. Review article: albumin as a drug-biological effects of albumin unrelated to oncotic pressure. *Alimentary Pharmacology and Therapeutics* **16**, 6-11 (2002).
16. Stehle, G. et al. Plasma protein (albumin) catabolism by the tumor itself--implications for tumor metabolism and the genesis of cachexia. *Crit Rev Oncol Hematol* **26**, 77-100 (1997).
17. Campbell, P.M. & Der, C.J. Oncogenic Ras and its role in tumor cell invasion and metastasis. *Seminars in Cancer Biology* **14**, 105-114 (2004).
18. Commisso, C. et al. Macropinocytosis of protein is an amino acid supply route in Ras-transformed cells. *Nature* **497**, 633-637 (2013).
19. Chatterjee, M. et al. Caveolae-Mediated Endocytosis Is Critical for Albumin Cellular Uptake and Response to Albumin-Bound Chemotherapy. *Cancer Research*.
20. Desai, N., Trieu, V., Damascelli, B. & Soon-Shiong, P. SPARC Expression Correlates with Tumor Response to Albumin-Bound Paclitaxel in Head and Neck Cancer Patients. *Translational Oncology* **2**, 59-64 (2009).
21. Hidalgo, M. et al. SPARC Expression Did Not Predict Efficacy of nab-Paclitaxel Plus Gemcitabine or Gemcitabine Alone for Metastatic Pancreatic Cancer in an Exploratory Analysis of the Phase III MPACT Trial.

22. Pinilla, S.M.R., Honrado, E., Hardisson, D., Benítez, J. & Palacios, J. Caveolin-1 expression is associated with a basal-like phenotype in sporadic and hereditary breast cancer. *Breast Cancer Research and Treatment* **99**, 85-90 (2006).
23. Tahir, S.A. et al. Secreted caveolin-1 stimulates cell survival/clonal growth and contributes to metastasis in androgen-insensitive prostate cancer. *Cancer research* **61**, 3882-3885 (2001).
24. Suzuoki, M. et al. Impact of caveolin-1 expression on prognosis of pancreatic ductal adenocarcinoma. *British Journal of Cancer* **87**, 1140-1144 (2002).
25. Schubert, W. et al. Caveolae-deficient endothelial cells show defects in the uptake and transport of albumin in vivo. *The Journal of biological chemistry* **276**, 48619-48622 (2001).
26. Valstar, A., Almgren, M., Brown, W. & Vasilescu, M. The interaction of bovine serum albumin with surfactants studied by light scattering. *Langmuir* **16**, 922-927 (2000).
27. Gull, N., Khan, J., Rukhsana & Khan, R. Spectroscopic studies on the gemini surfactant mediated refolding of human serum albumin. *International Journal of Biological Macromolecules* **102**, 331-335 (2017).
28. Qin, S. et al. A physiological perspective on the use of imaging to assess the in vivo delivery of therapeutics. *Ann Biomed Eng* **42**, 280-298 (2014).
29. Merlot, A.M., Kalinowski, D.S. & Richardson, D.R. Unraveling the mysteries of serum albuminâ€"more than just a serum protein. *Frontiers in Physiology* **5**, 299-299 (2014).
30. Knudsen, L.B. & Lau, J. The Discovery and Development of Liraglutide and Semaglutide. *Front Endocrinol (Lausanne)* **10**, 155 (2019).
31. Knudsen, L.B. et al. Potent derivatives of glucagon-like peptide-1 with pharmacokinetic properties suitable for once daily administration. *Journal of Medicinal Chemistry* **43**, 1664-1669 (2000).
32. Liu, H. et al. Structure-based programming of lymph-node targeting in molecular vaccines. *Nature* **507**, 519-522 (2014).
33. Hvam, M.L. et al. Fatty Acid-Modified Gapmer Antisense Oligonucleotide and Serum Albumin Constructs for Pharmacokinetic Modulation. *Molecular Therapy* **25**, 1710-1717 (2017).
34. Lacroix, A., Edwardson, T.G.W., Hancock, M.A., Dore, M.D. & Sleiman, H.F. Development of DNA Nanostructures for High-Affinity Binding to Human Serum Albumin. *J Am Chem Soc* **139**, 7355-7362 (2017).
35. Zheng, Y.-R. et al. Pt(IV) Prodrugs Designed to Bind Non-Covalently to Human Serum Albumin for Drug Delivery. *Journal of the American Chemical Society* **136**, 8790-8798 (2014).
36. Adams, J.M. & Cory, S. The Bcl-2 apoptotic switch in cancer development and therapy. *Oncogene* **26**, 1324-1337 (2007).
37. Akgul, C. Mcl-1 is a potential therapeutic target in multiple types of cancer. *Cell Mol Life Sci* **66**, 1326-1336 (2009).
38. Danial, N.N. & Korsmeyer, S.J. Cell death: critical control points. *Cell* **116**, 205-219 (2004).
39. Lowe, S.W. & Lin, A.W. Apoptosis in cancer. *Carcinogenesis* **21**, 485-495 (2000).
40. Warr, M.R. & Shore, G.C. Unique biology of Mcl-1: therapeutic opportunities in cancer. *Curr Mol Med* **8**, 138-147 (2008).
41. Song, L., Coppola, D., Livingston, S., Cress, D. & Haura, E.B. Mcl-1 regulates survival and sensitivity to diverse apoptotic stimuli in human non-small cell lung cancer cells. *Cancer Biol Ther* **4**, 267-276 (2005).
42. Zhang, H. et al. Mcl-1 is critical for survival in a subgroup of non-small-cell lung cancer cell lines. *Oncogene* **30**, 1963-1968 (2011).

43. Beroukhim, R. et al. The landscape of somatic copy-number alteration across human cancers. *Nature* **463**, 899-905 (2010).
44. Williams, M.M. et al. Intrinsic apoptotic pathway activation increases response to anti-estrogens in luminal breast cancers. *Cell Death Dis* **9**, 21 (2018).
45. Goodwin, C.M., Rossanese, O.W., Olejniczak, E.T. & Fesik, S.W. Myeloid cell leukemia-1 is an important apoptotic survival factor in triple-negative breast cancer. *Cell Death Differ* **22**, 2098-2106 (2015).
46. Wei, S.H. et al. Inducing apoptosis and enhancing chemosensitivity to gemcitabine via RNA interference targeting Mcl-1 gene in pancreatic carcinoma cell. *Cancer Chemother Pharmacol* **62**, 1055-1064 (2008).
47. Ding, Q. et al. Myeloid cell leukemia-1 inversely correlates with glycogen synthase kinase-3beta activity and associates with poor prognosis in human breast cancer. *Cancer research* **67**, 4564-4571 (2007).
48. Wertz, I.E. et al. Sensitivity to antitubulin chemotherapeutics is regulated by MCL1 and FBW7. *Nature* **471**, 110-114 (2011).
49. Balko, J.M. et al. Molecular profiling of the residual disease of triple-negative breast cancers after neoadjuvant chemotherapy identifies actionable therapeutic targets. *Cancer Discov* **4**, 232-245 (2014).
50. Kawabata, T. et al. Up-regulation of pro-apoptotic protein Bim and down-regulation of anti-apoptotic protein Mcl-1 cooperatively mediate enhanced tumor cell death induced by the combination of ERK kinase (MEK) inhibitor and microtubule inhibitor. *J Biol Chem* **287**, 10289-10300 (2012).
51. Fagg, J., Vol. 2020 (September 13, 2019).
52. Czabotar, P.E. et al. Structural insights into the degradation of Mcl-1 induced by BH3 domains. *Proceedings of the National Academy of Sciences of the United States of America* **104**, 6217-6222 (2007).
53. Wan, Y., Dai, N., Tang, Z. & Fang, H. Small-molecule Mcl-1 inhibitors: Emerging anti-tumor agents. *European Journal of Medicinal Chemistry* **146**, 471-482 (2018).
54. Lee, K.M. et al. MYC and MCL1 Cooperatively Promote Chemotherapy-Resistant Breast Cancer Stem Cells via Regulation of Mitochondrial Oxidative Phosphorylation. *Cell Metab* **26**, 633-647 e637 (2017).
55. Rasmussen, M.L. et al. A Non-apoptotic Function of MCL-1 in Promoting Pluripotency and Modulating Mitochondrial Dynamics in Stem Cells. *Stem Cell Reports* **10**, 684-692 (2018).
56. Merino, D. et al. Synergistic action of the MCL-1 inhibitor S63845 with current therapies in preclinical models of triple-negative and HER2-amplified breast cancer. *Sci Transl Med* **9** (2017).
57. Kotschy, A. et al. The MCL1 inhibitor S63845 is tolerable and effective in diverse cancer models. *Nature* **538**, 477-482 (2016).
58. Merino, D. et al. Synergistic action of the MCL-1 inhibitor S63845 with current therapies in preclinical models of triple-negative and HER2-amplified breast cancer. *Sci Transl Med* **9** (2017).
59. Opferman, J.T. et al. Obligate role of anti-apoptotic MCL-1 in the survival of hematopoietic stem cells. *Science (New York, N.Y.)* **307**, 1101-1104 (2005).
60. Wang, X. et al. Deletion of MCL-1 causes lethal cardiac failure and mitochondrial dysfunction. *Genes & development* **27**, 1351-1364 (2013).

61. Thomas, R.L. et al. Loss of MCL-1 leads to impaired autophagy and rapid development of heart failure. *Genes & development* **27**, 1365-1377 (2013).
62. Brennan, M.S. et al. Humanized Mcl-1 mice enable accurate preclinical evaluation of MCL-1 inhibitors destined for clinical use. *Blood* **132**, 1573-1583 (2018).
63. Sarett, S.M. et al. Lipophilic siRNA targets albumin in situ and promotes bioavailability, tumor penetration, and carrier-free gene silencing. *Proceedings of the National Academy of Sciences* **114**, E6490-E6497 (2017).
64. Allerson, C.R. et al. Fully 2'-modified oligonucleotide duplexes with improved in vitro potency and stability compared to unmodified small interfering RNA. *J Med Chem* **48**, 901-904 (2005).
65. Nair, J.K. et al. Impact of enhanced metabolic stability on pharmacokinetics and pharmacodynamics of GalNAc-siRNA conjugates. *Nucleic Acids Res* **45**, 10969-10977 (2017).
66. Ozpolat, B., Sood, A.K. & Lopez-Berestein, G. Nanomedicine based approaches for the delivery of siRNA in cancer. *J Intern Med* **267**, 44-53 (2010).
67. Biscans, A., Coles, A., Echeverria, D. & Khvorova, A. The valency of fatty acid conjugates impacts siRNA pharmacokinetics, distribution, and efficacy in vivo. *J Control Release* **302**, 116-125 (2019).
68. Madsen, K. et al. Structure-Activity and Protraction Relationship of Long-Acting Glucagon-like Peptide-1 Derivatives: Importance of Fatty Acid Length, Polarity, and Bulkiness. *Journal of Medicinal Chemistry* **50**, 6126-6132 (2007).
69. Prakash, T.P. et al. Fatty acid conjugation enhances potency of antisense oligonucleotides in muscle. *Nucleic Acids Res* **47**, 6029-6044 (2019).
70. Lau, J. et al. Discovery of the Once-Weekly Glucagon-Like Peptide-1 (GLP-1) Analogue Semaglutide. *Journal of Medicinal Chemistry* **58**, 7370-7380 (2015).
71. Jeong, J.H., Mok, H., Oh, Y.K. & Park, T.G. siRNA conjugate delivery systems. *Bioconjug Chem* **20**, 5-14 (2009).
72. Shmushkovich, T. et al. Functional features defining the efficacy of cholesterol-conjugated, self-deliverable, chemically modified siRNAs. *Nucleic Acids Res* **46**, 10905-10916 (2018).
73. Osborn, M.F. & Khvorova, A. Improving siRNA Delivery In Vivo Through Lipid Conjugation. *Nucleic Acid Ther* **28**, 128-136 (2018).
74. Sarett, S.M. et al. Lipophilic siRNA targets albumin in situ and promotes bioavailability, tumor penetration, and carrier-free gene silencing. *Proceedings of the National Academy of Sciences of the United States of America* **114**, E6490-E6497 (2017).
75. Li, L. & Shen, Y. Overcoming obstacles to develop effective and safe siRNA therapeutics. *Expert Opin Biol Ther* **9**, 609-619 (2009).
76. Wolfrum, C. et al. Mechanisms and optimization of in vivo delivery of lipophilic siRNAs. *Nat Biotechnol* **25**, 1149-1157 (2007).
77. Liu, H. et al. DNA-based micelles: synthesis, micellar properties and size-dependent cell permeability. *Chemistry* **16**, 3791-3797 (2010).
78. Chen, T. et al. DNA micelle flares for intracellular mRNA imaging and gene therapy. *Angew Chem Int Ed Engl* **52**, 2012-2016 (2013).
79. Patwa, A., Gissot, A., Bestel, I. & Barthélémy, P. Hybrid lipid oligonucleotide conjugates: synthesis, self-assemblies and biomedical applications. *Chem Soc Rev* **40**, 5844-5854 (2011).
80. Ercole, F., Whittaker, M.R., Quinn, J.F. & Davis, T.P. Cholesterol Modified Self-Assemblies and Their Application to Nanomedicine. *Biomacromolecules* **16**, 1886-1914 (2015).
81. Osborn, M.F. et al. Hydrophobicity drives the systemic distribution of lipid-conjugated siRNAs via lipid transport pathways. *Nucleic Acids Res* **47**, 1070-1081 (2019).

82. Birn, H. & Christensen, E.I. Renal albumin absorption in physiology and pathology. *Kidney International* **69**, 440-449 (2006).
83. Sleep, D., Cameron, J. & Evans, L.R. Albumin as a versatile platform for drug half-life extension. *Biochim Biophys Acta* **1830**, 5526-5534 (2013).
84. Birn, H. et al. Cubilin is an albumin binding protein important for renal tubular albumin reabsorption. *The Journal of clinical investigation* **105**, 1353-1361 (2000).
85. Klein, D. et al. Centyrin ligands for extrahepatic delivery of siRNA. *Mol Ther* **29**, 2053-2066 (2021).
86. Dassie, J., McNamara Ii, J. & Giangrande, P. Systemic administration of optimize aptamer-siRNA chimeras promotes regression of PSMA-expressing tumors. *nature biotechnology* **27** (2009).
87. Coutinho, P.J.G., Castanheira, E.M.S., Rei, M.C. & Oliveira, M.E.C.D.R. Nile Red and DCM Fluorescence Anisotropy Studies in C12E7/DPPC Mixed Systems. *The Journal of Physical Chemistry B* **106**, 12841-12846 (2002).
88. Brown, D.A. et al. Effect of phosphorothioate modification of oligodeoxynucleotides on specific protein binding. *J Biol Chem* **269**, 26801-26805 (1994).
89. Biscans, A. et al. The chemical structure and phosphorothioate content of hydrophobically modified siRNAs impact extrahepatic distribution and efficacy. *Nucleic Acids Res* **48**, 7665-7680 (2020).
90. Spector, A.A., John, K. & Fletcher, J.E. Binding of long-chain fatty acids to bovine serum albumin. *J Lipid Res* **10**, 56-67 (1969).
91. Spector, A.A. Fatty acid binding to plasma albumin. *Journal of Lipid Research* **16**, 165-179 (1975).
92. Parks, J.S., Cistola, D.P., Small, D.M. & Hamilton, J.A. Interactions of the carboxyl group of oleic acid with bovine serum albumin: a 13C NMR study. *Journal of Biological Chemistry* **258**, 9262-9269 (1983).
93. Frei, E. Albumin binding ligands and albumin conjugate uptake by cancer cells. *Diabetology & Metabolic Syndrome* **3**, 11 (2011).
94. Vollhardt, D. Effect of unsaturation in fatty acids on the main characteristics of Langmuir monolayers. *Journal of Physical Chemistry C* **111**, 6805-6812 (2007).
95. Alberts, B. et al. in Molecular Biology of the Cell. 4th edition (Garland Science, 2002).
96. Ashbrook, J.D., Spector, A.A., Santos, E.C. & Fletcher, J.E. Long chain fatty acid binding to human plasma albumin. *J Biol Chem* **250**, 2333-2338 (1975).
97. BIRKETT, D.J., MYERS, S.P. & SUDLOW, G. Effects of Fatty Acids on Two Specific Drug Binding Sites on Human Serum Albumin. *Molecular Pharmacology* **13**, 987-992 (1977).
98. Saito, G., Swanson, J.A. & Lee, K.D. Drug delivery strategy utilizing conjugation via reversible disulfide linkages: role and site of cellular reducing activities. *Adv Drug Deliv Rev* **55**, 199-215 (2003).
99. Schnitzer, J.E., Sung, A., Horvat, R. & Bravo, J. Preferential interaction of albumin-binding proteins, gp30 and gp18, with conformationally modified albumins. Presence in many cells and tissues with a possible role in catabolism. *J Biol Chem* **267**, 24544-24553 (1992).
100. Schnitzer, J.E. & Bravo, J. High affinity binding, endocytosis, and degradation of conformationally modified albumins. Potential role of gp30 and gp18 as novel scavenger receptors. *J Biol Chem* **268**, 7562-7570 (1993).

101. Schnitzer, J.E. & Oh, P. Albondin-mediated capillary permeability to albumin. Differential role of receptors in endothelial transcytosis and endocytosis of native and modified albumins. *J Biol Chem* **269**, 6072-6082 (1994).
102. Foulkes, W.D., Smith, I.E. & Reis-Filho, J.S. Triple-negative breast cancer. *New England journal of medicine* **363**, 1938-1948 (2010).
103. Liedtke, C. et al. Response to neoadjuvant therapy and long-term survival in patients with triple-negative breast cancer. *Journal of clinical oncology* **26**, 1275-1281 (2008).
104. Tan, D.S. et al. Triple negative breast cancer: molecular profiling and prognostic impact in adjuvant anthracycline-treated patients. *Breast cancer research and treatment* **111**, 27-44 (2008).
105. Lee, K.M. et al. MYC and MCL1 Cooperatively Promote Chemotherapy-Resistant Breast Cancer Stem Cells via Regulation of Mitochondrial Oxidative Phosphorylation. *Cell Metab* **26**, 633-647 e637 (2017).
106. Mason, K.D. et al. Programmed anuclear cell death delimits platelet life span. *Cell* **128**, 1173-1186 (2007).
107. Oltersdorf, T. et al. An inhibitor of Bcl-2 family proteins induces regression of solid tumours. *Nature* **435**, 677-681 (2005).
108. Anderson, G.R. et al. PIK3CA mutations enable targeting of a breast tumor dependency through mTOR-mediated MCL-1 translation. *Science translational medicine* **8**, 369ra175 (2016).
109. Cruz-Gordillo, P., Honeywell, M.E., Harper, N.W., Leete, T. & Lee, M.J. ELP-dependent expression of. *Sci Signal* **13** (2020).
110. Corkery, B., Crown, J., Clynes, M. & O'Donovan, N. Epidermal growth factor receptor as a potential therapeutic target in triple-negative breast cancer. *Annals of Oncology* **20**, 862-867 (2009).
111. Walsh, J.G. et al. Executioner caspase-3 and caspase-7 are functionally distinct proteases. *Proc Natl Acad Sci U S A* **105**, 12815-12819 (2008).
112. Hightower, E. et al. Phospho-histone H3 (pHH3) immuno-reactivity as a prognostic marker in non-functioning pituitary adenomas. *Pituitary* **15**, 556-561 (2012).
113. Brennan, M.S. et al. Humanized. *Blood* **132**, 1573-1583 (2018).
114. Foster, D.J. et al. Advanced siRNA Designs Further Improve In Vivo Performance of GalNAc-siRNA Conjugates. *Mol Ther* **26**, 708-717 (2018).
115. Haraszti, R.A. et al. 5′-Vinylphosphonate improves tissue accumulation and efficacy of conjugated siRNAs in vivo. *Nucleic Acids Res* **45**, 7581-7592 (2017).
116. Usama, S.M., Thapaliya, E.R., Luciano, M.P. & Schnermann, M.J. Not so innocent: Impact of fluorophore chemistry on the in vivo properties of bioconjugates. *Curr Opin Chem Biol* **63**, 38-45 (2021).
117. Chernikov, I.V. et al. Cholesterol-Containing Nuclease-Resistant siRNA Accumulates in Tumors in a Carrier-free Mode and Silences MDR1 Gene. *Mol Ther Nucleic Acids* **6**, 209-220 (2017).
118. Morrison, C. Alnylam prepares to land first RNAi drug approval. *Nat Rev Drug Discov* **17**, 156-157 (2018).
119. Du Rietz, H., Hedlund, H., Wilhelmson, S., Nordenfelt, P. & Wittrup, A. Imaging small molecule-induced endosomal escape of siRNA. *Nat Commun* **11**, 1809 (2020).
120. Xu, J., Chen, Y. & Olopade, O.I. MYC and Breast Cancer. *Genes & cancer* **1**, 629-640 (2010).
121. Willis, S. et al. Enriched transcription factor signatures in triple negative breast cancer indicates possible targeted therapies with existing drugs. *Meta gene* **4**, 129-141 (2015).

122. Shen, L. et al. Metabolic reprogramming in triple-negative breast cancer through Myc suppression of TXNIP. *Proceedings of the National Academy of Sciences of the United States of America* **112**, 5425-5430 (2015).
123. Camarda, R. et al. Inhibition of fatty acid oxidation as a therapy for MYC-overexpressing triple-negative breast cancer. *Nat Med* **22**, 427-432 (2016).
124. Terunuma, A. et al. MYC-driven accumulation of 2-hydroxyglutarate is associated with breast cancer prognosis. *J Clin Invest* **124**, 398-412 (2014).
125. Sorets, A.G., Rosch, J.C., Duvall, C.L. & Lippmann, E.S. Caveolae-Mediated Transport at the Injured Blood-Brain Barrier as an Underexplored Pathway for Central Nervous System Drug Delivery. *Curr Opin Chem Eng* **30**, 86-95 (2020).